THE UNIVERSITY OF SHEFFIELD

DOCTORAL THESIS

ON THE INTERSYSTEM CROSSING MECHANISM OF [1]BENZOTHIENO[3,2-B][1]BENZOTHIOPHENE CONTAINING SYSTEMS

Author:
Jozra GARRIDO VELASCO

Supervisor:
Prof. Mark GEOGHEGAN
and
Dr. Jenny CLARK

A thesis submitted in fulfillment of the requirements for the degree of Doctor of Philosophy in the

Department of Physics and Astronomy

September 2019

Declaration of Authorship

I, Jozra GARRIDO VELASCO, declare that this thesis titled, "On the inter-system crossing mechanism of [1]benzothieno[3,2-b][1]benzothiophene containing systems " and the work presented in it are my own. I confirm that:

- This work was done wholly or mainly while in candidature for a research degree at this University.
- Where any part of this thesis has previously been submitted for a degree or any other qualification at this University or any other institution, this has been clearly stated.
- Where I have consulted the published work of others, this is always clearly attributed.
- Where I have quoted from the work of others, the source is always given. With the exception of such quotations, this thesis is entirely my own work.
- I have acknowledged all main sources of help.
- Where the thesis is based on work done by myself jointly with others, I have made clear exactly what was done by others and what I have contributed myself.

Signed:

_____

Date:

_____

"*Al necio, le llueve recio.*"

L. Leticia García Arroyo.

"*Would you tell me, please, which way I ought to go from here?*"
"*That depends a good deal on where you want to get to*", *said the Cat.*
"I don't much care where" - said Alice.
"Then it doesn't matter which way you go" said the Cat.

"Alice's adventures in Wonderland". Lewis Carroll

Abstract

Jozra GARRIDO VELASCO

On the intersystem crossing mechanism of [1]benzothieno[3,2-b][1]benzothiophene containing systems

Probably one of the most interesting processes involving spin should be intersystem crossing, a spin-forbidden transition at first approximation, singlet-exciton generated by absorption of a photon converts into a triplet-exciton, or in other cases it proceeds in the opposite direction; from triplet to a singlet in what is called reverse intersystem crossing. To provide clarity about the underlying physical processes, we have developed three experimental setups for the study of intersystem crossing on these systems: Firstly, solutions of [1]**B**enzo**T**hieno[3,2-b][1]**B**enzo**T**hiophene BTBT and octyl chain substitutions at the 2 and 7 position and with various probing techniques as well as quantum modelling through Density Functional Theory *ab initio* calculations. Secondly, then we proceed to use electron-withdrawing and donating substituents at such positions. Thirdly, we managed to insert 2,7-Dioctyl[1]**B**enzo**T**hieno[3,2-b][1]**B**enzo**T**hiophene (C8-BTBT) inside the cavity of a synthetic bioprotein that aided in controlling aggregation and finally with a couple of thin films of C8-BTBT. In C8-BTBT solutions, we observe highly efficient ISC through a spin-vibronic mechanism. This is the first demonstration of such mechanism in thienoacenes molecules. Then through the introduction of electron-withdrawing and electron-donating substituent groups, we saw how the ISC got impacted. We examine the rate of ISC, showing that the introduction of heavy atoms to increase spin-orbit coupling did not yield higher rates of ISC in a counter-intuitive way and which may need to be reviewed by theoreticians. We propose that the mechanism responsible for unusually fast ISC in such materials is due mainly to the role of out of plane vibrations and vibrations originating from the side chains, for their overall interaction play an instrumental role in activating the spin forbidden transition. In the final experiments of aggregates and thin films of C8-BTBT, we found that even in the case of small aggregates intersystem crossing is effectively deactivated as relaxing channel, which our investigation suggests is due to changes of the intermolecular forces that makes crystal packing possible for they inactivate those vibrational modes present in solution.

Acknowledgements

I want to thank all the people involved in my PhD and projects around it.

- I should start acknowledging the body who made this possible the *National Council of Science and Technology* of Mexico (**CONACYT**) through the grant number 277429 with CVU 485829, for their generous support on this endeavour.

- I want to express my sincere admiration and gratitude to my 'Academic Parents' Mark and Jenny. This project has finished because of their unwavering support and continued encouragement, they embody what a proper supervisor should be and I am genuinely thankful for that. Dear Jenny thanks for your seemingly undying patience and a constant stream of help. Mark, I want to give you special thanks for your dedication and willingness to sort-things-out all the time, and for pushing me to break my limitations.

- Along these lines, specially dedicated words need to go to Andrew Joseph Musser and his equally lovely wife Leila Wilmers for not only hosting me in his house but also for showing me how things are done on so many aspects.

- I want to mention my dear cousin Marisel Sinta *aka* 'Bocho' and my friend and colleague 'Goldenboy David' Bossanyi because their help was instrumental in the completion of this work, thank you, guys! I am on your list, I know.

- To my former and present fellows of the G-12 in Hicks building: Ana Lorena Morales (Mexican source of pride and inspiration to do things well), Tom Kennelly, Latifah Alfhaid, Ellie Dougherty, Jamie Blakeman, Emily Hall and Emilia Hudzik.

- To all of whom we shared a few laughs and friendship: Francesco Rossetto, Daniel Pollak, James Pidgeon, 'Yoichi-San', a dedicated one to you Sandra for "NOT taking me to a *Mexican* restaurant" while at St. Andrews. Many thanks too go to the heart–warming "Brit-Trio" Hannah, Alfie and 'just John' Atkinson-Croad.

- To my friends from the Latin-American committee, it was such fun and you were such a fantastic team to lead: 'Julita' (Secretary) and Daniel (Treasurer) unit, Itzel (Media and communication), Lalo (Arts and Inclusion) and my good Emilio (Sports and Vicepresident) and '*El Charly*' for his coaching session.

- Many thanks to all our collaborators: across the sea in *Milano* - Tersilla Virgili, Aurelio Oriana, Giulio Cerullo, Umberto Giovanella and my student friends Lucia Ganzer and Jef Van Aschf (The Belgian). And to our domestic collaborations with Nick Paul, Luke Rochford and all the team at St. Andrews Sai Rajendran, Samuel D. Ifor, the postdocs and PhD students. And here in Sheffield University from the Department of Chemistry to Omar for his delicious Persian rice and aid in cyclic voltammetry measurements, Harry Robson for letting me use his workbench. Special thanks to Julia Weinstein for her humour and friendly pieces of advice on science and sample prep, Dimitrii for showing me to bear with difficult conscientious people, Alex Auty for lending his aid in Transient Absorption Spectroscopy in many occasions and finally to George Sutherland from the Department of Molecular Biology and Biotechnology for preparing the biological samples of this work, sometimes quite promptly.

- For those often neglected but instrumental, the people in the *Hicks Building*'s F-10 which are very helpful, special thanks goes to Beca J. Raynor, Janice Whittaker, Miles Collins and Ursula McGuone.

- Finally, to the memory of those who these past years had left us behind and no longer can raise their glass and join us: my dearest 'Tía Jaci', Tía Tere, 'Tía Lolita', 'Doña Bebes', 'el Tío Fer' and 'el Tío Sergio', special thanks to 'Ale' Mosqueira my favourite teacher, and my very first shared dog 'Luciano'.

"Pero nada de esto sería posible sin mis amadísimos Ilyanova Velasco Pimentel y Francisco Javier de Jesús Garrido Muñoz quienes por su cariño y devoción soy la persona que soy, y pude llegar hasta donde estoy al poner sus hombros monumentales bajo mis pies. Para ti, mi queridísimo hermanito Christian, por tu inmenso amor y apoyo de siempre; en múltiples niveles, en multitud de ocasiones y por ser mi '*ultimate*' carnal."

GRACIAS TOTALES !!

Contents

List of Figures

List of Tables

List of Abbreviations

C8-BTBT	
or	2,7-Dioctyl[1]**B**enzo**T**hieno[3,2-b][1]**B**enzo**T**hiophene
C8-BTBT-C8	
BTBT	**B**enzo**T**hieno[3,2-b][1]**B**enzo**T**hiophene
BR-BTBT	2,7-di**B**romine-[1]**B**enzo**T**hieno[3,2-b][1]**B**enzo**T**hiophene
tBut-BTBT	2,7-di-**T**ert-**b**utyl[1]**B**enzo**T**hieno[3,2-b][1]**B**enzo**T**hiophene
C8-O-BTBT	2,7-Dioctyl**O**xy-[1]**B**enzo**T**hieno[3,2-b][1]**B**enzo**T**hiophene
C6-F13-BTBT	2,7-fluorohexyl[1]**B**enzo**T**hieno[3,2-b][1]**B**enzo**T**hiophene
I-BTBT	2,7-di**I**odo-[1]**B**enzo**T**hieno[3,2-b][1]**B**enzo**T**hiophene
NH_2-BTBT	2,7-diamine-[1]**B**enzo**T**hieno[3,2-b][1]**B**enzo**T**hiophene
NO_2-BTBT	2,7-dinitro-[1]**B**enzo**T**hieno[3,2-b][1]**B**enzo**T**hiophene
DPH-BTBT	2,7-**D**i**Ph**enyl[1]**B**benzo**T**hieno[3,2-b][1]**B**enzo**T**hiophene
AEC	**A**nion **E**xchange **C**hromatography
BL	**B**io**L**uminescence
BOA	**B**orn-**O**ppenheimer **A**pproximation
CL	**C**hemi**L**uminescence
CT	**C**harge -**T**ransfer state
DFT	**D**ensity **F**unctional **T**heory
DNTT	**D**i**N**aphtho[2,3-b:2',3'-f]**T**hieno[3,2-b]**T**hiophene
DPh-NDT	**D**i**Ph**enyl-**N**aphtho**D**i**T**hiophene
EA	**E**lectron **A**ffinity
EL	**E**lectro**L**uminescence
ESR	**E**lectron **S**pin **R**esonance
FCWD	**F**ranckn **C**ondon **W**eighted **D**ensity
FRET	**F**örster **R**esonance **E**nergy **T**ransfer
GSB	**G**round **S**tate **B**leach
HEPES	(4-(2-**H**ydroxy**E**thyl)-1-**P**iperazine**E**thane**S**ulfonic acid)
HFI	**H**yper **F**ine **I**nteractions (Weak)
HOMO	**H**ighest **O**ccupied **M**olecular **O**rbital
IP	**I**onization **P**otential
ITO	**I**ndium **T**in **O**xide
ISC	**I**nter**S**ystem **C**rossing
LCAO	**L**inear **C**ombination of **A**tomic **O**rbitals
LUMO	**L**owest **U**noccupied **M**olecular **O**rbital
MO	**M**olecular **O**rbital
NEXAFS	**N**ear-**E**dge **X**-ray **A**bsorption **F**ine **S**tructure
OFET	**O**rganic **F**ield **E**ffect **T**ransistor
OS	**O**rganic **S**emiconductors
OLED	**O**rganic **L**ight **E**mitting **D**iode
OLET	**O**rganic **L**ight **E**mitting **T**ransistor
OOP	**O**ut **O**f **P**lane –vibrational modes

OPV	**O**rganic **P**hoto**V**oltaics
OSC	**O**rganic **S**olar **C**ells
P3HT	**P**oly(**3**-**H**exyl**T**hiophene)
PA	**P**oly**A**cetylene
PB	**P**hoto**B**leach
PCBM	[6,6]]-**P**henyl-**C**$_{61}$-**B**utyric acid **M**ethyl ester
PEDOT	**P**oly(3,4-**E**thylene**D**i**O**xy**T**hiophene)
PIA	**P**hoto **I**nduced **A**bsorption
PL	**P**hoto**L**uminescence
PLQY	**P**hoto **L**uminescence **Q**uantum **Y**ield
PPP	**P**oly(**P**-**P**henylene
PPV	**P**oly(**P**ara-phenylene **V**inylene
PTFE	**P**oly**T**etra**F**luoro**E**thylene
PTP	**P**oly**T**hio**P**hene
SE	**S**timulated **E**mission
SOC	**S**pin **O**rbit **C**oupling
SOCME	**S**pin **O**rbit **C**oupling **M**atrix **E**lements
TA	**T**ransient **A**bsorption
TCSPC	**T**ime-**C**orrelated **S**ingle-**P**hoton **C**ounting
TIPS	6,13-bis((**T**ri**I**so**P**ropyl**S**ilyl)ethynyl)
TR-PL	**T**ime **R**esolved **P**hoto**L**uminescence

To my precious wife
Laura Leticia García Arroyo

and

my beloved son
Francisco Ubaldo Garrido
García.

1 Introduction

1.1 Motivation.

Organic semiconductors (OS) pose a great promise, an instrumental reason for this is that materials used in their realisation are significantly more abundant and cheaper than those in the inorganic industry. Generally easier to extract and to purify, their synthesis and production processing is by far less expensive energy-wise in contrast with the inorganic industry. In solution processes techniques there are no need of such high purity which requires the associated *clean–rooms* conditions. Finally, there is the pressing necessity to moving closer to greener alternatives in all our endeavours, although silicon-based technologies certainly will not go out of business, organic electronics could capitalise on the richer chemistry, flexibility (both mechanically and in processability) and biocompatibility that these materials are known for.

Important technological advances founded on basic research have enabled organic light-emitting diodes (OLED) to become so ubiquitous. They are used in many digital screens: television[1], computer monitors, smart-phones and quite often small displays (hand-held size). Organic solar cells (OSC) made with polymer semiconducting materials have already surpassed 10% of efficiency [1] and are bendable which means we can roll them in our backpacks and use them in the middle of a desert to power the OLED screen in our mobile phones and make emergency calls if needed. Not least in importance was the emergence of organic field-effect transistors (OFET) –the building blocks of electronics. Given this importance, in organic electronics, an enormous amount of research is directed to its synthesis, characterisation, functionalisation and device engineering. However, it appears to lack a universal method for fabrication, although there are two most common routes: a solution processing approach and a plethora of high-vacuum thermal-sublimation methods. Solution processing is by far the most promising for being the cheapest, and for they could envision industrially tested roll-to-roll

[1] Recall the first so-called 'curved' television, a major commercial success.

printing techniques [2]. Nevertheless, for both there remain problems to overcome; like solution processing interface phenomena, thermal and ambient stability, as well as crystallinity to name the key ones. But let us observe that all depart from the fundamental notion of charge-carrier mobility, and its instrumental role in these physical processes which in turn impact the overall efficiency of all these devices [3].

One of such organic semiconducting materials, is 2,7-dioctyl[1]benzothieno[3,2-b][1] benzothiophene or C8-BTBT for short. Since the team led by Ebata developed C8-BTBT [4] more than a decade ago, it has continuously interested the scientific community for what could potentially be done with it. Thin film transistors have been made with this molecule, it has drawn much attention for its reported surprisingly high charge carrier mobility. Some authors have even claimed an unprecedented value of $43\,cm^2/(Vs)$ [5] for its carrier mobility which supersedes by far the one for amorphous silicon of $0.3\,cm^2/(Vs)$ [6].

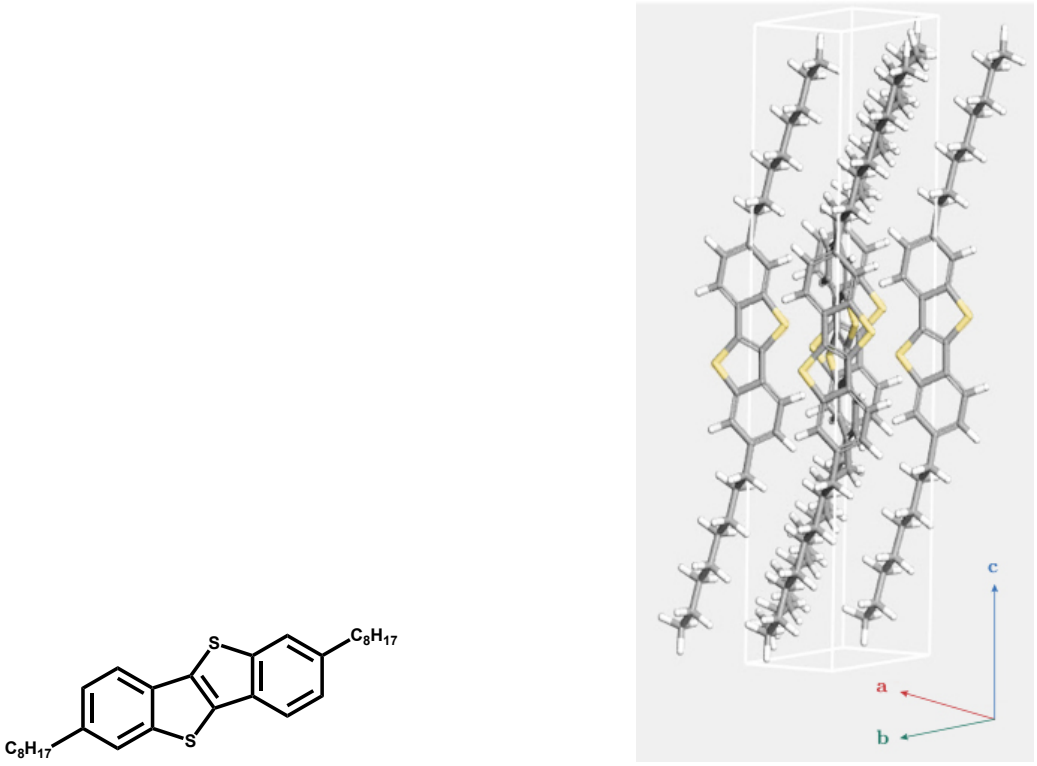

(a) C8-BTBT (b) C8-BTBT unit cell

Figure 1.1. Schematics of C8-BTBT.

1.2 Brief History of Organic Electronics

To some extent, properly defining the origin of organic electronics is a tricky task. On one hand, we have *organic*, which by scientific consensus was decided that everything that carries carbon, hydrogen, oxygen, nitrogen, phosphorus and sulfur shall be called organic. Note also, that the vast majority of such mass comes naturally from all the carbons, which is another way we refer that something is organic. Materials composed of organic molecules can arrange in vastly different ways; Gas–phase, diluted solution, aggregates, polymers, thin films and proper macroscopic crystals. They may behave like insulators and surprisingly like semi-conductors and full-on conductors too, this vast range stems on the wide tunability and rich chemistry they possess.

'Electronics' on the other hand, loosely denotes *a controlled flow of electrons*. This makes currents, and as we know from the well established inorganic electronics, this often entails the use of diodes and transistors, in such fashion that these electrical gates and switches make electrical circuits. Hence, the tacitly accepted way to start the history of organic electronics is to look at when an all-organic or a single organic component successfully mimicked the performance of its inorganic counterpart. Still, the problem arises when we start to think in a wider context on this electron flux. Moving electrons necessarily have kinetic energy, which in turn is what drives currents hence it must have an energy source. For classical electronics, this is often provided by a battery but for biological systems, there is no such source.

Although man was not present to observe the event, the first photochemical reaction probably occurred billions of years ago, when light packed with energy enabled proto-plants to react CO_2 with water molecules to create sugars, water and oxygen through photosynthesis[2]. This process beautifully exemplifies a complex and sophisticated way to view photophysics, as a light-driven electron motion between and within molecules that also allows energy to be stored. Ironically, despite its instrumental importance in virtually all living processes, it was not until the second half of the past century that photophysical processes were seriously investigated. This, of course, resulted from the advancement in the quantum optical sciences (fundamentally lasers) and related technology.

[2]Recent studies suggest that this vital process was taking place on Earth in some form of plant life 1.6 billion years ago [7].

Now, we are in the possibility of not only predict but control the products of a given photochemical reaction [8].

1.2.1 Early Beginnings

Yet light again is what gave birth to the two electronics branches that we enjoy in everyday electronics, either organic or inorganic. *Alexandre-Edmond Becquerel* was the first to observe in 1839 of what we now understand as *the photoelectric effect*. The first human-made photocurrent was made when under the illumination of a silver chloride solution liberated electrons flowed through wires – as electricity [9], establishing the driving mechanism of solar cells. Although modern silicon–based solar cell, owe their origin to an accidental discovery by scientists at *Bell–Laboratories* in 1953. *Gerald Pearson* and *Calvin Fuller* led the pioneering effort that brought forth the silicon transistor. Fuller devised a way for controlling the introduction of impurities needed to transform silicon from a poorly conducting material to a superior conductor of electricity [10]. Among the experiments they did with the specially produced silicon; they exposed it to the sun while connected to a device that measured the electrical flow. To Pearson's surprise, he observed an electric output almost fivefold greater than the best selenium produced. Then, his friend Daryl Chapin entered the project for he was working on selenium and related optical problems, eventually, this would lead to the first massive success of such technology: In 1955, the American government announced its intention of launching a satellite. The launching of the *'Vanguard'*, the first satellite equipped with solar cells, demonstrated their value [11]. Solar-powered Vanguard continued to communicate with the Earth for many years after the energy stored in the batteries was exhausted, allowing the completion of many valuable experiments. Instead, previous satellites ran by batteries, lost power rather quickly, turning millions of dollars worth of equipment into useless wandering interstellar objects – rubbish. On the other hand, organic electronics, which usually consist of either small molecules or polymers, started disguised as dyes quite shockingly five years before Becquerel! If we acknowledge that Runge in 1834 had already synthesised aniline which eventually led into the research of Lightfoot and Letheby in the 1860s on polyaniline [12]. Although it was studied for its dye properties and not as we know it today; as a celebrated conducting polymer. Although, the rebranding of polyaniline as an intrinsic conducting polymer would not

come until later on in the 1980s.

1.2.2 Polymers and Anthracene Crystals as forefathers.

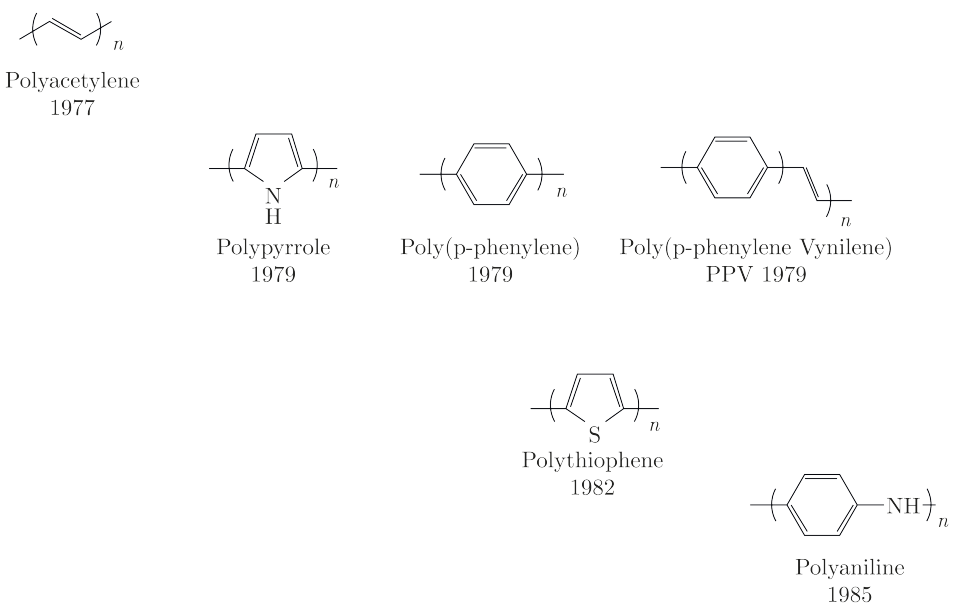

Figure 1.2. Seminal Semiconducting Polymers.

The 1970s saw a decade in what can be called a revolution in science, mainly in chemistry and physics. Just one example would come after the collaboration of the chemists and physicist (Alan MacDiarmid, Hideki Shirakawa and Alan J. Heeger) in 1977 when they discover the metallic behaviour of (PA) under iodine vapour doping as well as other halides [13]. A well known and nicely behaved plastic material proved not to be completely understood. For as been always thought as an insulator it surprised the scientific community when its ability to conduct electric current grew by a mammoth ten orders of magnitude! compared to the insulator regime. This fruitful intellectual union was the result of a curious trained mind and serendipitous everyday experiments, for three years earlier one of Shirakawa's postgraduate research students was reproducing a well established chemical route to produce a certain amount of polyacetylene (PA) when something seemed odd. He had wrongly poured a thousand times the amount of one of the catalysts to the polyacetylene reaction [14]. Then his tutor correctly realized some profound change had taken place in the chemical structure of the polymer. He thought that the electronic structure of the material

was no longer the same from the ordinary PA. When massive amounts of Iodine vapour were introduced (doping), the result was a significant increase in conductivity. Another sign was connected with the optical properties when the usually black polyacetylene powder had turned silvery, implicitly meaning the way the light interacted with the material had changed, which in turn implies an alteration had occurred within the material's intrinsic electronic arrangement: it had a more metallic nature. Baffled by this sudden colour changed, Shirakawa and coworkers kept scavenging answers out of those oddly shiny polymers. On the other hand, from the molecular picture of organic semiconductors, pioneering work led by Hans Kuhn and Bernhard Mann and colleagues reported in 1971, conductivity through monolayers of cadmium salts of fatty acids [15]. Closely related the ideas of attaching "electrodes" to a single molecule and make it work as a rectifier came just three years later in 1974 with the work of Arieh Aviram and Mark Ratner when they presented the first theoretical treatment of transport through a single molecule [16]. And as we have discussed previously electrons in motion create currents, and controlled currents make electronic circuits.

Polymers.

Wudl and collaborators [17–19], fiercely worked synthesising different polymers containing polycyclic structures, one of such offspring was polythiophene. Made from a simple unit of a small five-member ring structure -the thiophene- with a sulfur atom in the 1 position. Roncali [20] makes an extensive revision of the vast literature available on the synthesis, functionalisation and application of polythiophenes (PTP) and more recently in the Handbook of thiophene-based materials by Perepichka & Perepichka [21]. Shortly after, polymers mainly paved the way for one of the most fertile research disciplines. Then polypyrrole, polyaniline, poly(p-phenylene) PPP and poly(p-phenylene vinylene) PVP would become significantly more reported in the scientific literature. And in the case of PVP serendipity too, played a huge role in the first exhibition of polymer electroluminescence [22]. But the evidence of light emission by an organic crystal precedes it by several decades, a single anthracene crystal showed electroluminescence when it was placed under a voltage in 1963 [23], although three years earlier the same group floored the way to charge recombination by the first hole injection into

organic crystals [24].

History shows us then, how rapidly the development of an accidental idea can be transformed into commercial success. So, not surprisingly, during this brief period between the 1980s and 1990s major established chemical companies jumped in the research and development of innovative scientific endeavour. One of those interventions came from the hand of German scientists working at the time (the 1980s) for Bayer when they developed a polythiophene derivative: Poly(3,4-ethylene dioxythiophene) PEDOT. Although initially used as an antistatic coating in photographic films from *AGFA*® [25]. Which is now is part of the most commercially successful semiconducting polymer: PEDOT:PSS whom its applications vary greatly.

Small Molecules

Scientific advancement in chemistry allows us to bind together matter in the form of atoms and molecules, giant macromolecules like DNA and polymers. This is surprising by itself, but what attracts, even more, is that chemists are capable of joining these elemental constituents in a very precise way. This could not be possible without an understanding of *molecular bonding*.

Carbon atoms, the leading element in organic compounds bond through what chemists had defined as hybridisation. In this view, we say that atomic orbitals mix. The purpose of mixing orbitals is to lower the overall energy of the system, *i.e.* bonded atoms have lower energy compared to isolated atoms. We know that the electronic structure of carbon is $1s^2 2s^2 2p^2$, carbon atoms have six electrons and their $1s$ and $2s$ orbitals are fully occupied which leaves only two electrons in their $2p$ orbital. Denoted by $2p_x$ and $2p_y$. Hence these two electrons are ready to make bonds whereas the $1s$ and $2s$ are full so incapable of forming bonds. In this case, carbon atoms would bond only with two other atoms, which clearly is not the case. Instead, one $2s$ electron is promoted to the $2p_z$ orbital that is not occupied hence leaving three $2p$ orbitals and one $2s$ orbitals with unpaired electrons, consequently leaving the atom able to form four covalent bonds [26], which is what happens in *ethylene*, see figure 1.3. The system's energy is reduced as a result of carbon atoms bonding with other carbon atoms. New energy levels are created in order

to satisfy the Pauli exclusion principle.

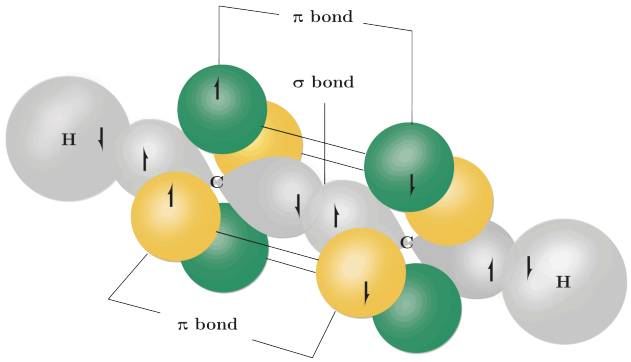

Figure 1.3. Ethylene molecule exemplifying sp^2-type hybridisation.

Aromatic compounds are called this way, for their discovery was first linked with a sweet *aroma*, thus the name. More often than not, this early categorization meant the presence of benzene, see figure 1.4. A small molecule, which is odorous even at low concentration, and of low molar mass. Given its chemical structure, it is non-polar, for hybridized π-electrons are shared equally (temporally and spatially) among the carbon framework. It has long been used as an everyday solvent, although much less now for its highly toxic, and for recent developments on 'green solvents'.

Benzene is depicted in the figure with two equivalent structures, to highlight its relation with the nature of**alternating single and double bonds** (*conjugation* or π-systems[3]) are not fixed in time, they change constantly creating a resonant picture. Our interest relies on the fact that this molecule is treated as the working paradigm of conduction in organic molecules. For we can associate the free movement of electrons around the ring through these hybridised orbitals which overlap and form the so-called π conjugated molecular orbitals. In general, these π-electrons are delocalised within the conjugated backbone of polymers or small molecules.

[3]Key concept in organic semiconducting materials.

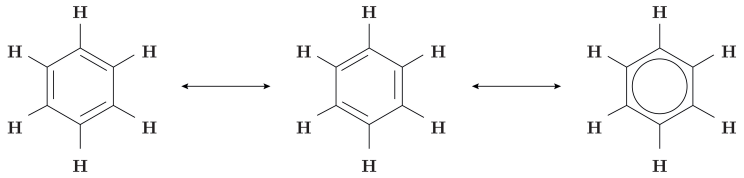

Figure 1.4. Benzene aromaticity.

Anthracene is simply three linearly fused benzene molecules, one can keep adding rings in this fashion to create higher–order *acenes*. To synthesise large acenes is difficult so thus far dodecacene is the longest reported acene molecule to date [27]. Nonetheless, small molecules like these have played an important role in the development of organic photovoltaics where functionalised molecules from perylene, pyrene, porphyrin, phthalocyanine work as organic donors and acceptors [9]. The light-absorbing regions of such dyes are important for device architecture, where several layers of dyes are made in order to capture as many photons as possible at many different wavelengths.

Incidentally, we have returned to the incipient history of organic semiconductors, for thiophene another interesting molecule, and the foundation of this work had a tricky birth. It was supposedly evidence of benzene from 1879 to 1882, during its purification process. Baeyer in 1879 wrongly assumed it was a definite test of the presence of benzene, but it was indophenine which is a deep-blue pigment [21]. The pigment's structure was eventually shown to consist of a form of bithiopene.
So, not surprisingly synthetic routes to make new and to improve known molecules abound the scientific literature. The aim, in this case, is to impart molecules of certain capabilities that the core molecule lacks, for instance, solubility, which aids solution processes like film deposition. When Ebata and coworkers [4] devised the synthesis of BTBT derivatives, they had in mind making the molecule more soluble, to do so they attached alkyl chains to enhance its solubility and also as spacers for adjacent molecules to pack through mutual attractive interactions.

1.3 Top applications

Organic semiconductors of π-conjugated molecules with aromatic and heteroaromatic backbones attract much attention, for their potential applications for low-cost, flexible, and large-area electronic devices. Unlike inorganic semiconductors, in which atoms are covalent-bonded in three dimensions, organic crystals are held together by intermolecular interactions formed through Van der Waals and dipole-dipole interactions, which play important roles in the solid–state. The exact nature of charge carrier photogeneration and its evolution in small–molecule organic semiconductors remain poorly understood due to the difficulties in accessing the intrinsic properties that are often masked by impurities, contact effects, or interface effects [28].

1.3.1 Organic field-effect transistor.

Modern semiconductor technology makes extensive use of transistors as switches and amplifiers in virtually any electronic circuit. Thus, organic field–effect transistors (OFET) as their inorganic counterpart are the building blocks of semiconductors, they drive the research in organic electronics intensely [29]. A transistor is an electronic device that contains three electrodes. The third electrode is used to control the current flow between the other two electrodes; for either to switch or to amplify the signal. The field–effect transistor (FET) is voltage–controlled. A thin–film organic field–effect transistor T-OFET can easily be imagined as a sandwiched layered structure. It consists of three electrodes: the gate, the source and a drain. A layer of dielectric material is always adjacent to the gate followed by a separated layer of semiconducting material that connects the other two electrodes, see figure below. One of the most common architectures is top-gate. This simply means that the electrode located at the top position is the gate followed by a dielectric layer as well as the semiconducting one, illustrated in the figure. In the other arrangement, the components have been inverted and now the bottom of the transistor is the gate, and hence are known as bottom-gate transistors.

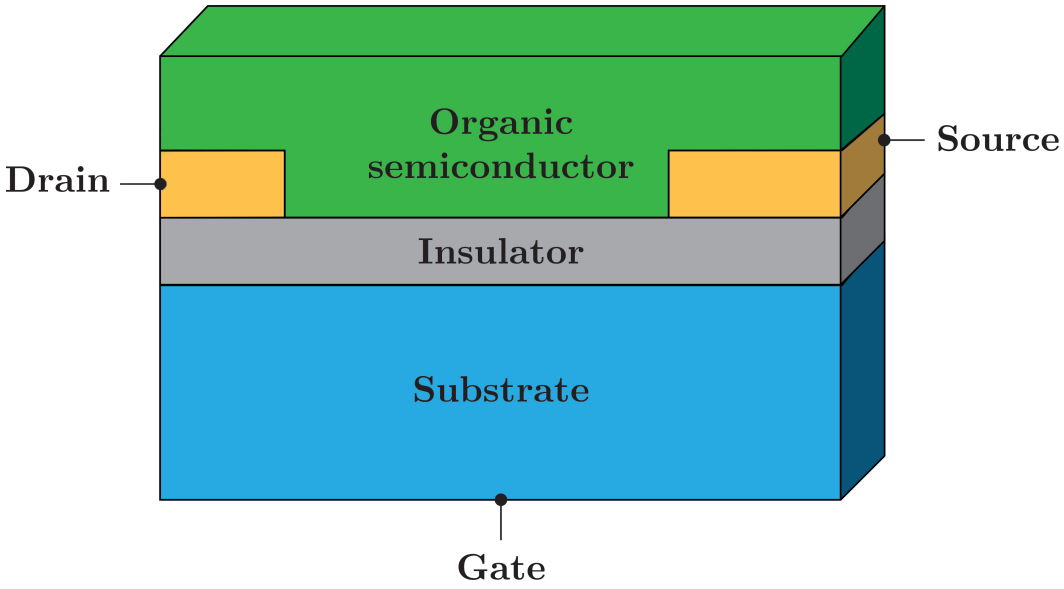

Figure 1.5. Organic Field Effect Transistor, basic device architecture.

1.3.2 Organic light emitting diodes

Like the OFET, organic light–emitting diodes OLED are sandwiched structures, where the semiconducting material is enclosed within two adjacent electrodes. To get light out of this arrangement, one of the electrodes needs to be transparent. One of the most used ones is indium tin oxide (ITO)[4], PEDOT can also be used but this is less common. So, charges flow from the electrodes through the semiconducting material recombine and emit light. It is here, that small chromophore molecules make their way into applications. OLED digital screens in portable phones dominate the market, for example *Samsung* uses them in the *Galaxy* series. Although most of these organic electronics devices are fabricated from vacuum or vapour deposition techniques, solution deposition based on high throughput printing is progressing fast in both displays and lighting [30].

Photochromic molecules are small organic molecules that can undergo reversible photochemical isomerisation between (at least) two (meta)stable states which differ in properties. They can be embedded as an additional component in organic-based materials ready to be exploited in devices such as OLEDs, OFET and possibly in electrophoretic displays [29]. The structurally controlled incorporation of photochromic

[4], In general, any transparent conductive oxide.

molecules can be done at various interfaces of a device, including the electrode/semiconductor or dielectric/semiconductor interface, or even as a binary mixture in the active layer, in order to impart a light–responsive nature to the device.

The photoresponsive nature of these molecular materials, acting as switches, directs the attention of the organic electronics community. Research aiming at developing devices with multiple functionalities. One of these intense and well-funded research lines address the photo-controllable traps, with optical switching applications in mind [31].

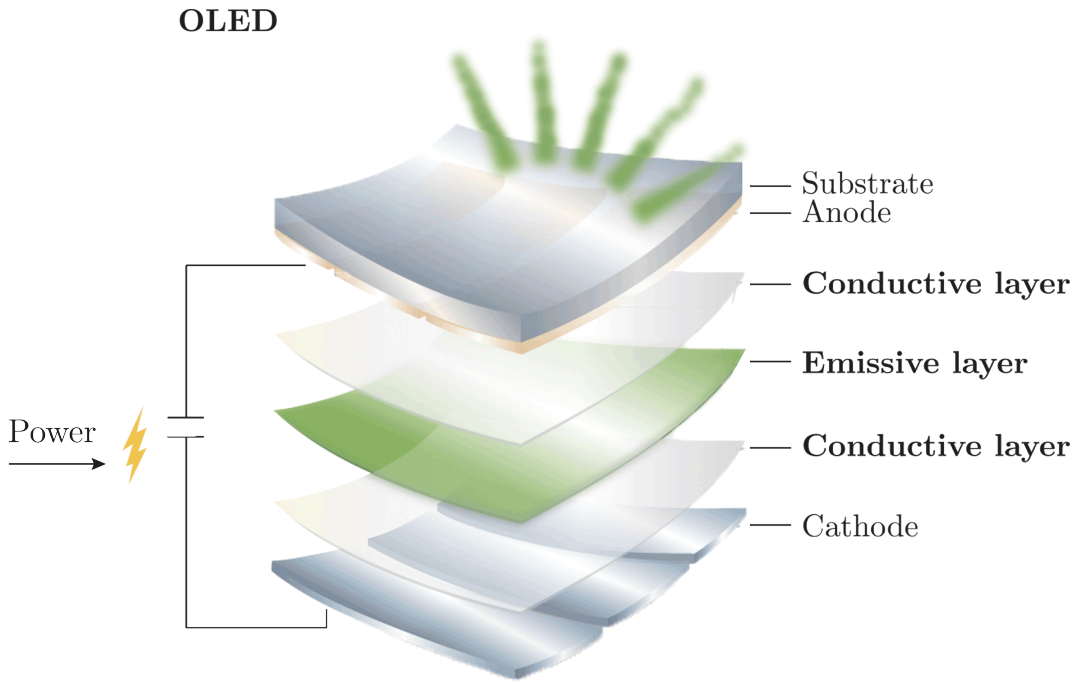

Figure 1.6. Organic Light Emitting Diode, basic device structure.

1.3.3 Organic solar cells

The other famous representatives of organic electronics are organic photovoltaics (OPV). Organic photovoltaics have still a long way to catch with OLEDS in terms of market penetration, despite the fact of having an older

first patent. Tang reported the first solar cell with cellulose as the photoactive material in 1979 [32].
Not much progress was done until the first half of the 1990s when the breakthrough of using the relatively new fullerene molecule was functionalised in the form of [6,6]]-phenyl-C_{61}-butyric acid methyl ester PCBM [33] to replace the less effective previous type-n semiconductor materials in OPV devices. The blend with with poly(3-hexylthiophene) (P3HT) *i.e.* (P3HT:PCBM), dominated the polymer solar cell landscape and is still widely studied many years after first been reported [1]. Although polymer semiconductors dominate OPV research, there is considerable research done with small molecules acting as both donor and acceptor semiconducting materials [9, 28], which in organic terms would be hole conducting layer and electron–conducting layer respectively.

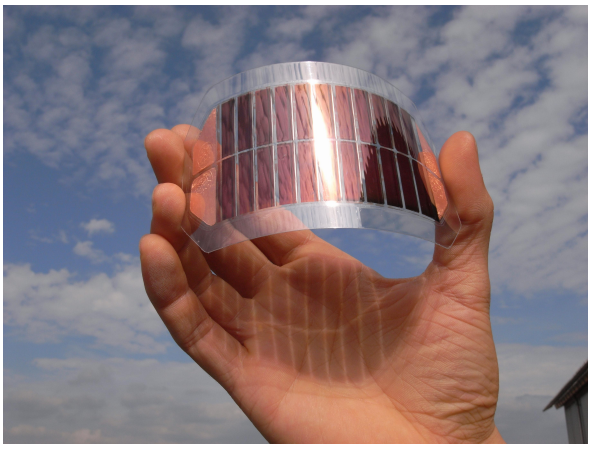

Figure 1.7. Example of a flexible Organic Solar Cell.

For the OPV, what is desired is to easily and effectively dissociate the photo-generated charges. Many device architectures exist but the simplest is where two active layers are adjacent. Both will have to take their respective charges to the collector electrodes, of which one is usually indium tin oxide and gold or silver. So, considerable research, as well as economic resources, has been devoted towards the extraction and control of the excitations formed right in the interface of such layers. Also, in passing we have just mentioned interfaces, which by itself is another subject by its own, so what happens in the boundaries between different media is often of importance.

1.4 Summary

We hope convinced the reader on why *organic seminconductors* studies and optical characterisation, in particular, are instrumental probes in the study of such molecular systems. The OS science has come of age, and has gained terrain in the form of OLED which Its photophysical properties have been largely ignored, however, it is the purpose of this work to bridge the gap in this respect, with ever-expanding the understanding to the optical signatures of the BTBT core. We will concentrate on the solution-based photophysical behaviour of C8-BTBT because in this way we minimise unwanted interaction as well as being as its purest, but we shall also consider briefly small aggregates and thin-films because herein lie interesting applications.

We have established that the study of the optical properties of these materials has not been engaged leaving holes in our understanding of this small thienothiophene containing molecules, this stems primarily on the strong tendency of the field to focus primarily on applications of organic semiconductors. Since the vast majority of those applications are made for devices, is no surprise that the basic photophysics of isolated molecules has been neglected. Our study picks on this gap, where we have systematically addressed these issues; we build our intuition by starting from studies in solution in chapter 4. Proceed then to study the effects brought by substitutions within the backbone molecule in chapter 5, and how these different substituents affect the photophysical behaviour of the backbone and their impact on the intersystem crossing. Finally, in chapter 6 we briefly address the role of controlled aggregation in the optical properties of C8-BTBT, by using state of the art bio–templating techniques, and we study as well the solid–state behaviour through films of C8-BTBT made by molecular beam epitaxy. We compare these results, and observed that the complete quench of the triplet state strongly suggests a suppression of the out–of–plane vibrations, which are responsible for the rapid population of the triplet state seen in the solution studies.

2 Background Theory

We believe that one of the early successes of the nascent quantum theory (∼1910's), was the joy of reconciling early spectroscopic experiments with theory in such a seamless and coherent way. The understanding of the hydrogen emission lines was a paramount expression of the quantised nature of atoms and molecules. It is fair to say that the very nature of light-matter interaction should be entirely addressed quantum physically –matter and light as a quantum particles, hence we should be describing all the phenomena as many particles interacting with each other - ***the quantum many body problem*** *- using only quantum operators and quantum statistics. The truth is that this is so complex and intractable that we cannot even use super-computers to deal with it, so we approximate and make use of simpler models. Thus we treat some parts classically and other bits quantum, both of them with assumptions that simplify the description of the physical process, but still good enough to interpret and explain experimental results in such a way that we keep working with them, as well as creating new technology.*

In this chapter, we are going to describe briefly the theory that will set the stage for properly discussing all the results of our systems. As a caveat to the reader, this thesis is devoted to experiments and their interpretation, based on the scientific literature as updated at the time of submission. So we have deliberately kept the mathematical sophistication to a bare minimum, but hopefully taken care to keep a correct depiction of the physics involved.
Finally, we want to express that the lack of references in this chapter is duly noted. This is due to the nature of the contents, been widely known and for we have taken from many sources: handout notes, lecture notes from previous degrees and my notes on books. Nonetheless, I refer the reader to those few that were cited and reflect more closely our opinion and philosophy on such matters.

2.1 Introduction

All modern discussions of matter start with the omnipresent and omniscient concept of a wavefunction, for nano-scale systems are best described with such framework. All information related to a given system and how it will react to external perturbations originates from it, which is one intrinsic feature of quantum physics.
First, let us acknowledge the impossibility to analytically solve the eigenvalue equation of a system of more than three particles, or as was elegantly put by one of the *Giants* of quantum mechanics:

> *"The fundamental laws necessary for the mathematical treatment of a large part of physics and the whole of chemistry are thus completely known, and the difficulty lies only in the fact that application of these laws leads to equations that are too complex to be solved."*
>
> (Paul Adrien Maurice Dirac, 1930)

So, approximations are needed then, if one wants an estimate for **the energy of the system**, arguably the most important observable of all. We rather discuss everything in terms of a wavefunction because as we will see further below, under certain conditions we can separate the wavefunction and treat parts of it in a separate way which significantly reduces the complexity. Hence, we will only mention some key ideas of molecular wavefunctions although they will be central to our discussion. Here we will exclusively be concerned with the electronic structure of molecules and solids.

2.2 Wavefunctions and Molecular States.

A nonrelativistic electron in a potential $v(\mathbf{r})$ is described with a wavefunction Ψ, by solving the following Schrödinger's equation:

$$\left[-\frac{\hbar^2\boldsymbol{\nabla}^2}{2m_e} + v(\mathbf{r})\right]\Psi(\mathbf{r}) = E\Psi(\mathbf{r}) \tag{2.1}$$

All in all, the full description of the system will be complete only when we supply the explicit form of the potential $v(\mathbf{r})$. In our case, this usually means the dominant Coulombic interactions.

2.2.1 Observables and how to extract information from the Wavefunction

We stated at the beginning of the chapter that all information of a system is contained in its wavefunction, now we consider how such information is retrieved. Quantum mechanics remind us that we can no longer talk about functions representing observables (like position as a function of time), instead, they are represented by mathematical operators (quite often in their matrix representation) [1]. An *observable* is any dynamical variable that can be measured *e.g.* Energy, angular momentum, dipole moment, transition dipole moment, position and momentum to name a few, but the truly instrumental ones are the latter -position and momentum- these two are often term as space representations: real space and reciprocal space respectively.

In a system described by a wavefunction Ψ, we define the mean value of the observable Ω in a series of measurements to be equal to the expectation value of the corresponding operator. Such expectation value of the operator $\widehat{\Omega}$ is denoted $\langle \Omega \rangle$ and is generally given by the following equivalent expressions:

$$\langle \Omega \rangle = \frac{\int \Psi^* \widehat{\Omega} \Psi \, d\tau}{\int \Psi^* \Psi \, d\tau} = \frac{\left\langle \Psi \middle| \widehat{\Omega} \middle| \Psi \right\rangle}{\langle \Psi | \Psi \rangle} \tag{2.2}$$

When wavefunctions are normalised to unity[2] and where τ is a normalised dimensionless volume element, then the expectation value expression reduces to,

$$\langle \Omega \rangle = \int \Psi^* \widehat{\Omega} \Psi \, d\tau = \left\langle \Psi \middle| \widehat{\Omega} \middle| \Psi \right\rangle \tag{2.3}$$

This mathematical representation of the action of measuring *any* observable of the system, has a physical interpretation. It says that when we go and measure any observable of the system, we inherently disturb it solely to the act of observing it. Although this action needs to be done in order to measure any given value of any given observable, so the physical consequence of measuring is that we care of what comes after the measurement and not to what happened before, which means, we do not care the state previous to our measurement.

[1] Or Matrices, hence the old fashion way to referrer to quantum mechanics as "Matrix Mechanics".

[2] Unless we state otherwise, from now on we shall assume that the wavefunctions are normalised to 1.

2.2.2 The Hamiltonian Operator

The fundamental equation of motion for a non-relativistic quantum mechanical system is the time-dependent Schrödinger equation which reads

$$\widehat{H}(\mathbf{r},t)\,|\Psi(\mathbf{r},t)\rangle \;=\; i\hbar\frac{\partial}{\partial t}\,|\Psi(\mathbf{r},t)\rangle \tag{2.4}$$

Where $\widehat{H}$ and $|\Psi\rangle$ are the Hamiltonian and the wavefunction of the system respectively, $\mathbf{r}$ denotes the coordinates of all the particles in the system. The Hamiltonian $\widehat{H}$ is the operator describing the energies and interactions between all particles of the system, which recalling from equation 2.1. Is what multiplies the Ψ (or $|\Psi\rangle$) from the left-hand side. When this instrumental operator does not explicitly depend on time (t), then we have the *time independent Schrödinger equation* which can be written as

$$\widehat{H}(\mathbf{r})\,|\Psi(\mathbf{r})\rangle = E\,|\Psi(\mathbf{r})\rangle \tag{2.5}$$

where E is the total energy of the system. This result communicates the value of the energy if we supply the Hamiltonian: which is the sum of the kinetic energy and the potential energy operators. The kinetic energy always look the same, so the true characteristic of any given system will be encoded in the mathematical form of its potential, regardless if it will be of an atom or a molecule or a crystal.

2.2.3 Dipole Operator and Transition Dipole Moment

Among many of the simple yet elegant concepts of physics, the *electric–dipole* stands-out. It is related to charges in general; from point charges to charged molecules and solids. Responsible for many fundamental processes: *e.g.* polarisation, polarisability and particularly in the core of the Van der Waal forces which are at the kernel of organic crystals formation [34]. Two neutral molecules interact through the van der Waals forces, observing the fact that the molecules have no static dipole moment, rather a charge distribution that is not fixed. A time–dependent fluctuation in the charge distribution in a molecule implies an associated temporary fluctuating dipole moment. An adjacent molecule feeling this temporal fluctuation will exhibit a corresponding fluctuating dipole induced by the first molecule. The electrostatic interaction between the correlated fluctuating dipoles in the molecules results in an attractive

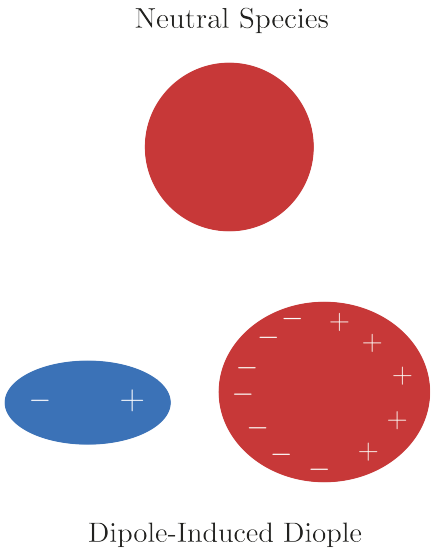

Figure 2.1. Schematic representation of an induced dipole.

force –the van-der-Waals force.

From electromagnetism, we know than an oscillating field induces a corresponding oscillating field within a dipole, so when we approximate the system as a dipole, we remember that dipoles are characterised by their dipole moment, a vector quantity in classical physics. From which we build the quantum operator.

let us consider the simplest case, the quantum dipole operator for an electron

$$\widehat{\boldsymbol{\mu}} = e\mathbf{r} \tag{2.6}$$

Where 'e' represents the elementary charge. For electronic motion in a molecule, the dipole moment operator is slightly modified

$$\widehat{\boldsymbol{\mu}} = e\sum_i Z_i \mathbf{r}_i \tag{2.7}$$

So the *transition dipole moment* for a transition between states Ψ_i[3] and Ψ_f is defined for both the electron and the molecular cases as

$$\widehat{\boldsymbol{\mu}}_{if}^{e} = \langle \psi_i | \, \widehat{\mathbf{r}} \, | \psi_f \rangle \tag{2.8a}$$

$$\widehat{\boldsymbol{\mu}}_{if}^{mol} = \left\langle \Psi_i \left| \sum_j Z_j \widehat{\mathbf{r}}_j \right| \Psi_f \right\rangle \tag{2.8b}$$

where $\mathbf{r}_j$ is the position of the vector of the *j*-th particle and the Z_j is the charge on this particle. The sum *j* is over all electrons and nuclei in the molecule.

The transition dipole moment can be regarded as a measure of the size of the electromagnetic impulse that the electron receives from the electromagnetic field when it makes a transition between states. The coupling between an electromagnetic wave and an electronic transition with transition dipole moment $\widehat{\boldsymbol{\mu}_{if}}$ depends on the charge distribution within the molecule, the strength of the electric field, and the relative polarizations of the field and the transition. Additionally, the transition dipole moment depends on the molecular geometry of initial and final states.

2.2.4 Density Operator

Among the observables that are calculated in the way described in section 2.1.1, one of ***fundamental*** importance is the particle density (ρ). Which can easily be associated with the *charge–distribution* or *charge–density* within molecules and solids. So, we can roughly know where does the electron cloud is distributed which is all related to the molecule's geometry. In its simplest form, the density operator is

$$\widehat{\boldsymbol{\rho}} = \sum_j p_j \, |\psi_j\rangle \, \langle \psi_j| \ , \tag{2.9}$$

Where the coefficients p_j are non-negative and add up to one. This represents a mixed state, with probability p_j that the system is in the pure state $|\psi_j\rangle$. For an N-electron system we modify slightly and express

[3] We have chosen to label "i" with initial state and "f" for the final state.

the electron density in terms of the wavefunction as

$$\widehat{\boldsymbol{\rho}}(\mathbf{r}) \;=\; N \int d\mathbf{r_2}...d\mathbf{r_N}|\Psi(d\mathbf{r}, d\mathbf{r_2}, ..., d\mathbf{r_N})|^2 \tag{2.10}$$

This observable is of instrumental importance when dealing with much more robust formalism like Density Functional Theory (DFT). All this is done by promoting the particle density $\widehat{\boldsymbol{\rho}}(\mathbf{r})$ from just one among many observables to the status of *key* variable, on which the calculation of all other observables can be based, see [35].
The DFT approach can be summarised by the sequence

$$\boldsymbol{\rho}(\mathbf{r}) \Longrightarrow \; \Psi(\mathbf{r}_1, \mathbf{r}_2, ..., \mathbf{r}_n) \; \Longrightarrow \; v(\mathbf{r}) \tag{2.11}$$

i.e. knowledge of $\boldsymbol{\rho}(\mathbf{r})$ implies knowledge of the wave function and the potential ($v(\mathbf{r})$), and hence of all other observables. Although this sequence describes the conceptual structure of DFT, it does not really represent what is done in actual applications of it, which typically proceed along rather different lines, and do not make explicit use of many–body wave functions, see for instance [36].

2.3 Electron Spin

So far, we have obviated the fact, that with this formalism of non-relativistic quantum mechanics some issues are not addressed at all, and in so doing, we have neglected one of the most inherent features of quantum mechanics and instrumental to our work, namely –*the electron spin*.
Shortly after the quantum mechanics was developed, Goudsmith and Uhlenbeck in 1925 at Leiden University suggested that the electron was spinning around its own axis, an *intrinsic* angular-momentum calling it '*spin angular-momentum*' or more simply: ***spin*** [37]. In the Dirac formalism of quantum mechanics, this is taken into account, unfortunately at great expense in mathematical sophistication and computing complexity. Such formalism lies outside the scope of this thesis so we will not mention it further, nonetheless, *spin*–related processes are central to our discussion. For a more appropriate introduction to this section see the excellent texts of *Molecular Quantum Mechanics*[38] and

Atoms, Molecules and Photons. [39].

The foremost impact of electronic spin is reflected in the Pauli-exclusion principle, a fundamental postulate of quantum mechanics. It can be stated as follows:

The total Wavefunction must be antisymmetric with respect to the interchange of any electron pair[4].

Due to electrons being indistinguishable, $|\Psi|^2$ must be invariant with respect to an interchange of any pair of electrons, because the probability of finding an electron in a volume element must be the same when the electrons are exchanged. Both symmetric and antisymmetric wavefunctions would satisfy this condition, but the Pauli principle allows only antisymmetric wavefunctions. The product of two symmetric or two antisymmetric functions is symmetric, that of a symmetric and antisymmetric function is antisymmetric.

The intrinsic non-zero angular momentum *spin* s of electrons is unconnected to their motion in space, and plays a major role in the description of any given quantum system. For electrons, the *spin* can take the values of $s = \pm 1/2$, and it usually appears depicted equivalently as *spin–up* ($\uparrow$ or α) and *spin–down* ($\downarrow$ or β). The spin does not appear in the Schrödinger equation, so, it has to be introduced *ad hoc* in non-relativistic quantum mechanics. This is usually done by defining a spin operator $\widehat{S} = (\widehat{s_x}, \widehat{s_y}, \widehat{s_z})$ that acts only on the spin coordinates s of the electrons. Then the wavefunction $|\Psi(\mathbf{r}, s)\rangle$ can be expressed as a product of a spatial wavefunction and a spin-wavefunction $|\psi_s\rangle$,

$$|\Psi(\mathbf{r}, s)\rangle \; = \; |\Psi(\mathbf{r})\rangle \times |\psi(s)\rangle \tag{2.12}$$

The spin-dependent functions $|\psi(s)\rangle$ are orthogonal for different spins s, i.e., $\langle\psi(s)|\,\psi(s')\rangle = \delta_{ss'}$. Thus, all couplings of electronic wave functions of different spin value are zero, and, as a consequence, transitions between electronic states of different spin value are forbidden at this level of theory.

[4] More commonly encounter as: "No two electrons can have the same quantum numbers"

2.3.1 Spin States

The *spin* of a given state comes from the total–*spin* for all the electrons occupying available orbitals. Fortunately, there is no need to count them all, for in all *fully-occupied* orbitals, electrons are paired with anti-parallel spins and so the net contribution to the total spin is zero. That is the reason we concern ourselves only with the unpaired electrons[5] of an excited state, usually one electron in a π^*-orbital and one in a π-orbital. When the spin of the electron in the π^* orbital and that of the remaining electron in the π-orbital are anti-parallel, we label it a *singlet* state, adding up to a total spin of zero. When the arrangement leads to having electrons with parallel spins we say they are in a *triplet* state and so they add up to a total spin of one in units of $\hbar$. Note that for the triplet wavefunctions, the spins are always in phase, while they are 180° out of phase for the singlet state. We label excited states in energetic order, that is, S_1, S_2, or T_1, T_2, and so on, for the energetically lowest or second-lowest singlet or triplet excited state[6]. Spin angular momentum is a vector quantity that follows the rules of quantum mechanics. The convenience of using the ideas of molecular orbitals is highlighted when we simplify the discussion on the spin of electrons in the HOMO and LUMO to a two-particle system that forms the configuration dominating the excited state. So, we focus on the unpaired electrons in the π^* and the π orbitals. From basic quantum mechanics, we know that two particles with spin angular momentum have simultaneous eigenstates to $\widehat{\mathbf{S}}^2$ and $\widehat{S_z}$ with eigenvalues S and M_s, where $\widehat{\mathbf{S}}$ is the spin angular momentum operator, and $\widehat{S_z}$ denotes its z-component. For the two-particle-system, there are four such eigenstates. There are three different ways parallel spins can be aligned to yield a total spin $S = 1$ hence these states are collectively called 'triplets'. In contrast, there is only one way to make the total spin $S = 0$, and we call it a singlet. Without a magnetic field, the $\widehat{S_z}$ cannot be defined, which means that M_s will no longer be a good quantum number. In the absence of a magnetic field, the four linearly independent and orthonormal spin eigenstates of a

[5] Regardless of orbitals types and/or labels.

[6] Even in the absence of a magnetic field, the three triplet sublevels are not degenerate. Rather, they are separated by small energy, called the *zero-field splitting*.

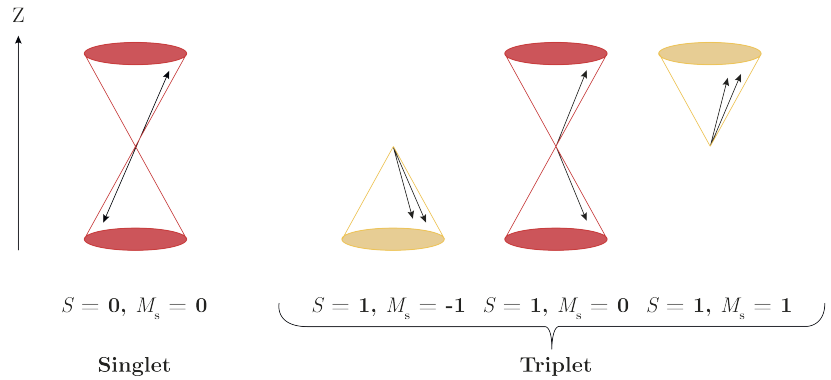

Figure 2.2. Singlet and Triplet States, spin configurations.

two-particle-system can be expressed as follows

$$\begin{cases} \Psi_{T_x} = \dfrac{1}{\sqrt{2}}(\beta_1\beta_2 + \alpha_1\alpha_2) & \text{(2.13a)} \\ \Psi_{T_z} = \dfrac{1}{\sqrt{2}}(\alpha_1\beta_2 + \beta_1\alpha_2) & \text{(2.13b)} \\ \Psi_{T_y} = \dfrac{i}{\sqrt{2}}(\beta_1\beta_2 + \alpha_1\alpha_2) & \text{(2.13c)} \end{cases}$$

$$\Psi_S = \frac{1}{\sqrt{2}}(\alpha_1\beta_2 - \beta_1\alpha_2) \qquad \text{(2.13d)}$$

Where α and β denote the spin wavefunctions of the one-electron states and the index 1 and 2 refer to electron 1 and 2.
In order to preserve the Pauli exclusion principle, the total wavefunction for two fermions (half integer quantum particles) must be antisymmetric with respect to particle exchange. The symmetric spin wavefunctions of the triplet state are always combined with an antisymmetric electronic wavefunction, whilst for the singlet, the antisymmetric spin wavefunction must be coupled with a symmetric spatial wavefunction.

2.4 The Born-Oppenheimer Approximation and potential energy surfaces (PES)

The physical basis for the Born-Oppenheimer approximation [40] is the fact that the mass of the atomic nuclei in molecules are much

larger than the mass of the electrons[7]. Because of this difference, the nuclei move much more slowly than the electrons, hence electrons can respond almost instantaneously to displacements of the nuclei. Also, due to their opposite charge, there is a mutually attractive force of $\sim \frac{Ze^2}{r_{jk}^2}$ acting on an atomic nucleus and an electron, where r_{jk} is the distance between them. Where we refer to the j-th electron and the k-th nucleus. This force causes both particles to accelerate, since the magnitude of this acceleration is inversely proportional to the mass, resulting in a significantly greater acceleration for the electrons than the one imparted to the nuclei. Consequently, the electrons are moving and responding to forces very quickly, whilst the nuclei are not. Therefore, instead of trying to solve the Schrödinger equation for all the particles simultaneously, we approximate the molecular wavefunction by regarding the nuclei fixed in position, i.e. they are stationary. Then we solve the Schrödinger equation for the electrons in the static electric potential arising from the nuclei in that particular arrangement[8]. The nuclei, however, can be stationary at different positions so the electronic wavefunction can depend on the positions of the nuclei even though their motion is neglected.

The Hamiltonian for a molecule will naturally include kinetic energy terms for the nuclei and electrons, the attractive term between the electrons and the nuclei, the term for the electron repulsion and the last term the potential energy of nuclear repulsion. Mathematically we express this as follow:

$$\widehat{H} = -\frac{1}{2}\sum_k \frac{1}{M_k}\boldsymbol{\nabla}^2 - \frac{1}{2}\sum_i \frac{1}{m_i}\boldsymbol{\nabla}^2 - \sum_i \sum_k \frac{Z_k}{r_{ik}} + \sum_{i\neq j} \frac{1}{r_{ij}} + \sum_{k\leq l} \frac{Z_k Z_l}{R_{kl}} \tag{2.14}$$

[7]Just the proton-electron mass ratio is $\frac{m_p}{m_e} \approx 1830$.

[8]This is also called the adiabatic approximation. The term adiabatic comes from considering the change in nuclei position as work been done on the molecule, without any abrupt change in electronic configuration.

This operators are so important that we are going to label them separately;

$$\widehat{T}_{ele} = -\frac{1}{2}\sum_{k}\frac{1}{M_k}\boldsymbol{\nabla}^2 \tag{2.15a}$$

$$\widehat{T}_{nuc} = -\frac{1}{2}\sum_{i}\frac{1}{m_i}\boldsymbol{\nabla}^2 \tag{2.15b}$$

$$\widehat{V}_{e-e} = \sum_{i\neq j}\frac{1}{r_{ij}} \tag{2.15c}$$

$$\widehat{V}_{n-n} = \sum_{k\leq l}\frac{Z_k Z_l}{R_{kl}} \tag{2.15d}$$

$$\widehat{V}_{n-e} = \sum_{k}\frac{Z_k}{r_{ik}} \tag{2.15e}$$

Although the complete Hamiltonian for a molecule can be determined, the resulting Schrödinger equation is impossible to solve analytically. Hence, the electron motion is determined for a fixed position of the nuclei making the distances (R_{kl}) in equation 2.14 now a constant. This is the Born-Oppenheimer approximation. The approximation removes the kinetic energy operators for the nuclear motion in equation 2.14, *i.e.* the $\widehat{T}_{nuc}$.

$$\widehat{H} = \widehat{T}_{ele} + \widehat{V}_{e-e} + \widehat{V}_{n-e} + \widehat{V}_{n-n} \tag{2.16}$$

The resulting Schrödinger equation becomes just the electronic Schrödinger equation for the molecule plus a constant term for the nuclear repulsion. Consequently, the total molecular wavefunction can, therefore, be described as a product of two wavefunctions; a wave function for the nuclei and one for the electrons. Hence $\Psi(\mathbf{r};\mathbf{R}) \equiv \psi_{ele}(\mathbf{r};\mathbf{R})\psi_{nuc}(\mathbf{R})$. Where the notation $(\mathbf{r};\mathbf{R})$ means that the wavefunction for the electron is a function of its position $\mathbf{r}$ and depends parametrically on the coordinates of the nuclei $\mathbf{R}$. Solving the Schrödinger equation for different arrangements of nuclei allows us to construct the molecular potential energy surface, and to identify the equilibrium geometry of the molecule with the lowest point on this surface see figure 2.3. The wavefunctions that result in the computation are called molecular orbitals (MO).

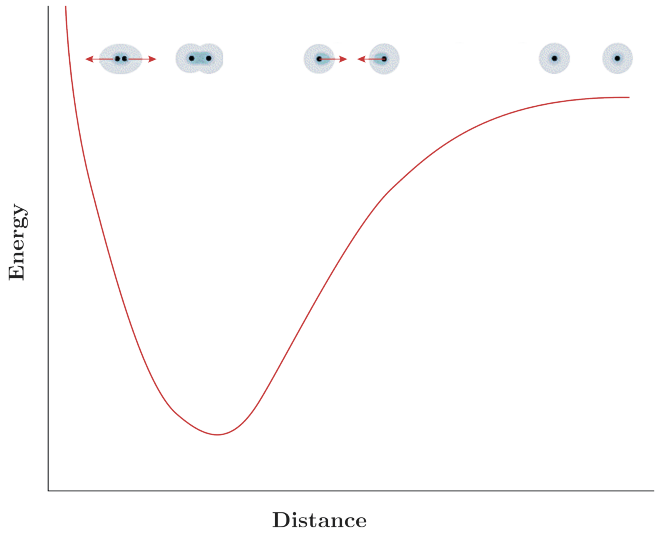

Figure 2.3. Potential energy surface curve for the H_2-molecule as a function of the distance between nuclei. Atoms are dissociated at larger distances and upon approximation, bonding forces bring them closer, the equilibrium geometry is achieved when they rest in the minima of the PES.

2.4.1 Corollary of the BOA: Franck-Condon Principle.

In the previous section, we have laid down the modern foundations of the Born-Oppenheimer approximation, its widespread use is often the starting point for any modern quantum mechanical calculation. Now we direct our attention to some of its implications, in particular for organic molecules. In these cases, the most important perturbation for *mixing* wavefunctions is the vibrational nuclear motion that is coupled to the orbital motion of the electrons - called the *vibronic–coupling*. We can think of this coupling as a distortion of the wavefunction that gives rise to non-vanishing terms in the matrix elements of the transition.

In other words, the Franck-Condon principle is the approximation that an electronic transition is most likely to occur without changes to the position of the nuclei in the molecule, hence the term *vertical transition*. In terms of quantum mechanics, this principle says that the probability of a vibrational transition is proportional to the square of the overlap integral ($|\langle\chi_i|\ \chi_f\rangle|^2$) between the vibrational wavefunctions of the two states involved in the transitions *e.g.* initial vibrational (χ_i) and final vibrational (χ_f) states. The Franck-Condon factor is a measure of the overlap of the vibrational wavefunctions, the most probable transition occurs when the wavefunctions overlap the most.

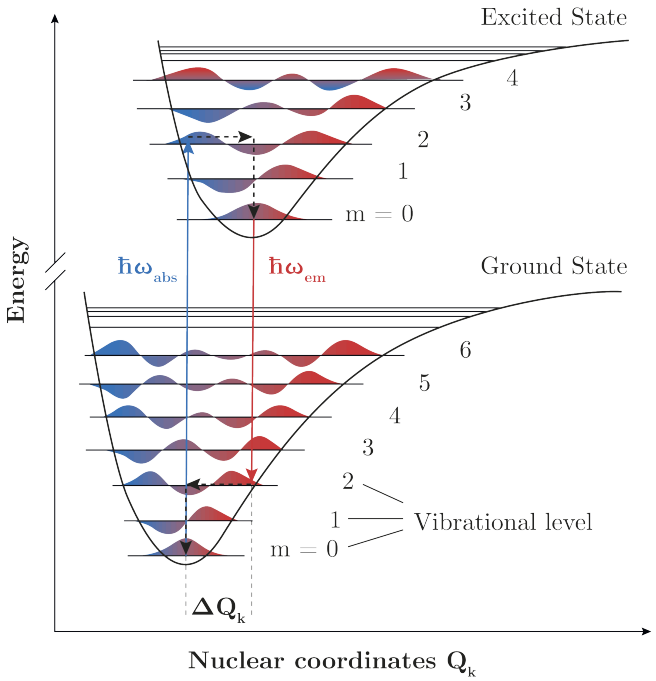

Figure 2.4. Illustration of the Franck-Condon principle. The vertical blue arrow represents absorption while the red arrow represents emission. ΔQ, stands for the difference in minima nuclear coordinates.

Spectroscopic minima are also called Franck-Condon minima for they are related to the absorption of photons. Excitation energy takes an electron from one potential energy surface PES minimum to an excited PES minimum, i.e. from minimum to minimum, hence the name *vertical transitions*. But the important remark here is that these so-called Franck-Condon minima also relate the molecular geometries of the states involved (mainly the initial (i) and final (f) states) in the transition induced by optical excitation, so for those particular states for whose geometries as well as their energies in the ground and excited state are similar have the highest probabilities to take place.

Huang-Rhys Parameter.

Further in this work we will benefit greatly from a parameter called the *Huang-Rhys* parameter, so it will be time well invested in exploring its relation with the Franck-Condon principle. Quite usefully we can relate the nuclear displacements with this parameter, defining an *equilibrium*

coordinate–Q (remember from figure 2.4), which its origin corresponds to the minimum of the potential energy surface and consequently the equilibrium geometry of the molecule. Thus, deviations from the *equilibrium geometries* can be expressed as ΔQ, when the oscillation of the normal mode is treated as a single harmonic oscillator with reduced mass M, force constant $k = M\omega^2$, and angular frequency ω_m, the Franck–Condon factor can be related to the change in equilibrium coordinate ΔQ by

$$I_{0-m} = |\langle \nu_0 |\, \nu_\mathrm{m} \rangle|^2 = \frac{S^m}{m!} e^{-S} \tag{2.17}$$

with

$$S = \frac{1}{2} k \frac{\Delta Q^2}{\hbar \omega_m} = \frac{1}{2} M \omega_m \frac{\Delta Q^2}{\hbar} \tag{2.18}$$

Where S is called the *Huang-Rhys parameter*. In chapter 4 we will see why we need to remember that real molecules necessarily imply more than single modes of vibrations, in particular for our studies *out–of–plane* (OOP) vibrations are of instrumental importance and to a lesser extent the in-plane vibrations too. For instance, in small oligothiophenes Kölle *et al* [41] demonstrated that between the second lowest triplet state T_2 and the lowest singlet state S_1 mediates an intersystem crossing path. This ISC turns to be enabled through coupling induced by torsional out of plane motion of the S_1 state dynamics. Hence, we see why several vibrational modes m_i need to be taken in to account, this usually involves modifying the expression in eq.2.17 to reflect this fact

$$I_{0-m_i} = \frac{S^{m_i}}{m_i!} e^{-S_i} \tag{2.19a}$$

$$S_i = \frac{1}{2} M_i \omega_{m_i} \frac{\Delta Q_i^2}{\hbar} \tag{2.19b}$$

From the previous equation we can express S as the quotient of the 0-0 to the 0-1 vibrational transition, *i.e.*

$$S = \frac{I_{0-1}}{I_{0-0}} \tag{2.20}$$

If we examine the expression in eq.2.18 we could further associate the Huang-Rhys parameter with the number of quanta involved in the vibrational transition, for we can take S as a measure for the ratio between the potential energy associated with a vibrational excitation, $k\Delta Q^2/2$ and the energy of the vibrational quanta, $\hbar\omega_m$. What this physically means in the case of absorption, is that upon absorption of photons

molecules recently excited will still have their ground state equilibrium geometry, only after emission of vibrational quanta is that the nuclei can adapt to changes in charge distribution, and the system reaches the new equilibrium geometry of the excited state. In other words, transitions take place vertically, which implies that molecules in the excited state are instantaneously in the equilibrium geometry of the ground state, then within ps molecules reach the equilibrium geometry of the excited state, conversely, immediately after emission of photons molecules in the ground state are instantaneously in the equilibrium geometry of the excited state, and within ps molecules reach their ground state equilibrium geometry[9].

2.4.2 Linear Combination of Atomic Orbitals

Based on the previous analysis, it is reasonable to construct the molecular orbitals from a *linear combination of atomic orbitals* (LCAO). Another reason for making further approximations comes from the fact that we already have good atomic orbitals for many-electron atoms, and it seems appropriate to try to use them as a starting point for the description of many-electron molecules built from those atoms. We have already informally used this when discussing the origin of p-type orbitals as a result of hybridisation and mix of atomic orbitals. This mixing takes the mathematical form of

$$\psi = \sum_i c_i \phi_i \,. \tag{2.21}$$

The terms c_i are coefficients indicating the magnitude of the contribution of each atomic orbital ϕ_i to the molecular orbital. The coefficients c_i need to be determined by solving the Schrödinger equation using the variational principle, another requirement is that $\sum_i c_i = 1$ to guarantee the normalisation of the wavefunction. To produce a precise molecular orbital, a great number of $\{\phi_i\}$ should be used. Of course, in practice, only a finite basis set is used. As this cannot be solved analytically for more than one electron (because the electrons are moving), one considers the hypothetical case of a molecule with only one electron. The molecular

[9]When optical transitions take place, systems are said to be in Franck-Condon minima, and the energy difference between equilibrium geometries and F-C minima are referred as the *reorganization energy*.

orbitals thus obtained are one-electron orbitals. The associated many-electron molecular wavefunction, corresponding to the ground state is constructed by multiplication of the molecular one-electron orbitals,

$$\Psi = \prod_i \psi_i \,. \tag{2.22}$$

Among all the molecular orbitals two of particular importance are the *highest occupied molecular orbital* (HOMO) and the *lowest unoccupied molecular orbital* (LUMO). Knowing their energies is important for a materials scientist, for instance, someone interesting in adding an electron–conducting layer either for a solar cell or for an organic light–emitting diode. The energetic difference among these molecular orbitals is commonly referred as the "HOMO-LUMO-gap", $E_{gap} = |E_{\text{HOMO}} - E_{\text{LUMO}}|$. For our purposes, we are only concerned about this value, and not the exact energies of the molecular orbitals.

Excitons

The older term *exciton* should only be used in the context of a highly ordered system for it was developed by the Soviet physicist Yakov Frenkel in 1931 for treating excited atoms in crystal lattices [42]. Yet by now, the tradition has evolved of using the terms "excitation" and "exciton" as synonyms, since formally the term means an excitation that is delocalised over more than one molecule, or that moves rapidly from molecule to molecule.

When an organic material is excited externally either by light or by an electric field a particular type of excited state forms in the organic semiconductor, the exciton.

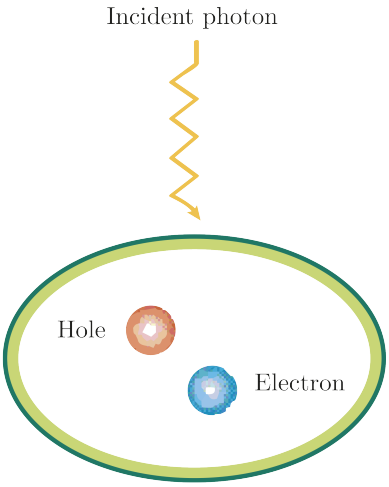

Figure 2.5. Pictorial representation of an exciton. The ellipse represents the coulombic force that binds the pair and also to denote its size.

This means that for instance, optical excitation creates a pair of electron and a *hole* –the absence of a negative charge that the electron leaves behind when promoted– In organic semiconductors, this mechanism works like this: an electron that has been promoted to the π^* orbital, or LUMO, remains bound to the positively charged 'hole' in the π orbital, HOMO. The result is an electrically-neutral quasi-particle, strongly-bound via coulombic interactions, and relatively localised on the order of a few nm [34]. Low dielectric constants of organic materials make the screening between charges less effective than in inorganic materials. Thus the exciton size is dictated not by the electron-hole Coulomb interaction, but by the physical dimensions of the material or the arrangement of distinct building blocks. Furthermore, the exchange interaction (singlet–triplet splitting) is a good measure of the exciton size [43]. Excitons are often treated in the two limiting cases of small dielectric constant versus large dielectric constant; corresponding to Frenkel exciton and Wannier-Mott exciton respectively. In Wannier-Mott excitons, the electron and hole can be on separate molecules, although they usually are not far apart [44]. For organic photovoltaics, a primary focus is finding effective ways of overcoming the Coulomb binding in excitons so that free charges can be extracted.

2.5 Transitions between states.

The rate of an electronic transition, depends on the spatial overlap between initial (Ψ_i) and final (Ψ_f) state wavefunctions[39]. This transition rate is independent of time as long as the originating perturbation is independent too, and is proportional to the coupling between the initial and final states of the system as well as the density of states. To calculate a transition rate, all that it is needed is to multiply the square modulus of the transition matrix elements between the two states by the density of states. This succinct expression is called Fermi's golden rule.

A $\pi - \pi^*$-transition promotes an electron from a π-HOMO to a π^*-LUMO, when both orbitals are delocalised over a similar area of the molecular backbone. The overlap is reduced when the HOMO and the LUMO are located on the different regions of the molecule, as occurs in the case of a charge-transfer state (CT) transition [43]. In our case, the matrix elements result from the interaction of the dipole moment operator and applied electric field operator. The transition probability per unit of time from the initial state $|\Psi_i\rangle$ to a final state $|\Psi_f\rangle$ is given by

$$\text{Rate of transition} = \; k_{if} = \frac{2\pi}{\hbar} \left|\langle \Psi_f | \, \widehat{\boldsymbol{\mu}} \, | \Psi_i \rangle\right|^2 \rho \; . \tag{2.23}$$

Where ρ is a density of states.

2.5.1 Origin of Transitions Selection Rules

It follows from the Born-Oppenheimer approximation that the total molecular wavefunction is going to be split three-way: electronic and vibrational degrees of freedom as an additional term for the spin wavefunction that is independent of the electronic and nuclear coordinates, *i.e.* we can write this molecular wavefunction as $\Psi_{Total} = \psi^{elec}\,\psi^{vib}\,\psi^{spin}$ and after inserting this expression in the definition of the *transition dipole moment* from equation 2.23, some important selection rules for optical transitions emerge.

$$k_{if} = \frac{2\pi}{\hbar} \left|\langle \Psi_f | \, \widehat{\boldsymbol{\mu}} \, | \Psi_i \rangle\right|^2 \rho \tag{2.24a}$$

$$= \frac{2\pi}{\hbar} \left|\left\langle \psi_f^{elec} \right| \widehat{\boldsymbol{\mu}} \left| \psi_i^{elec} \right\rangle\right|^2 \left|\left\langle \psi_f^{vib} \right| \psi_i^{vib} \right\rangle\right|^2 \left|\left\langle \psi_f^{spin} \right| \psi_i^{spin} \right\rangle\right|^2 \rho \tag{2.24b}$$

We have used the fact that the dipole operator acts only on the electronic wavefunction, sometimes also called the Condon approximation. Physically, the incident electromagnetic wave with its time-dependent electrical dipole causes only the electrons to move in resonance. The nuclei move too slowly to respond to optical frequencies and the spins are not affected by the changing electric field. So, the spin wavefunction and the vibrational wavefunction are unaffected by the dipole operator. They can therefore be treated like constant factors. The spin term demonstrates that optical transitions can only occur between states of the same total spin; direct transitions from singlet to triplet states or vice versa are forbidden at this level of theory.

So, for a given transition to be allowed all three terms must be non-zero. The rate of optical transitions, therefore, depends on three factors: the electronic factor, the vibrational factor and the spin factor.

Electronic Factor.

Let us first turn to the integral $\left|\left\langle \psi_{\mathrm{f}}^{elec}\right|\widehat{\boldsymbol{\mu}}\left|\psi_{\mathrm{i}}^{elec}\right\rangle\right|^{2}$. If this expression is different from zero, the transition is said to be *dipole-allowed*, otherwise it is *dipole-forbidden*. Also, note from the expression that the value of the integral scales with the overlapping of the initial and final wavefunctions, and finally the integral will scale with the value of the transition dipole moment $\widehat{\mu}$.

Vibrational Factor.

The electronic part, mainly controls the intensity of the transition but the overlap of the vibrational wavefunctions $\left(\left\langle \psi_{\mathrm{f}}^{vib}\right|\left.\psi_{\mathrm{i}}^{vib}\right\rangle\right)$ is what controls the spectral shape of both absorption and emission. Ground–state absorption always takes place from the zeroth vibrational level, this is because at room temperature there is not enough thermal energy to populate higher states. The *Franck-Condon-overlap-integral* relates to the overlap of the initial and final vibrational wavefunctions, which governs the intensity of the transitions. And the square of it, $\left|\left\langle \psi_{\mathrm{f}}^{vib}\right|\left.\psi_{\mathrm{i}}^{vib}\right\rangle\right|^{2}$, is called the *Franck-Condon-factor*. It can be understood as the probability of the transition from the zeroth vibrational level of the ground state to the m-th vibrational level of the excited state, sometimes expressed as I_{0-m}[34, 44].

Spin Factor

The final term to take into account when computing the rate of a transition is the spin wavefunction, *i.e.* the value of the $\left\langle \psi_{\mathrm{f}}^{spin} \middle| \psi_{\mathrm{i}}^{spin} \right\rangle$. This integral can only take two values, from section 2.2 we recall that this is 0 if the spins of the initial and final state differ, and 1 if they are equal. As previously stated, transitions within singlet-manifold states or between triplet-manifold such as $S_0 \rightarrow S_n$ or $T_1 \rightarrow T_n$ are spin-allowed while transitions from triplet to singlet or vice versa, such as $T_1 \rightarrow S_0$ are spin-forbidden. But, light emission from such transition occurs experimentally observed and it is termed: *phosphorescence* to distinguish it from fluorescence.

From all the previously discussed seems hopeless for a spin–flip transition to take place – the intersystem crossing (ISC). This is because we have discarded the mechanisms involved in the interaction that make possible this type of spin forbidden transitions. It is now the turn to explore further this process fundamental to our work. But briefly stated means, that for multi-electron atoms where the spin–orbit coupling is weak, it can be presumed that the orbital angular momenta of the individual electrons add to form a resultant orbital angular momentum $\widehat{\mathbf{L}}$. Likewise, the individual spin angular momenta are presumed to couple to produce a resultant spin angular momentum $\widehat{\mathbf{S}}$. Then $\widehat{\mathbf{L}}$ and $\widehat{\mathbf{S}}$ combine to form the total angular momentum $\widehat{\mathbf{J}}$. This kind of combination is visualised in terms of a vector model of angular momentum. This kind of coupling is called $\widehat{\mathbf{L}}$–$\widehat{\mathbf{S}}$ coupling or Russell-Saunders coupling, and it is found to give good agreement with the observed spectral details for many light atoms. For heavier atoms, another coupling scheme called "j-j coupling" provides better agreement with experiment [36].

2.6 Intersystem Crossing.

In order to make the experimental observation phosphorescence consistent with theory, we need to invoke a mechanism that allows the spin forbidden transitions to take place. Such mechanism is provided by the *spin–orbit coupling*, that states that when the spin angular momentum $\widehat{\mathbf{S}}$ and the orbital angular momentum $\widehat{\mathbf{L}}$ couple only the total angular momentum $\widehat{\mathbf{J}} = \widehat{\mathbf{L}} + \widehat{\mathbf{S}}$ needs to be conserved during the transition. *This is of such instrumental importance* that we are going to rephrase it, the *total*

spin–angular momentum $\widehat{\mathbf{J}}$ is the quantity that needs to be conserved in the analogy of conserved dynamical variables, hence the offset balance between $\widehat{\mathbf{S}}$ and $\widehat{\mathbf{L}}$ *is* ***the physical mechanism*** that allows forbidden transitions like *spin–conversion* to take place, or more generally any change in *spin–multiplicity* the driving force in intersystem crossing ISC.

When spin flip is involved (*e.g.*, $S_1 \rightarrow T_1$, $T_1 \rightarrow S_0$). The system is taken from one type of spin multiplicity to another and this can be done from one way to the other, that is to say, in the reverse direction. It is common for ISC to occur from either the zero-point vibrational level of S_1 or from higher energy vibrational levels of S_1 (usually thermally populated). ISC can proceed into any excited vibrational level of the first excited triplet state (T_1) or to higher energy excited triplet states T_2, T_3 and so on, but only to those which are closest in energy to S_1. When intersystem crossing occurs in the reverse direction, is called reverse intersystem, crossing (rISC). It follows from the first excited triplet state T_1 to S_1, and is of instrumental importance when the energy difference between the two states is small, which allow thermal activation of T_1 to a given vibrational level of S_1 when they are isoenergetic. This is commercially exploited in organic light-emitting diodes (OLEDs) in order to harvest those non-emissive triplets and repopulate the emissive singlet state in what is known as *thermally activated delayed fluorescence* (TADF).

The starting point of all these allowed and forbidden transitions stem on our extensive use of the working horse of the Born-Oppenheimer approximation (BOA), so far this convenient treatment has treated the electron spin motion independently from both the motion of electrons in orbitals and the motion of nuclei present in vibrations and rotations. We shall see that this procedure is not entirely correct, is justified on the fact that spin motion is exclusively due to a magnetic interaction and that the interaction of the electric and magnetic fields is relatively weak. This justification is further supported by observing that the Born-Oppenheimer approximation excels for the ground–state of organic molecules that do not massively interact with other excited electronic, vibronic and spin states. However, the BOA breaks down in certain specific instances, which give rise to the origin of the spin forbidden transitions. One of such instances is when one single nuclear configuration leads to two or more electronic states of similar energy (commonly refer as *degeneracy*), this, in turn, renders the states in resonance condition. When resonance conditions are fulfilled, those two or more

resonant states start competing for the dynamical control of the nuclear motion [45]. In other words, this approximation breaks down when either interaction becomes strong, be it between electrons and vibrations interacting -*vibronic coupling*- or by the interaction of the spin and orbital motion of the electron -*spin-orbit coupling*. Both interactions can happen jointly.

2.6.1 $\lambda_{S_1}^{T_n}$ '*The*' parameter of ISC

The evaluation of the mixing between S_1 and T_n: $\lambda_{S_1}^{T_n}$, dictates how likely a transition between them occurs, a direct analogy on what we have already stated in the *Fermi's golden rule* for electronic transitions. In particular note that when the energies E_{S_1} and E_{T_n} become close, regardless of the value of the numerator the quotient can get very high, on the other hand, for any arbitrary non-vanishing value of the denominator the value of the parameter will heavily rely on the evaluation of the matrix elements, which will be squared, as such, terms smaller than 1 are to become even smaller when squared.

$$\lambda_{S_1}^{T_n} = \frac{\left\langle \Psi_{S_1} \middle| \widehat{H}_{\text{SOC}} \middle| \Psi_{T_n} \right\rangle^2}{E_{S_1} - E_{T_n}} . \tag{2.25}$$

Then we evaluate both the mixing between S_1 and T_1, $\lambda_{S_1}^{T_1}$, as well as the sum of the mixing to all states lower in energy than S_1 at a given geometry, $\lambda_{S_1}^{T_n<S_1}$. Succinctly, there are only two ways to overcome this issue, both of them requires a higher degree on the mathematical sophistication of the problem, which for the scope of this work we will pursuit no longer, but this mixing parameter will be revisited on chapter 4, where extensive literature has been provided.

3 Experimental Methods.

When faced with novel materials and in their development, scientists employ a variety of characterisation techniques, they all depend on the material's function, composition and dimensions. But almost always many of these techniques rely on light as a probing media. Unsurprisingly, we use spectroscopic techniques for studying organic semiconductor materials. For example, 'PUMP-PROBE' spectroscopy in its various implementations is often used to monitor fundamental processes like optical gain, exciton dissociation and charge transport to name a few [46–48] in particular those where ultrafast optical processes take place following photoexcitation, a timescale typically in the order of hundreds of femtoseconds to picoseconds ($10^{-14} - 10^{-12}\,s$). PUMP-PROBE is routinely employed for mapping primary photochemical dynamics and transient intermediates in functional chromophores, a class of research vital for developing more efficient light-harvesting materials [49].

The overwhelming widespread use of spectroscopy is understood when we rationalise all the properties that can be extracted from such experiments. Simple properties such as absorbance, fluorescence, as well as linear and circular dichroism provide detailed information on molecules; like concentrations, energies, conformations, or dynamics and often their sensitivity to small changes in molecular structure or their surroundings. Most of our knowledge about the structure of atoms and molecules is based on spectroscopic investigations. Single-handedly spectroscopy has made an outstanding contribution to the present state of atomic and molecular physics, which naturally encompasses chemistry and molecular biology. In this chapter, we devote some time to describe the basics of this beautiful scientific discipline. Pump-probe spectroscopy has been particularly useful in studies of light-driven processes in photosynthesis, vision, bacteriorhodopsin, photoactive yellow protein, green fluorescent protein, and DNA photolyase [44].

3.1 Introduction.

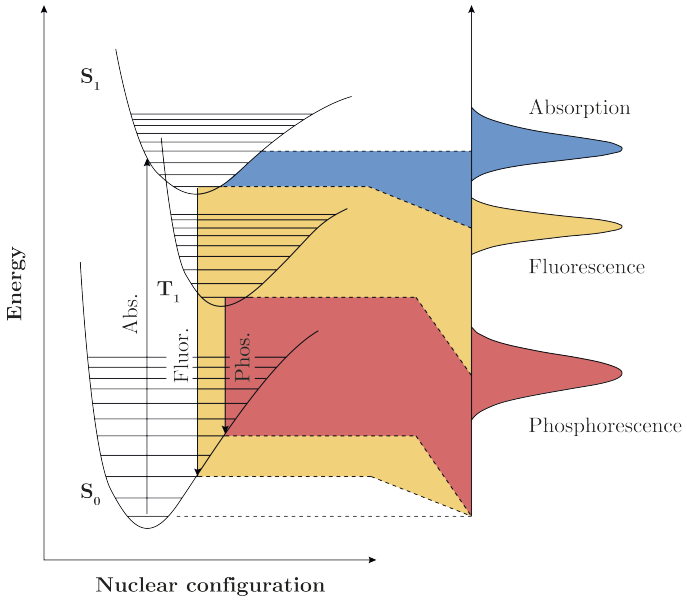

Figure 3.1. Absorption, Fluorescence and Phosphorescence schematics with Jablonski-Diagram.

Radiative processes have the suffix term -*luminescence*, preceded by the origin of such luminous stimuli. So, when the energy source comes from light we called it *photoluminescence* (PL), when it originates from an electric field it is named *electroluminescence* (EL) which is the operational mechanism for virtually all LEDs. Emission of light can be observed as a result of a chemical reaction[1], hence the term -*chemiluminescence* (CL) - and lastly when these chemical reactions take place inside a living organism we name defined it as *bioluminescence* (BL). Finally, we subdivide further photoluminescence into two types of luminescence: *fluorescence* and *phosphorescence* according to the type of excited to ground state transition; either from singlet or triplet state respectively See figure 3.1 above. On the previous chapter, we stated that molecules exist in well-defined quantum-states and how they change from one state to another, and particularly induced by light. A molecule excited by light can decay back to the ground state by several possible pathways. One possibility is to reemit energy as fluorescence. In spectroscopy, we are interested in knowing which of these decay channels dominate and why.

[1]Note, that the energy source, in this case, is on chemical surprisingly rather thermodynamically in origin.

All spectroscopy experiments consist of three basic items: a source of light, a sample holder and a detector see figure 3.3. Steady-state measurements give the integrated signal over a given time range and are useful for determining the average response of the material with respect to temperature, or morphology, for example. On the other hand, time-resolved experiments give more information on the systems since they revealed their behaviour as a function of time. Because of their extraordinary sensitivity and speed, optical spectroscopic techniques are well suited for addressing a broad range of questions in molecular physics. Photomultipliers sensitive enough to detect a single photon make it possible to measure the fluorescence from individual molecules, and lasers providing light pulses with widths of less than $10^{-14}\,s$ can be used to probe molecular behaviour on the time scale of nuclear motions.

A fluorophore is a molecule or part of it, that absorbs light of a specific wavelength and then remits at a different but specific wavelength. The amount and wavelength of emission depend on both the fluorophore and its environment. Fluorophores were called chromophores, for a historical association of these molecules to their colour. Their distinction from chromophore implies the molecule not only absorbs light but emits it too. Compounds absorbing in the visible region of the spectrum (posses colour) some have weakly bound or delocalised electrons. In these systems, the energy difference between the lowest LUMO and the HOMO corresponds to the energies of quanta in the visible region. Hence, most of the known stable and bright fluorophores absorb and emit in the wavelength range between 300 and 700 nm.

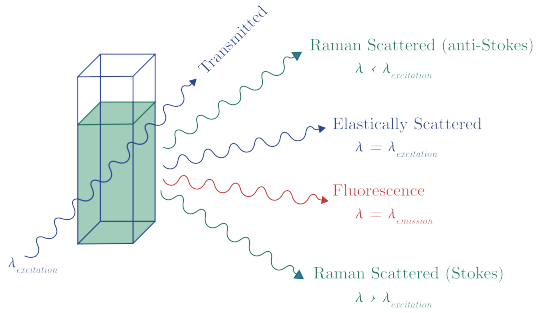

Figure 3.2. Common outputs of light-matter interaction processes.

3.2 Sample Preparation.

The specifics of sample preparation varied from material to material, all molecules were used as purchased or as received. Unless otherwise noted, solutions were prepared under normal 'air' conditions using common organic solvents with frequent exposure to oxygen. Solutions were generally stored in glass vials and used within a week of preparation, depending on experiment and lab availability. Most of the spectroscopic measurements, were solutions sealed in 1 or 10 mm path-length quartz cuvettes (Hellma Analytics) with a Polytetrafluoroethylene PTFE stopper and parafilm when needed.

3.3 Steady State Spectroscopy.

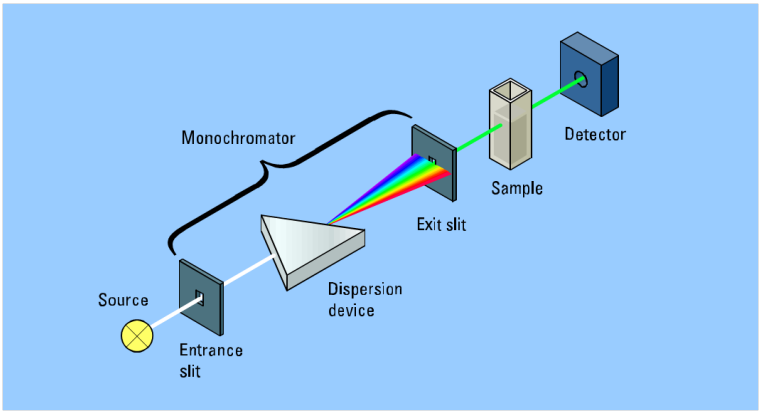

Figure 3.3. Typical UV-Vis experiment arrangement. Note that in the case for emission detection one needs to place the detector orthogonally to the incident beam.

3.3.1 UV-Vis Absorption.

Most spectroscopic investigations must begin with an understanding of the steady-state absorption of a material. Ultra violet-Visible absorption (UV-Vis) spectroscopy is a standard technique, found in most physical-chemistry laboratories. It is used to determine the electronic transitions that occur in a molecule when it is excited by light. As the name suggests, the technique probes transitions in the ultraviolet and visible region of the electromagnetic spectrum, particularly well-suited to studying conjugated organic molecules where the lowest energy transitions are in this region. The electronic absorption is often modulated

with the transitions to different vibrational sublevels of the excited state, known as the Franck-Condon progression. The energy spacing between the vibrational bands is equal to the excited state vibrational frequency, which for organic conjugated molecules is typically the C=C stretching frequency (1600 cm^{-1}).

3.3.2 Photoluminescence.

Photoluminescence spectroscopy is a powerful technique to study emissive excited states -if an excited state can couple radiatively to the ground state. Following the absorption of photons, excited electrons can return to the ground state by re-emitting a photon with energy equal to the gap between them. This technique enables us to probe the nature of these emissive transitions. The various techniques available generally have high sensitivity and can detect photons even in cases where <1% of the excited population is emissive, thus making it a valuable technique for investigating the photophysics of a system. Emission in organic systems generally occurs from the lowest vibrational level of the excited state (named as Kasha's rule). From this level radiative transitions occur to vibrational levels of the ground state, resulting in a 'mirror-image' appearance of the absorption spectrum.

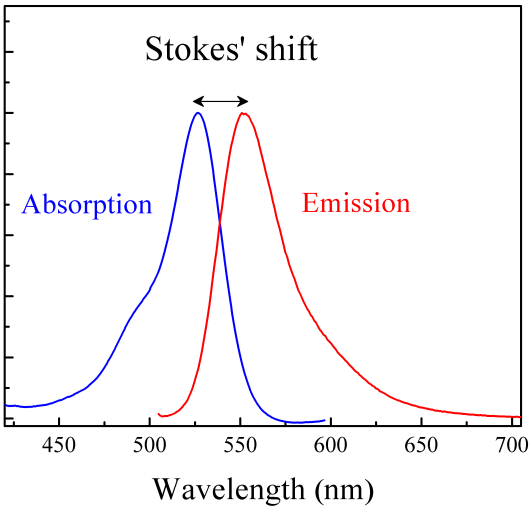

Figure 3.4. Typical mirror image or 'Stokes-Shift' associated to absorption and emission from rhodamine 6G. Image by Sobarwiki, public domain.

3.3.3 Phosphorescence.

In the production of excited states by the promotion of an electron into a higher orbital, the direction of the spin of the electron is preserved. Since most molecules have an even number of electrons and these are normally arranged in pairs of opposite spin, promotion of an electron does not disturb this parity. However, it is possible for the spin of the promoted electron to be reversed so that it is no longer paired and the molecule has two independent electrons of the same spin in different orbitals. Quantum theory predicts that such a molecule can exist in three forms of very slightly differing, but normally indistinguishable energy, and the molecule is said to exist in a triplet state. The indirect process of relaxation from an excited state produced by singlet state to a triplet state is known as intersystem crossing, and can occur in many materials when the lowest vibrational level of the excited singlet state, S_1, has around the same energy level as an upper vibrational level of the triplet state. Direct transition from the ground state, usually a singlet state, for a molecule with an even number of electrons, to an excited triplet state is theoretically forbidden, which means that the reverse transition from triplet to ground state will be difficult. Thus, while the transition from an excited singlet state, for example, S_1, to the ground state with the emission of fluorescence can take place easily and within $10^{-9} - 10^{-6}$ seconds, the transition from an excited triplet state to the ground state with the emission of phosphorescence requires at least 10^{-4} seconds and may take as long as 10^{2} seconds. This delay was once used as the characterisation of phosphorescence, but a more precise definition requires that phosphorescence be derived from transitions directly from the triplet state to the ground state. The triplet state of a molecule has lower energy than its associated singlet state so that transitions back to the ground state are accompanied by the emission of light of lower energy than from the singlet state.

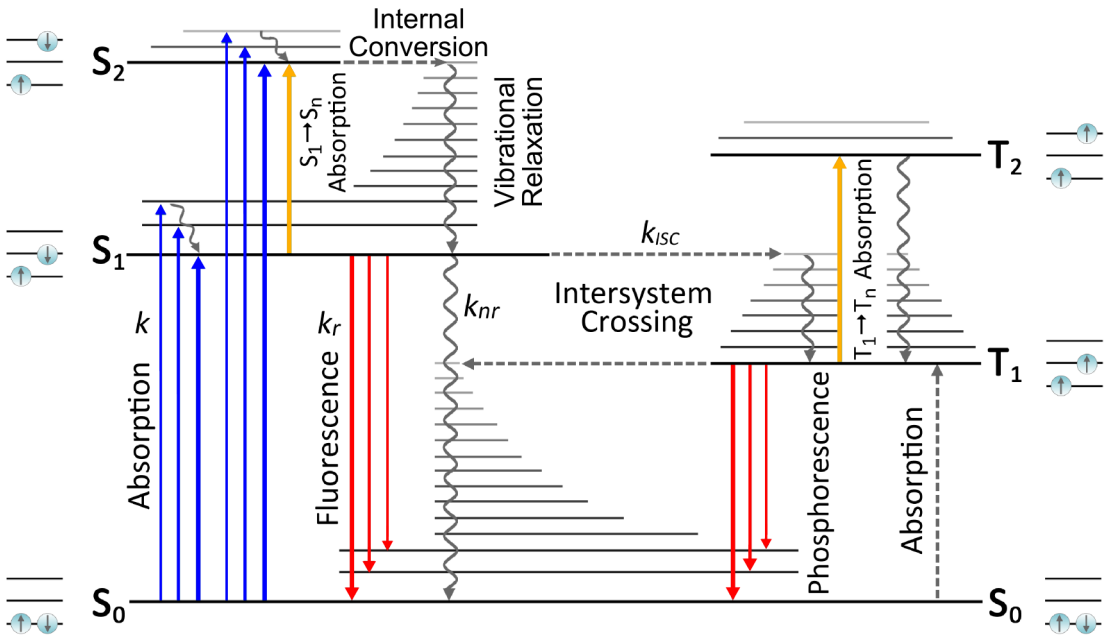

Figure 3.5. Expanded Jablonski-Diagram. The figure depicts types and usual time-scales of transitions. Figure credit to Dr Andrew Joseph Musser, used with permission.

Therefore, we would typically expect phosphorescence to occur at longer wavelengths than fluorescence. Since molecules occupying excited states for relatively long periods can easily lose their energy by other deactivating channels instead of phosphorescence. Hence, triplet states are very susceptible to collisions with solvent molecules. Solute molecules with unpaired electrons, such as oxygen, are very effective at destroying triplet states even at low concentrations. Therefore, phosphorescence in solution at room temperature is a rare phenomenon, but by dispersing the sample in a rigid matrix or freezing the solution to a low temperature, it can be observed from many compounds.

Figure 3.6. Visible phosphorescence of C8-BTBT at 77K inside a cryostat for spectrsocopical measurements.

3.4 Time-Resolved Spectroscopy.

3.4.1 Time-Resolved Photoluminescence.

The photoluminescence lifetime as already mention is an intrinsic characteristic of a fluorophore that can provide insight into the species excited state dynamics. When used jointly with a time-dependent detection system, *time-resolved photoluminescence* (TR-PL) may reveal spectral changes that are averaged out in the steady-state (such as vibrational relaxation). Hence, TR-PL is the tool of choice for studying fast electronic deactivation processes, (*e.g.*; solvent dependence, presence of quenchers (O_2), or temperature) as well as interactions with other molecules. Processes like Förster Resonance Energy Transfer (FRET), quenching, solvation dynamics, or molecular rotation also have an effect on the decay kinetics. Lifetime changes can, therefore, provide information about the local chemical environment or insights into reaction mechanisms.
It is also possible to measure time-resolved photoluminescence, which yields information about the lifetime of the emissive states. In this dissertation, the only technique used for this purpose is time-correlated single-photon counting (TCSPC). TCSPC works by measuring the time between sample excitation by a laser pulse and the arrival of the emitted photon at the detector. In other words, TCSPC is basically a timer, that starts when a laser pulse is fired and stopped when a photon emitted from the sample

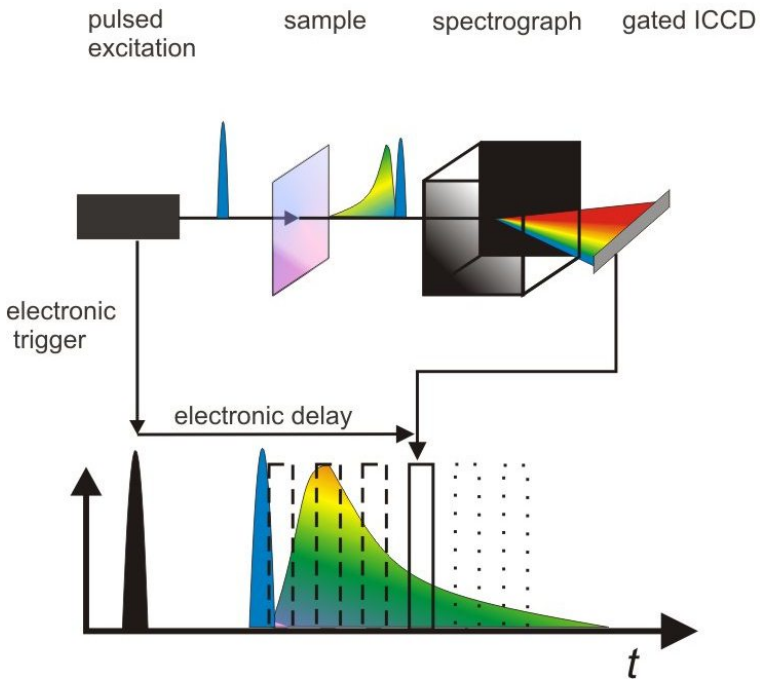

Figure 3.7. Schematics of a Time-Resolved Photoluminescence Experiment.

reaches the detector. Time-correlated single-photon counting requires a defined "start", provided by the electronics steering of the laser pulse, and a defined "stop" signal, realised by detection with single-photon sensitive detectors. The measurement of this time delay is repeated many times and after sufficient collection, time to account for the statistical nature of the fluorophores emission. The resulting histogram according to their arrival, reflects the decay lifetime of the emitting state. Which allows reconstruction of the photoluminescence decay.

The time-correlated single-photon counting uses the same excitation as for steady-state PL, but the sample emission instead collected and directed through a monochromator to select the desired photoemission energy and onto a photomultiplier detector. The emission is passed through a colour filter to remove any residual scattered light from the pump beam, as well as through a neutral density filter to obtain a good signal to noise ratio.

3.4.2 Transient Absorption.

Transient absorption is an extremely powerful and versatile technique. Its main purpose is to track the electronic states, for both ground and excited states, as a function of time. In this thesis, we use it as the primary tool to measure C8-BTBT and derivatives photodynamics, and

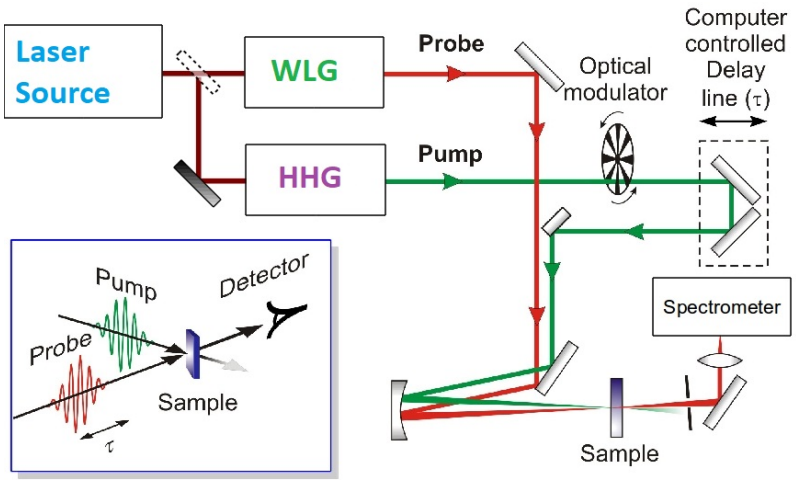

Figure 3.8. Schematics of a Pump and Probe optical set-up.

to see how the substitutions may influence the intersystem crossing mechanism of the core complex.

The pump-probe technique provides insight into photoinduced phenomena with temporal resolution in the femtoseconds domain. This technique is capable to address both radiative and non-radiative processes, often called 'dark'. In this technique, the sample is excited with a laser pulse - the *pump* - at time zero, then a *probe* pulse[2] is focused on the same location, with a controllable time interval (the 'delay'). Providing a time-dependent description of the pump induced changes through a wide range of delays. The time resolution is only limited by pulse duration. In this fashion, we can build a map of the probe transmission and how it changes from initial photoexcitation up to decay back to the ground state and relate all of this to the photophysical processes occurring in the material. This technique is capable to address both radiative and non-radiative processes[3]. Which is an advantage on PL-based techniques, it is sensitive to all states which are populated following photoexcitation, the drawback is the low sensitivity of the experiment; certainly lower than PL. It is for this reason we employ different techniques.

Electrons in the excited state have a different set of transitions available from electrons in the ground state, therefore the absorption of the system is modified from the ground state absorption. Our interest amounts to the pump–induced change in transmitted probe following excitation. The measured signal is the difference between the intensities of the transmitted probe pulses in the presence and absence of the excitation pulses

[2]That can be monochromatic or broadband.

[3]or commonly refer as 'dark', for they are not radiatively coupled to the ground state

and usually is averaged over many pulses. This differential transmission ΔT is normalised to yield $\frac{\Delta T}{T}$, and it enables comparison between different interactions of the excited states with light. Experimentally, the Transient Absorption signal is the ΔT of the probe with and without the pump present, thereby measuring only the excited state absorption. The pump pulse is '*chopped*' at half the frequency of the probe, meaning every second measurement recorded is done without the pump pulse.
To interpret the signal at a first approximation we disregard coherent artefacts and just focus on three general types of spectral feature that can be observed in a TA measurement. The peaks in the resulting TA spectra can be classified into three types of signals based on the nature of the transitions that produce them: *ground state bleach* (GSB), *stimulated emission* (SE) and emphphotoinduced absorption (PIA). First we will address positive TA signals. Any signal with $\Delta T/T > 0$ relates to an increase in transmittance in a certain spectral region when the system is excited. Such situation occurs when a fraction of the electrons previously in the ground state are excited and leave the ground state, when this fraction increases in such a fashion that the majority of the population of electrons are in effect in a higher state, we are in a *population inversion* regime.

Ground State Bleach

Conventional absorption measurement gives information about the transitions accessible from the ground state. In transient absorption, the additional pump pulse before the measurement means that a certain fraction of the chromophores is already excited. This is known as the ground-state depletion, named photobleaching (PB). PB corresponds to positive ΔT and has the spectral shape of ground-state absorption when thermalisation, is over (which is usually very fast). One should keep in mind, however, that internal conversion normally is very fast ($\sim$ 100 fs), so in most cases, we probe the thermalised sample with the occupation of the lowest states only.

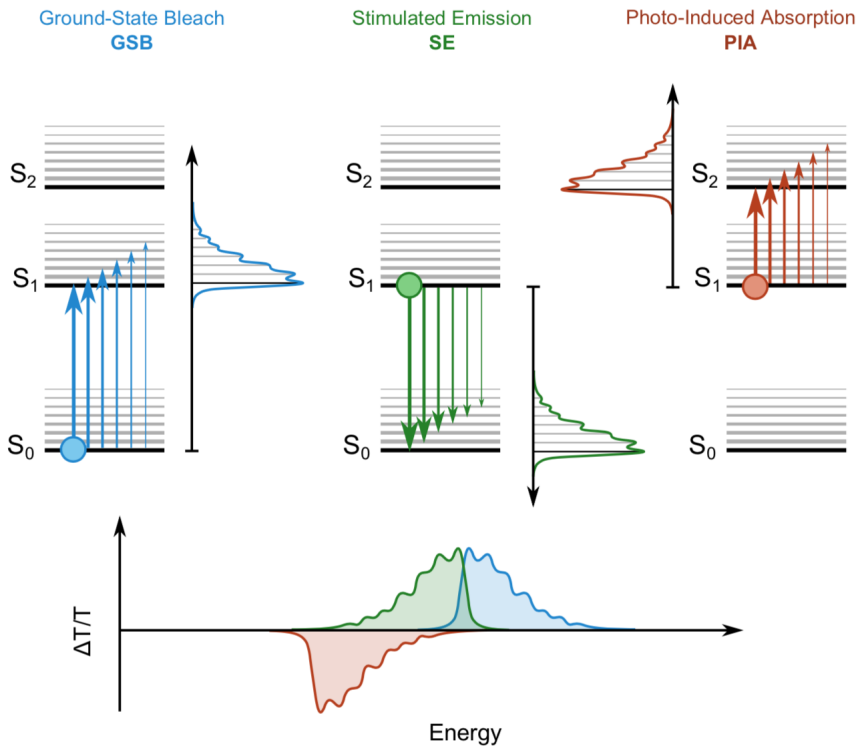

Figure 3.9. Typical $\Delta T/T$ signals. Figure by Dr. Andrew Joseph Musser, used with permission.

Stimulated Emission.

When there exists an allowed transition from (S_1) to S_0, we say the system luminesce, so again the ΔT is positive which means stimulated emission (SE) is taking place. Although this does not always mean a positive ΔT is observed in the region of emission, as it depends on the spectral overlap with other absorbing transitions (often there) and on the relative cross-sections involved. As a result, SE may not appear at all even in light-emitting materials.

Photo-induced Absorption.

Photoinduced absorption (PIA) is a broad term that encompasses any change in the sample following excitation that results in increased absorption of the probe. This is seen in TA spectra as a reduction in probe transmission, this is a negative $\frac{\Delta T}{T}$ feature. The most common origin of PIA is the absorption of excited states. Each state - singlets and triplet - has its characteristic absorption features, so given a sufficiently broad probe spectral range the PIA can offer the best 'fingerprint' of the excited species present, though the differences between PIA bands can at times be subtle. It is thus the most useful feature for building a model of the photophysics of organic materials and the progression of excited

states following pump absorption. However, even in this case, other phenomena such as the artefacts that we mention at the beginning of the chapter can result in similar photoinduced absorptions, so rigorous care must be taken in making spectral assignments.

4 The vibronic spin–orbit coupling in BTBT and alkyl-chains substituents.

Contents on this chapter are based on an article manuscript under review where the author of this thesis is the leading author. Nonetheless, experimental and computational modelling were made in collaboration with a theoretical chemistry group from our *campus* led by Theo Kane, and other collaborations from Glasgow University, Newcastle University and Cambridge University. Scientific leadership and project discussion were heavily shaped by Jenny Clark and Mark Geoghegan. Partial and initial femtosecond transient absorption spectroscopy was done during a *research stay* at the *Politecnico di Milano* with Tersilla Virgili, Giulio Cerullo. Fruitful discussions for sample preparation were initiated by Laura Pacini (solutions) and Humberto Gambetta (thin films) from the *l'Istituto per lo studio delle macromolecole* (ISMAC) in Milan. Finally, my group-colleague Oleksandra Korychenska from the department of chemistry for she was responsible for the *organic synthesis* of BTBT derivative molecules, as well as the *data acquisition* of the experimental Resonance Raman Spectroscoscopy, such work was done in collaboration with Sophia Hayes from Cyprus University.

4.1 Introduction

As we mentioned before, the ***spin*** –an instrumental quantum-mechanical entity– governs important material properties, intrinsically in π-conjugated organic molecular semiconductors and by extension their electronics. The spin, for example, commands the photophysics of singlet and triplet excitons in organic light-emitting diodes [50], photovoltaic [51] and polaritonic devices [52]. The same spin–based photophysical processes are also responsible for many photoprotective processes in biology [53], either affect or determine the efficiency of photodynamic

therapy [54] and for photocatalysis too [55], and they also drive the operation of spintronic devices [56, 57].

In these mainly carbon-based materials, the importance of spin in determining electronic processes originates from two material properties: Firstly, their low *dielectric–constant* allows them strong electronic correlations and correspondingly large exchange energies hence a singlet–triplet splitting too; Secondly, their generally slow *spin–dephasing* or *spin–relaxation* due to weak *hyperfine interactions* (HFIs) and spin–orbit–coupling (SOC) results in a *slow spin–lattice relaxation*, compared with most inorganic materials and slow (>ns) intersystem crossing between different *spin–manifolds* [58]. Recently, the relative importance of HFIs and SOC in determining spin–relaxation lifetimes has been studied in detail. Consensus is starting to emerge that SOC plays an important role, alongside HFIs [59–62]. However, quantifying the effect of SOC, and determining the molecular parameters that govern spin relaxation or intersystem crossing in organic molecular systems is non-trivial and research is ongoing [56, 58–60, 62–69].

In organic molecular systems, SOC depends sensitively on the complex interplay between electronic, spin and nuclear degrees of freedom. While most quantum mechanical calculations consider only direct spin-orbit coupling, it is becoming clear, that often is necessary to include vibronic terms in the SOC Hamiltonian [63, 64]. For these vibronic terms are thought to act by allowing vibrations to induce mixing between orthogonal orbitals (e.g. π and σ orbitals) that increase SOC. This mechanism is known as '***spin-vibronic-coupling***' and is described in detail in a recent review [63].

Spin–vibronic coupling has been invoked recently as a mechanism to explain unusually rapid (<<ns) intersystem crossing (ISC) in molecules where static calculations of SOC at the equilibrium geometry could not explain results [68, 70–75]. In bi-thiophene, for example, S_1 rapidly ($\sim$12 ps) converts to the triplet manifold even though the SOC matrix elements between S_1 and the triplet manifold, T_n, are negligible at the equilibrium geometry. In this case, rapid intersystem crossing has been calculated to be due to enhanced SOC during S_1 vibrational relaxation through coupling to '***out-of-plane***' vibrational modes (OOP)[74, 76–78]. Similar findings have been made in other molecules with strong coupling to torsional motion such as oligothiophenes [79–81]. In other instances,

SOC is enhanced not by reorganization during an electronic transition (i.e. through a conical intersection), but due to fluctuations in molecular geometry ('*dynamic disorder*') caused by coupling to low-energy vibrational modes [82], or possibly due to *zero–point fluctuations*.

In the above examples, the molecules are flexible and coupling to *out–of–plane* torsional motion is expected. Therefore, a reasonable assumption would be that spin–vibronic coupling might be neglected in planar molecules. However, recent work on planar molecules [82–85] suggests this assumption should be treated with caution. For example, a surprisingly rapid (∼300 ps) ISC is observed in a planar *perylenebisimide* derivative [83]. In each case, they attribute this rapid ISC to *vibronic spin–orbit* coupling.

Here, we study a series of *heteroacenes*, to determine how molecular structure impacts vibronic *spin–orbit coupling* in planar molecules used for optoelectronics applications. We chose to focus on heteroacenes because of their relevance for organic spintronics [59, 60, 86, 87] and singlet exciton fission [88–90] and their high expected triplet yield [91, 92]. In particular, we concentrate on the benzothieno-benzothiophene (BTBT) family of materials which are solution-processable materials (structures in Figure 4.1) that exhibit high charge-carrier mobility for an organic semiconductor material[93–95]. Spin properties of these materials have recently been studied in detail using electron spin resonance (ESR) spectroscopy [59] coupled with theoretical calculations [59, 86, 96] to determine the effect of spin-orbit coupling on charged molecules. In this work [59, 86], the authors define the effective SOC to mean the overlap between orbital- and spin angular momentum distributions. These depend on the molecular composition and geometry, and the spin density of the molecule. With this definition, the effective SOC is quite likely to be different for neutral and charged molecules due to the different geometry and spin densities for the two cases, and it will be interesting to make the comparison.

This earlier work demonstrated that electron-spin resonance (ESR) measurements of charged molecules in solution yield *gyromagnetic coupling tensor* shifts (Δg) that are correlated with spin-lattice relaxation times (T_1) [59]. Through comparison with theory they find that the Δg shifts are dominated by spin-orbit coupling [86]. Some of the findings are initially counter-intuitive [86]. They find, for example, that double

addition of alkyl chains on the long-axis of the BTBT molecule, *ie* in C8-BTBT-C8[1], reduces the effective spin-orbit coupling by a factor of ∼2 due to '*spin-leakage*' into the alkyl chains and away from the sulphur.

Here we explore steady–state and time–resolved spectroscopy of similar alkylated benzothieno-benzothiophene-based materials in solution, which we report for the first time. Despite their planarity, we find that ISC in BTBT derivatives is rapid (∼150 ps) generating a high yield (∼50-98%) of triplet excitons. In contrast to the findings by Schott *et. al.*, we prove that ISC is faster in the alkylated molecules compared with the bare derivative, suggesting larger effective SOC in alkylated molecules. Using DFT calculations we find that such fast intersystem-crossing cannot be explained via direct SOC or solely due to the thiophene units, and requires vibronic contributions. To explore this, we use molecular dynamics simulations to probe the ensemble behaviour of our system at different temperatures.

Our findings suggest that spin-orbit coupling depends sensitively on vibronic coupling, even in the highly planar materials required for optoelectronic, photonic and spintronic devices. Further, these findings suggest that studying spin-behaviour and spin-orbit coupling in solution may not be directly relevant to the solid-state because the low-energy tuning modes that impact spin-orbit coupling can be altered –or completely damped– when moving to the solid-state [94].

[1]Throughout this chapter we have adopted a long format name to denote 2,7-Dioctyl[1]benzothieno[3,2-b][1]benzothiophene, namely C8-BTBT-C8 instead of the shorter form C8-BTBT used in the rest of the Thesis, in order to avoid confusion with another substituent.

4.2 Results

4.2.1 Nature of the excited-states and spectral analysis of fluorescence and phosphorescence in BTBT derivatives.

Although some detailed photophysical study here and there of BTBT derivatives exist [91, 92], no study has yet rigorously explored the impact of side-chain substitution. We, therefore, started with a detailed description of the absorption and photoluminescence spectra, shown in Figure 4.1. The figure shows the absorption, fluorescence and phosphorescence spectra of our target molecules. In panels (a) to (c) differences due to alkyl-chain substitution to the core BTBT, in (d) together with a benzothieno-benzothiophene molecule which is non-planar in the ground-state panel (d). Panel (e) shows DFT calculations for the singlet (bars) and triplet (circles) energies and oscillator strengths.

From the absorption spectra in panels (a)– (c), we assign the peak at 3.75 eV (331 nm) to the S_1 electronic (0-0) transition. Increasing the number of alkyl chains slightly shifts this peak to lower energies (by 0.01 eV) due to a shift in the HOMO energy. In di-BT, the S_1 energy is stabilized to 3.45 eV (360 nm). Interestingly, DFT calculations show that S_1 and S_2 have very similar oscillator strengths in the three BTBT derivatives and are separated by only ∼0.19 eV (C8-BTBT-C8). This spacing is very similar to the dominant vibrational modes measured with resonance Raman: ring stretches at 1474 cm^{-1} (0.18 eV), 1555 cm^{-1} (0.19 eV) and 1604 cm^{-1} (0.2 eV), shown in Figure 4.2. This close energetic separation explains the congested vibronic structure of the absorption spectra, which cannot be modelled as a standard Franck-Condon progression. It suggests non-adiabatic coupling between states is likely, but we do not calculate the spectral contribution from this. On the other-hand, in di-BT S_1 is separated from S_2 (S_3) by 0.4 eV (0.6 eV) and S_1 has significantly higher oscillator strength than both S_2 or S_3. This conclusion is supported by the fact that the di-BT absorption spectrum can be reasonably well fitted with a standard Franck-Condon model and shows near mirror-symmetry between absorption and fluorescence (see analysis below, Figure 4.4).

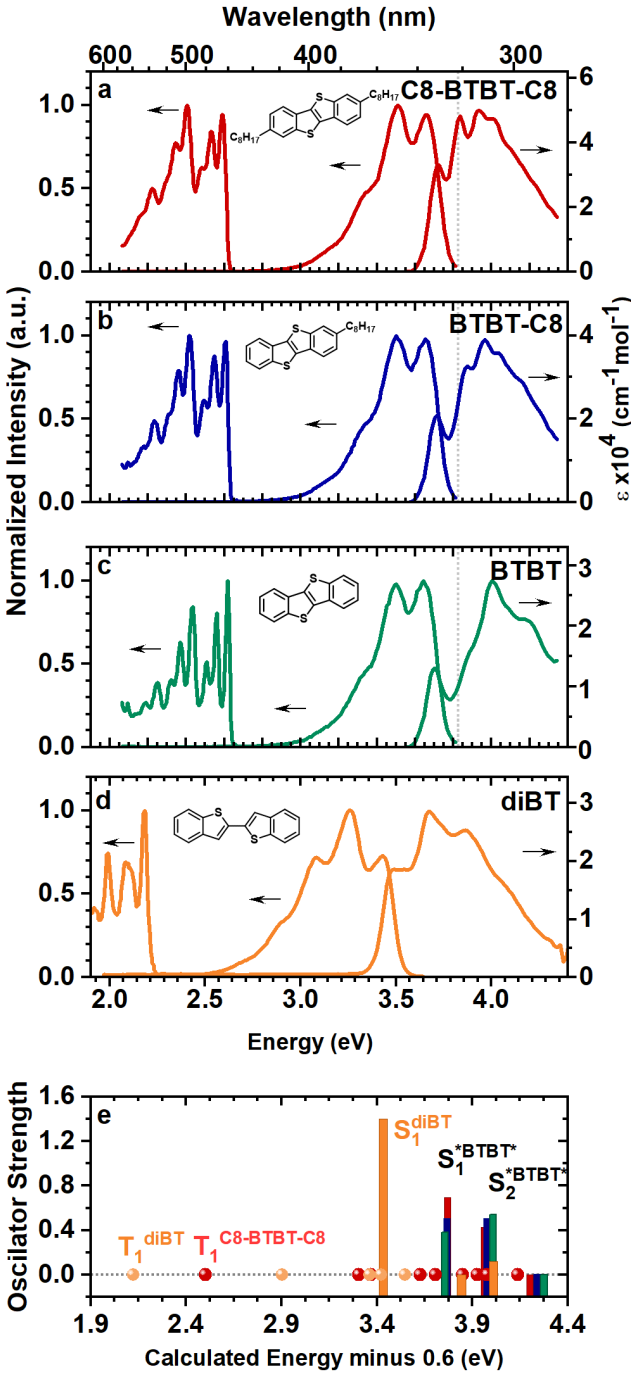

Figure 4.1. Steady-state spectroscopy of benzothieno-benzothiophene derivatives. Parts (a)-(c) show (from top to bottom and left to right) experimental phosphorescence (77 K), fluorescence (Room Temperature) and absorption (RT) spectra of (a) C8-BTBT-C8, (b) BTBT-C8, (c) BTBT and (d) di-BT in dilute solution. Chemical structures are shown in insets. RT measurements were performed in toluene, 77 K measurements in a toluene:ethanol:diethyl ether (1:1:2) solvent mixture. (e) shows DFT-calculated energies and oscillator strengths of the low-lying singlet (bars) and triplet (circles) excited states. Bar height denotes oscillator strength. DFT and *molecular dynamics* simulations are known for overestimate energy in MO processes, thus the shift of 0.6 eV in the x-axis to match experimental values.

The extinction coefficient of the S_1 absorption was measured to be 12,400 $cm^{-1}mol^{-1}$ for BTBT and increases to 33,100 $cm^{-1}mol^{-1}$ for C8-BTBT-C8 and 28,500 $cm^{-1}mol^{-1}$ for di-BT. This increase in oscillator strength of S_1, reproduced in the DFT calculations in panel (d), suggests that the S_1 state delocalises into the alkyl chains in BTBT-C8 and C8-BTBT-C8 or along the entire di-BT chain. This is reminiscent of the spin-density calculations reported in Ref. [59]. For comparison, the width of the vibronic replica in the absorption spectrum (assuming Gaussian broadening) increases from 34 meV for C8-BTBT-C8 to 59 meV for di-BT (see fits in Figure 4.4). The increased broadening in di-BT reflects the fact that the electronic transition couples to low-energy *out-of-plane* torsional motion which broadens the spectra and induces a sizeable Stokes' shift of ∼100 meV (∼65 meV in C8-BTBT-C8). The emission spectra are similar in all three BTBT derivatives see figure 4.1 (a)–(c). The small Stokes shift and clear vibronic structure strongly suggests emission comes from S_1 only, in agreement with the Kasha-Vavilov rule. We found no solvent dependence of the absorption or emission spectra, nor viscosity-dependence, nor difference in emission spectral shape when exciting into S_2.

The phosphorescence spectra (left part of each panel in Figure 4.1) were measured at 77 K. They show vibronically structured spectra, giving a triplet energy of 2.6 eV (475 nm) and a T_1-S_1 energy gap of 1.2 eV for the BTBT derivatives (energetic values are taken at the onset of the 0-0 peaks). Using these values, we can benchmark our DFT calculations of the triplet energies panel (d). Our calculations show that the T_1-S_1 energy gap (1.2 eV) is similar to the experimental value. We, therefore, predict the relative energies of other triplet states should be correct too.

4.2.2 Resonance Raman Spectroscopy

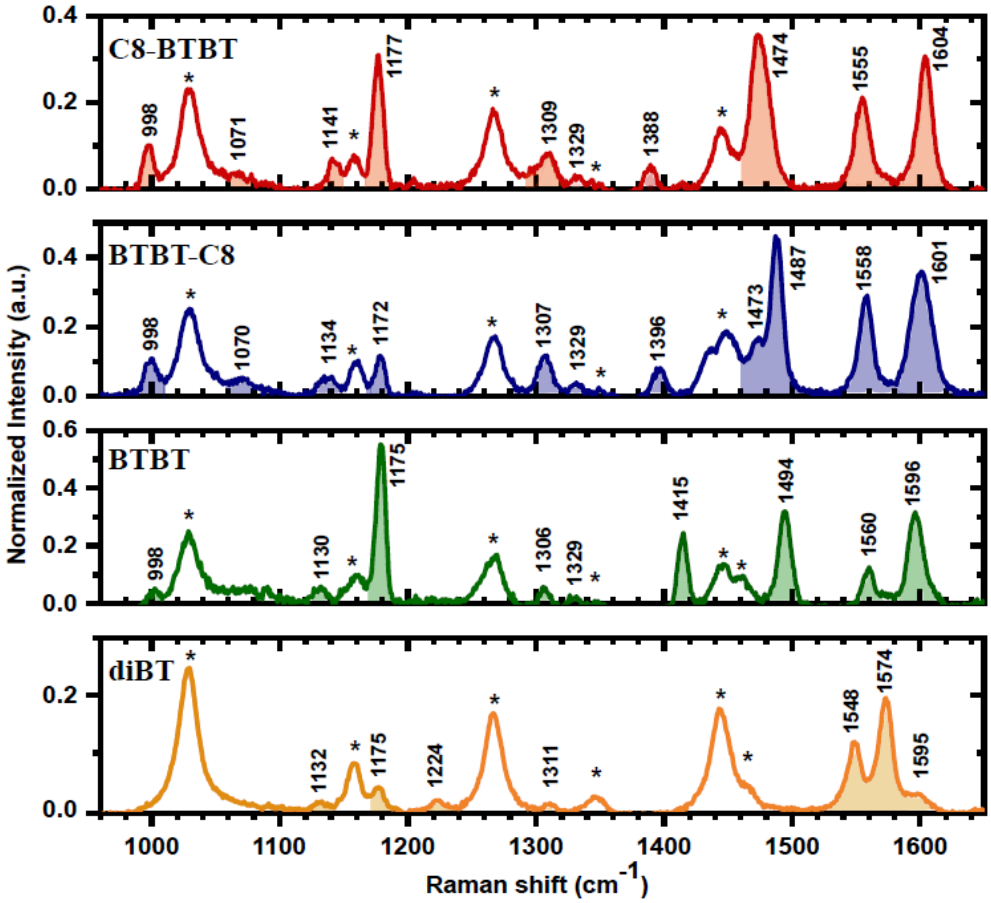

Figure 4.2. Resonance Raman spectroscopy of BTBT derivatives. Excitation at 282 nm (4.40 eV) in cyclohexane to remain on-resonance range. (a) C8-BTBT-C8, (b) BTBT-C8, (c) BTBT, (d) di-BT. Solvent modes are marked with an asterix on top of its associated peaks, target molecule's modes are shaded. Assignment of modes is performed by comparing with DFT calculations and cross-section analysis is shown in Table 4.1.

To analyze the emission spectra in more depth, we first present resonant Raman spectra in Figure 4.2 which should relate to the fluorescence vibronic structure. The Raman measurements were performed in cyclohexane with excitation at 282 nm. This wavelength was chosen so that we remain on-resonance with the lowest electronic transitions while reducing unwanted background fluorescence. From these spectra, we have calculated the Raman cross-section of the main vibrational modes, following the method described by Myers [97]. These are shown in Table 4.1. Assignment of the different modes is accomplished by comparing the spectra to DFT-calculated modes. All modes are found to be in-plane

vibrations, including dominant contributions from ring-breathing and C–H-coupled backbone motion.

C8-BTBT-C8		BTBT		di-BT	
ν (cm^{-1})	σ^{Raman} ($10^7 cm^2$)	ν (cm^{-1})	σ^{Raman} ($10^7 cm^2$)	ν (cm^{-1})	σ^{Raman} ($10^7 cm^2$)
1604	4.16	1596	7.37	1595	1.02
1555	2.9	1560	2.52	1574	4.24
		1494	5.94	1548	3.01
1474	6.29	1415	3.14		
1388	0.45				
1329	0.68	1224	0.41		
1309	0.91	1306	0.53	1311	0.13
1177	2.51	1175	6.35	1175	0.73
1141	0.53	1130	0.80	1132	0.43
1071	3.7				
998	0.74	998	-		

Table 4.1. Resonance Raman cross-sections σ^{Raman}, calculated using the method outlined in Ref. [97]. ν is the Raman shift in wavenumbers. Using $E_{vib}^{\text{effective}} = \sum_i E_i^{vib}\sigma_i^{Raman} / \sum_i \sigma_i^{Raman}$, we determine effective high (ν >1200 cm^{-1}) and mid-range (ν <1200 cm^{-1}) vibrational energies that couple to the electronic S_0-S_1 transition. This gives, for example, E_{vib}^{high} ≈1520 cm^{-1} and E_{vib}^{med} ≈1110 cm^{-1} for C8-BTBT-C8.

The calculated resonance Raman cross-sections (σ^{Raman}) should, to first approximation [97], be proportional to the square of the displacement along normal co-ordinates Q between the ground-state and the excited-state potential energy surfaces. This displacement is quantified by S, the Huang-Rhys parameter, directly proportional to $(\Delta Q)^2$. Hence the resonance Raman spectrum indicates which normal modes couple most strongly to the resonant electronic transition, and the relative cross-section denotes the strength of the coupling to that particular vibrational mode. We, therefore, use our resonant Raman analysis to describe the fluorescence spectrum. To achieve this, we split the Raman modes into high (ν >1200 cm^{-1}) and mid-range (ν <1200 cm^{-1}) regions and calculate two weighted effective vibrational energies using $E_{vib}^{\text{effective}} = \sum_i E_i^{vib}\sigma_i^{Raman} / \sum_i \sigma_i^{Raman}$, where the sum runs over the different modes in the spectrum (see Table 4.1).

4.2.3 Franck-Condon Analysis of the fluorescence spectra

At the excitation energy we use for the resonance Raman 282 nm (4.4 eV), it is difficult to disentangle the contributions from S_1 and S_2. Nevertheless, we use the effective modes calculated from Table 4.1, to fit the 77 K fluorescence spectra with a multi-mode Franck-Condon model given by:

$$P(\hbar\omega) \propto n_f^3(\hbar\omega)^3 \sum_{m_i} \prod_i \frac{S_i^{m_i} e^{-S_i}}{m_i!} \times \Gamma\delta \left[\hbar\omega - \left(\hbar\omega_0 - \sum_i m_i \hbar\omega_i\right)\right], \qquad (4.1)$$

Where n_f is the refractive index and the product of cube terms accounts for the photon density of states. We assume that the refractive index in solution is non-dispersive in the spectral region of interest; the index i runs over the different effective vibrational modes and m_i are the vibrational quanta ($m_i = 0, 1, 2\ldots$); S_i is an effective Huang-Rhys parameter for mode i; Γ is a Gaussian lineshape function with broadening σ and $\hbar\omega_0$ is the bare electronic energy ('zero-phonon energy' or '0-0 energy').

For the fitting we use two effective modes from the resonance Raman (a C=C breathing/stretching mode at ∼190 meV and an *in-plane* mid-frequency mode at ∼140 meV) as well as a low-energy mode with variable energy. All other parameters were allowed to vary and the fits are shown in Figure 4.3 for C8-BTBT-C8 and di-BT, with parameters in Table 4.2. The fit for C8-BTBT-C8 is good. di-BT showed some self-absorption in the 77 K spectrum which accounts for the suppressed 0-0 feature, otherwise the fit is reasonable. The low-energy vibrational mode at ∼60-70 meV corresponds to an *in-plane* breathing motion that has also been suggested to be involved in charge-transfer in C8-BTBT-C8 [98]. We note scattering *artefacts* in the BTBT and BTBT-C8 spectra prevented analysis of the 77 K spectra for these materials.

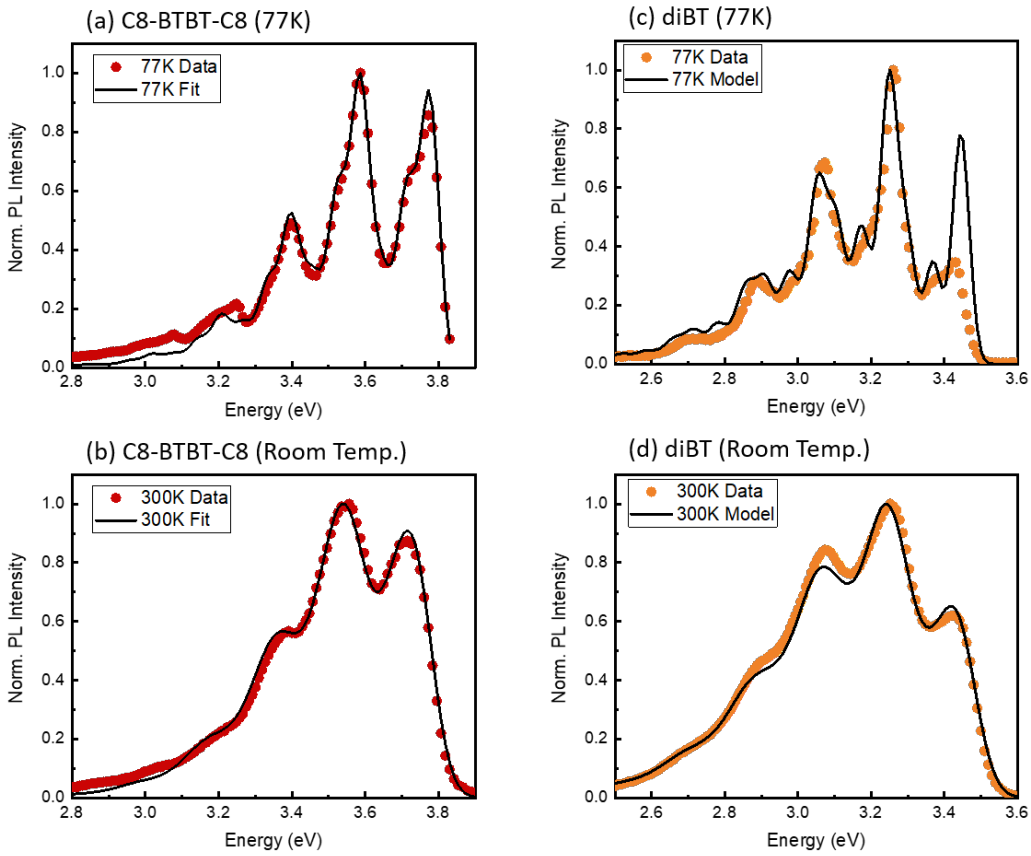

Figure 4.3. Franck-Condon Analysis of fluorescence spectra. Excitation at 310 nm (4.0 eV) in toluene:ethanol:diethyl ether (1:1:2) solvent mixture. (a) C8-BTBT-C8 at 77 K, (b) C8-BTBT-C8 at room temperature, (c) di-BT at 77 K, (d) di-BT at room temperature. Fitting (solid black lines) were performed following equation 4.1, the parameters used are shown in Table 4.2. Suppressed 0-0 feature in di-BT at 77 K is due to self-absorption. 77 K spectra of BTBT-C8 and BTBT showed sufficiently scattering in the fluorescence region and are therefore not shown.

Having fitted the 77 K spectrum, the room temperature spectrum was fitted varying only $\hbar\omega_0$, and the broadening compared with the 77 K fit (Figure 4.3, Table 4.2). The fits are good. The red-shift in the zero-phonon energy ($\hbar\omega_0$) when going from 77 K to 300 K for C8-BTBT-C8 is found to be ~0.036 eV. This is similar to the ~0.02eV shift in anthracene spectra with temperature that has been explained as due to a change in solvent density causing a change in refractive index (dielectric environment) [99]. Room-temperature specta of BTBT and BTBT-C8 (see Figure 4.1) were fitted using a single effective vibrational mode, and the parameters are shown in Table 4.2.

	C8-BTBT-C8		di-BT		BTBT	BTBT-C8
	77 K	300 K	77 K	300 K	300 K	300 K
broadening, σ	26 meV	49 meV	23 meV	52 meV	60 meV	60 meV
$\hbar\omega_0$	3.776 eV	3.740 eV	3.445 eV	3.436 eV	3.66 eV	3.66 eV
S_1	0.644		0.436		1.36	1.46
E^1_{vib}	62 meV		76 meV		164 meV	164 meV
S_2	0.145		0.409			
E^2_{vib}	138 meV		144 meV			
S_3	0.911		1.117			
E^3_{vib}	189 meV		194 meV			
$\sum_i S_i E^i_{vib}$	232 meV		309 meV		223 meV	239 meV
λ	46 meV	51 meV	40 meV	52 meV	70 meV	70 meV
E_{reorg}	278 meV	283 meV	349 meV	361 meV	293 meV	309 meV

Table 4.2. Franck-Condon fitting parameters for fits in Figure 4.3. σ is the broadening of the Gaussian line function; $\hbar\omega_0$ is the 0-0 energy; S_i is the Huang-Rhys parameter of effective vibration i and E^i_{vib} is the corresponding vibrational energy. Note that only 300 K spectra were fitted for BTBT and BTBT-C8 using a single effective mode.

The total reorganization energy in going from S_1 to S_0 can be determined using

$$E_{reorg} = \sum_i S_i E^i_{vib} + \lambda \tag{4.2}$$

where i denotes an effective vibrational mode with Huang-Rhys parameter S_i and vibrational energy E^i_{vib} and λ is the Marcus-type reorganization energy associated with low-energy modes that can be treated classically in the high temperature limit [100]. These modes include solvent and intra-molecular modes such as librations and torsions. S_i and E^i_{vib} are obtained from the fits (Figure 4.3 and Table 4.2) and λ can be estimated from the broadening, σ, of the room temperature fluorescence using $\lambda = \sigma^2/2k_BT$ (as in Table 4.2) or from the measured Stokes' shift using $\lambda = E_{Stokes}/2$, where E_{Stokes} is defined as being the 0-0 peak energy difference between absorption and fluorescence.

di-BT has a larger S_1-S_0 reorganization energy than the BTBT derivatives. This is not only due to coupling to low-energy torsional modes but also due to stronger coupling to the in-plane C=C stretching modes. As we can fit both the 300 K and 77 K spectra with the same parameters, we find that the main part of the reorganization energy does not change with temperature, as expected. However, the change in broadening with

temperature cannot be explained using simple Arrhenius arguments and therefore we suggest that some of the low-energy vibrational modes are frozen out at 77 K.

For completeness, Figure 4.4 shows the room-temperature fluorescence fits and the corresponding expected mirror-image absorption feature, shifted by 10 meV for C8-BTBT and 80 meV for di-BT. Note that di-BT shows almost perfect mirror symmetry.

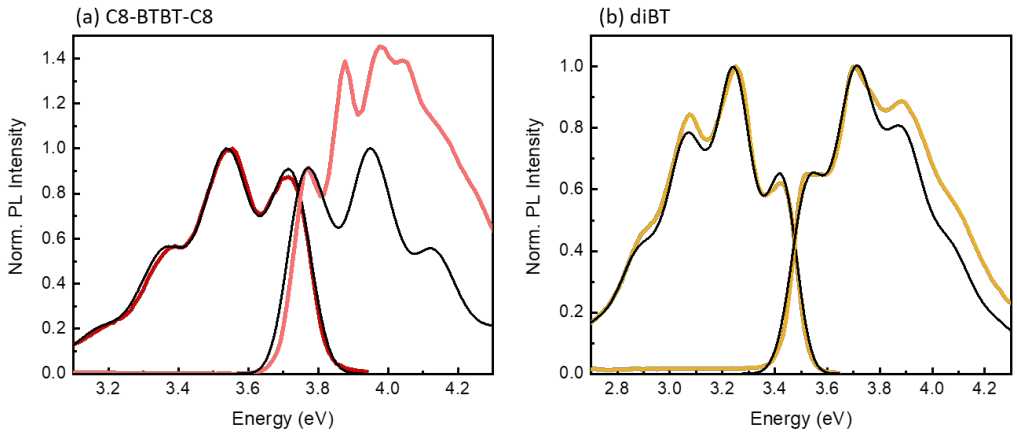

Figure 4.4. Mirror symmetry from Franck-Condon Analysis. Fluorescence and absorption spectra of (a) C8-BTBT-C8 and (b) di-BT together with fits to the fluorescence spectra (black, see Figure 4.3 and Table 4.2) and the corresponding mirror-image absorption spectra.

4.2.4 Franck-Condon Analysis of the phosphorescence spectra.

We can perform similar multi-mode Franck-Condon analysis of the 77 K phosphorescence spectra where all parameters are allowed to vary. These are shown in Figure 4.5 with parameters in Table 4.3. Despite the number of parameters, the fits are well constrained by the complexity of the spectra and we find that the parameters do not change significantly between BTBT derivatives, as expected for a localised triplet. We note that the spectra cannot be fit using only two effective vibrational modes, but including four, rather than three, does not improve the fit. Interestingly, the reorganization energy of the T_1-S_0 transition is larger in the planar BTBT derivatives than in di-BT. This is the opposite trend than we observed for the fluorescence fits.

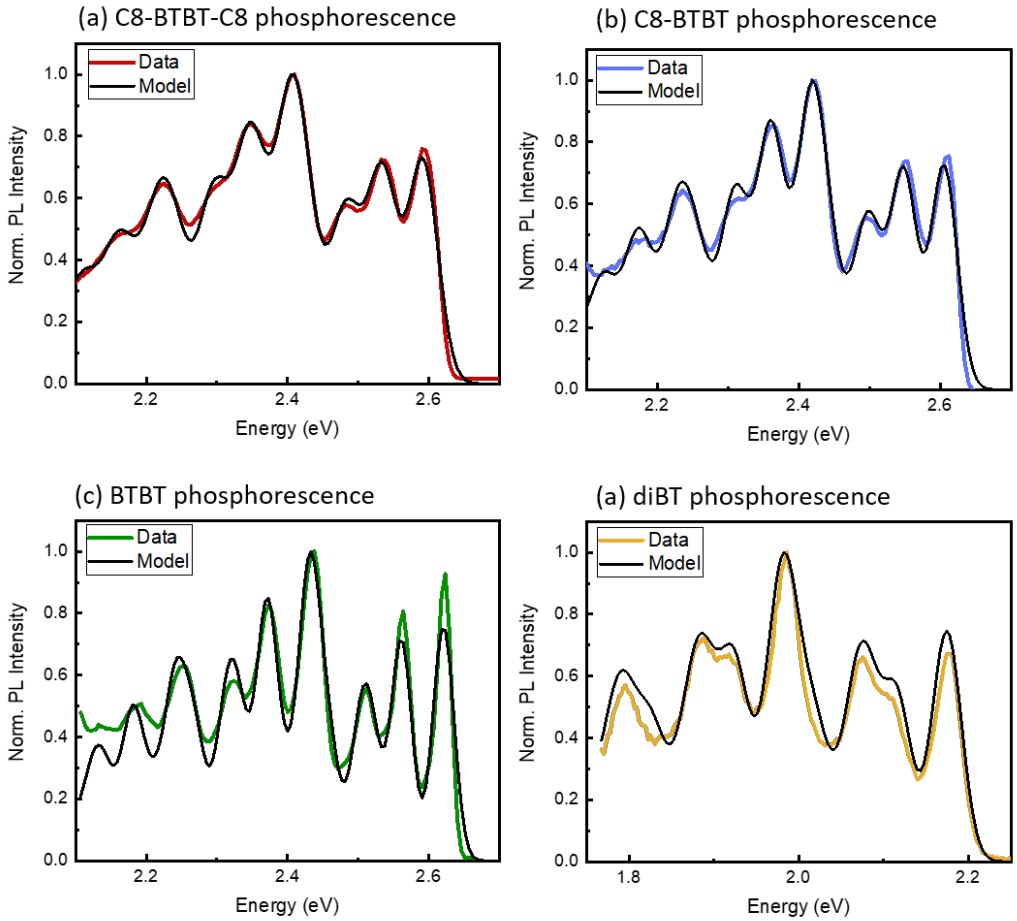

Figure 4.5. Franck-Condon Analysis of phosphorescence spectra. Excitation at 310 nm in solvent mixture at 77 K (see methods). (a) C8-BTBT-C8, (b) BTBT-C8, (c) BTBT, (d) di-BT. Fit parameters are shown in Table 4.3.

	C8-BTBT-C8	di-BT	BTBT	BTBT-C8
σ (broadening)	21 meV	17 meV	15 meV	19 meV
$\hbar\omega_0$	2.592 eV	2.174 eV	2.621 eV	2.605 eV
S_1	0.931	0.700	0.938	0.961
E^1_{vib}	58 meV	59 meV	59 meV	57 meV
S_2	0.370	0.776	0.441	0.362
E^2_{vib}	102 meV	98 meV	102 meV	100 meV
S_3	1.013	0.862	1.057	1.065
E^3_{vib}	187 meV	191 meV	190 meV	188 meV
$\sum_i S_i E^i_{vib}$	281 meV	282 meV	0.301 meV	0.291 meV
λ	33 meV	22 meV	17 meV	27 meV
E_{reorg}	314 meV	304 meV	318 meV	318 meV

Table 4.3. Franck-Condon fitting parameters for fits in Figure 4.5. σ is the broadening of the Gaussian line function; $\hbar\omega_0$ is the $0-0$ energy; S_i is the Huang-Rhys parameter of effective vibration i and E^i_{vib} is the corresponding vibrational energy. Note that only 300 K spectra were fitted for BTBT and BTBT-C8 using a single effective mode.

4.2.5 Empirical determination of the S_1-T_1 Reorganization Energy

Table 4.4 compares the E_i^{vib} and S_i for the three effective vibrational modes for the S_1-S_0 and T_1-S_0 transitions for C8-BTBT-C8 and di-BT.

	C8-BTBT-C8				di-BT			
	S_1-S_0		T_1-S_0		S_1-S_0		T_1-S_0	
	E_{vib} (meV)	S	E_{vib} (meV)	S	E_{vib} (meV)	S	E_{vib} (meV)	S
Mode 1	62	0.64	58	0.93	76	0.44	59	0.70
Mode 2	138	0.15	102	0.37	144	0.41	98	0.86
Mode 3	189	0.91	187	1.01	194	1.12	191	0.86

Table 4.4. Franck-Condon fitting parameters for fits in Figures 4.3 and 4.7.

We note that the high- and low-energy vibrational modes ($\sim$190 meV and $\sim$60 meV) do not change much, suggesting similarity in the S_1 and T_1 geometries along these normal mode co-ordinates. However, the mid-energy effective mode changes from $\sim$140 meV for S_1-S_0 to $\sim$100 meV for

T_1-S_0. Examination of the DFT-calculated Raman spectrum, depicted in Figure 4.6, suggests that this shift may be due to the involvement of modes with an *out-of-plane* component [101].

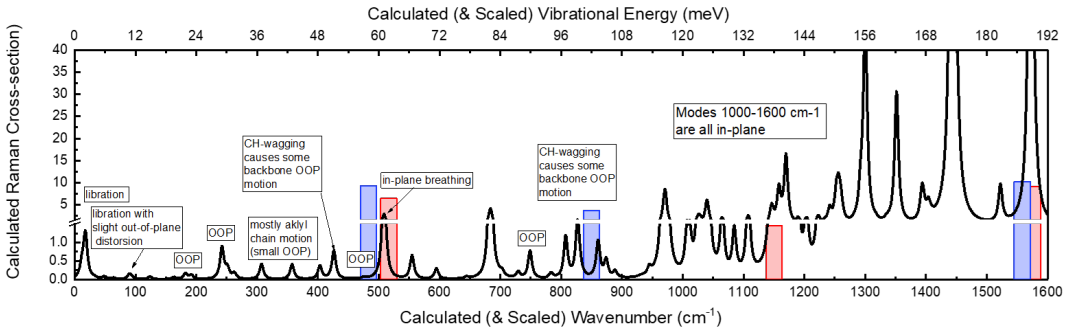

Figure 4.6. Calculated ground-state Raman spectrum for C8-BTBT-C8. The vibrational mode energy is scaled according to [102]. Shaded rectangles denote Franck-Condon effective modes from fluorescence (red) and phosphorescence (blue) fitting. The low (∼60 meV) and high (∼190 meV) modes do not shift significantly between fluorescence and phosphorescence. The shift in the mid-range mode is more pronounced. We tentatively attribute this to stronger coupling to *out-of-plane* modes in phosphorescence [101], which shifts the effective mode to lower energies compared with fluorescence.

Using the values in Table 4.4, we can estimate an effective reorganization energy in going from S_1 to T_1. This is illustrated in Figure 4.7. As both the fluorescence and phosphorescence are measured relative to the same state (S_0), we can estimate the relative shift of the potential energy surfaces between S_1 and T_1. From this, we can calculate the effective Huang-Rhys parameter for the different modes using:

$$(\Delta Q_{S_1-T_1})^2 = ((\Delta Q_{S_1-S_0}) \pm (\Delta Q_{T_1-S_0}))^2 \tag{4.3}$$

and assuming that the Huang-Rhys factor is unlikely to be much larger than 1. From this analysis, we determine a single effective vibrational mode couples S_1 and T_1. For C8-BTBT-C8 (di-BT), the effective vibrational energy is 0.11 eV (0.11 eV) with a corresponding Huang-Rhys parameter of 0.54 (1.22). We will use this value to benchmark our calculations and to estimate the Franck-Condon-weighted density of states during intersystem crossing, as described below.

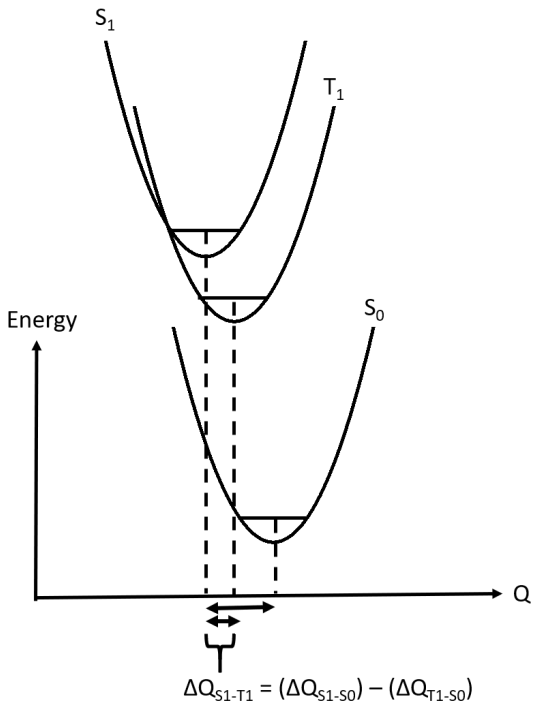

Figure 4.7. Schematic Potential Energy Surfaces of T_1 and S_1 relative to S_0. From our Franck-Condon analysis of the fluorescence and phosphorescence spectra, we have estimated an effective change in normal-mode co-ordinate $\Delta Q \propto \sqrt{S}$ (S is the Huang-Rhys parameter) for low, mid-range and high vibrational modes with respect to S_0 (see Table 4.4). As depicted in the diagram, this allows us to estimate the effective shift in co-ordinate between S_1 and T_1 given by $\Delta Q_{S_1-T_1} = \Delta Q_{S_1-S_0} \pm \Delta Q_{T_1-S_0}$, which in turn provices an effective Huang-Rhys parameter for coupling between S_1 and T_1. This is used to benchmark our calculations below.

state decay is dominated by intersystem crossing

. We now move on to examine the excited-state processes that occur following excitation. The simplest indication of the balance of radiative and non-radiative processes is given by the photoluminescence quantum yield (PLQY). This is reported in Table 4.5 for dilute solutions of the BTBT derivatives.

	C8-BTBT-C8	BTBT-C8	BTBT	di-BT
PLQY (%)	3.4 ±0.7	3.4	3.8 ± 0.7	29 ±4
Triplet yield (%)	51±7		63±8	52±4

Table 4.5. Photoluminescence and triplet yields in dilute solution (10μM in toluene). Measurements were repeated 5 times with different samples. The reported values are the mean and standard deviation. We note that it is surprising that the photoluminescence and triplet-yields do not sum to 100%. This is either because of significant non-radiative decay (unlikely, see below) or due to systematic error in the measurements, which are notoriously error-prone. We therefore make the reasonable assumption that 1-PLQY is an upper bound on the triplet yield.

We find that the PLQY is low ∼4% in BTBT derivatives, compared with 30% for diBT. For comparison, we note that the PLQY of other flexible oligothiophenes in solution is 30-40%, despite significant intersystem crossing [103]. However, previous reports on fused molecules with benzothiophene motifs have widely varying triplet yields, many close to unity [91, 104]. A literature review suggests that the low PLQY in similar materials arises due to rapid intersystem crossing and a correspondingly high yield of triplet excited states [91]. Using triplet-yield measurements, Table 4.5, we find that the triplet yields are indeed high. The discrepancy between PLQY and triplet yield suggests either significant internal conversion (IC) from S_1 to the ground-state or error in the triplet yield measurements. From our transient absorption results below, and the number of steps involved in triplet yield determination, we suspect the latter, Figure 4.8.

4.2.6 Fast (∼150ps) intersystem crossing in BTBT derivatives

To investigate ISC in these molecules, we performed transient absorption spectroscopy. In Figure 4.8 we plot the change in transmission as a function of time for the three BTBT derivatives, excited at their S_1 0-0 energy (3.75 eV). As we plot changes in the transmission rather than absorbance, excited-state absorption is negative, with stimulated emission showing up as a positive signal. At 5 ps, the spectra of all four BTBT derivatives are dominated by stimulated emission (above 3.2 eV) and excited-state absorption (peaked at 2.2-2.4 eV). We assign these features to the photoexcited S_1 state as both features decay together leaving an excited-state absorption peaked at 3 eV. This is confirmed by measurement of the S_1 fluorescence of C8-BTBT-C8 using a Streak Camera (Figure 4.8 panel (e) pink triangles), which shows that the fluorescence decay matches the excited-state absorption decay at 2.4 eV. Excitation into the S_2 band at 3.86 eV shows similar transient absorption spectra

and dynamics within our time resolution of ~200 fs, suggesting fast internal conversion between S_2 and S_1, as expected given the proximity of the states and the S_1-like emission spectrum. We also observed no significant solvent dependence, nor concentration dependence neither excitation wavelength dependency.

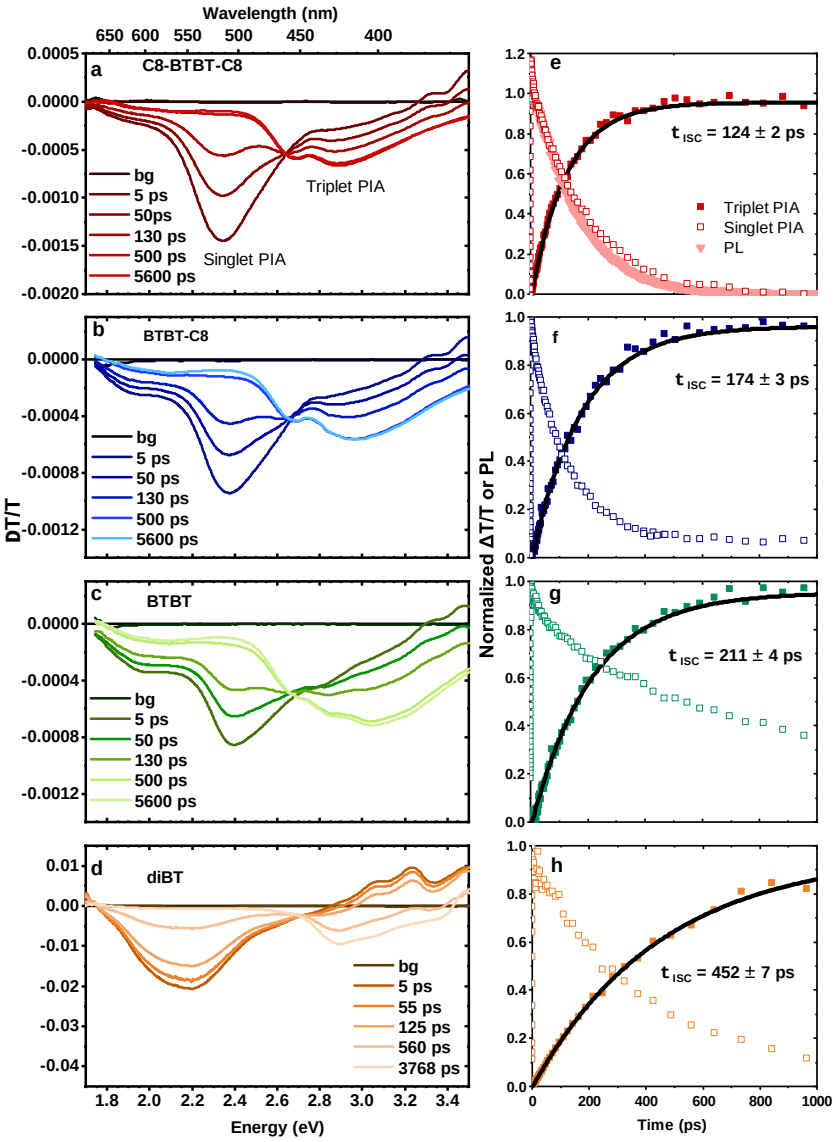

Figure 4.8. Transient absorption spectroscopy of BTBT derivatives.(a)-(d) show transient absorption spectra of C8-BTBT-C8, BTBT-C8, BTBT and di-BT respectively. (e)-(h) show transient absorption (squares) and photoluminescence (triangles) *kinetics* of the same materials. Measurements were performed in dilute toluene solution with excitation at 320 nm (3.87 eV). Solid black lines show monoexponential fits to the triplet rise-time with the extracted intersystem crossing time-constant as an inset.

We assign the excited-state absorption band at 3 eV to triplet T_1-T_n absorption as it does not decay during the timescale of our measurement (7 ns), further supported by the fact that we observe phosphorescence on the same nanosecond timescales (Figure 4.9). In addition, the spectral shape is similar to reported T_1-T_n absorption spectra of benzothiophene and dibenzothiophene [91, 92].

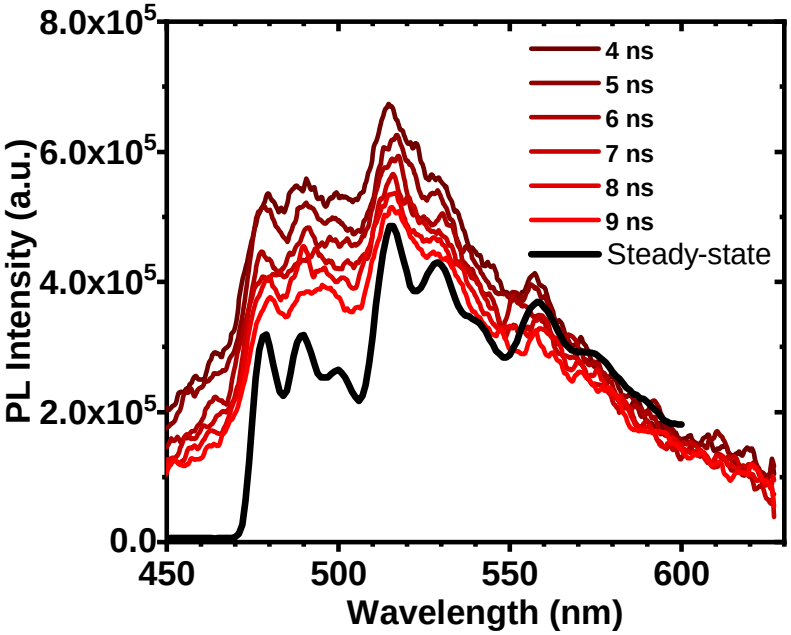

Figure 4.9. C8-BTBT-C8 Transient phosphorescence spectra at 77 K. The figure demonstrates the presence of phosphorescence at 4 ns after excitation, measured using an intensified gated CCD with excitation at 320 nm in toluene: ethanol: diethyl ether (1:1:2) solvent mixture at 77 K. The subsequent decay of the blue-green (450-550 nm see figure 3.6) spectral region is due to triplet relaxation, although it is likely to be an artefact of the measurement due to the very weak signal during the nanosecond gate window and overlap with tail fluorescence (possibly from a minority of undissolved dimers). Clear triplet emission peaks are nevertheless observed when compared with the steady-state spectrum (in solid black line) and the red-edge of the spectrum does not decay, as expected.

The presence of an isosbestic point in the transient absorption spectra demonstrates negligible population of any intermediate states or spectral relaxation. The intersystem crossing consequently, must proceed either via higher-lying triplet states (T_n) followed by rapid internal conversion in the triplet manifold ($\ll$100ps) or directly from S_1 to T_1. The time-scale of intersystem crossing in these molecules ($\sim$150ps) also means that intersystem crossing occurs from the relaxed S_1 state, as relaxation within the singlet manifold is expected to be

complete within at most a few 10's of picoseconds.

The rate of intersystem crossing for the different molecules are shown in Table 4.6 using the S_1 lifetime and either the triplet yield or (1-PLQY) (Table 4.5) assuming negligible S_1 non-radiative decay. Interestingly, the rate of intersystem crossing increases with the number of alkyl chains by roughly a factor of 2, from $1/213\,ps^{-1}$ in BTBT to $1/124\,ps^{-1}$ in C8-BTBT-C8. This trend is opposite to that observed from ESR spectroscopy [59, 86].

	C8-BTBT-C8	di-BT	BTBT	BTBT-C8
k_{isc}^{PLQY} [a] (1/ps)	1/124	1/590	1/213	1/153
$k_{isc}^{Triplet}$ [b] (1/ps)	1/235	1/810	1/326	

Table 4.6. Rate of intersystem crossing calculated using fitted S_1 lifetimes and [a] using (1-PLQY) as an upper triplet-yield limit or [b] the triplet yield from Table 4.5.

Figure 4.10 shows how the fluorescence decay changes with temperature. We note that the decay slows down as temperature decreases but remains mono-exponential down to 77 K, with very little change in lifetime below 150 K.

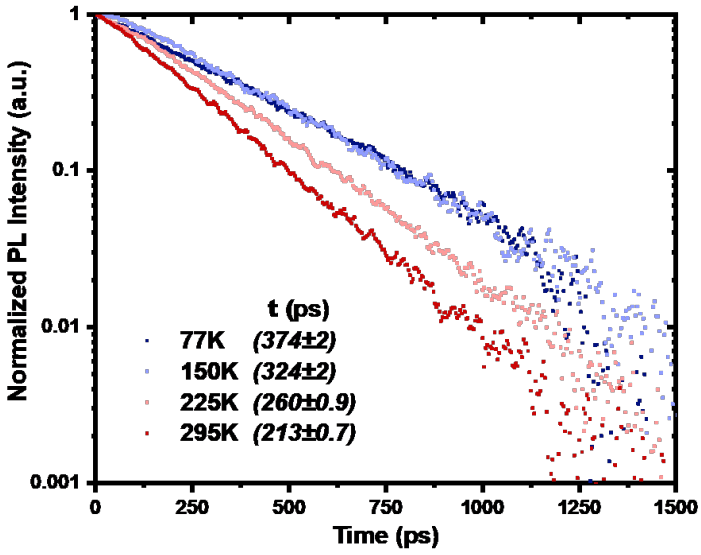

Figure 4.10. Temperature dependence of the fluorescence lifetime for BTBT in toluene:ethanol:diethyl ether (1:1:2) solvent mixture, measured using a streak camera and plotted on a log/linear scale to emphasise the monoexponential decay. Fitted time-constants are shown in the legend.

The rate of intersystem crossing in the weak coupling regime (i.e. when the spin-orbit coupling matrix element is small compared with the energy separation between states) can be approximated using Fermi's Golden Rule:

$$k_{isc} = \frac{2\pi}{\hbar}|SOCME|^2\rho, \tag{4.4}$$

where ρ is the density of final states and SOCME is the spin–orbit–coupling matrix element between S_1 and T_n given by $\langle T_n | H_{SOC} | S_1 \rangle$. In the harmonic approximation, ρ is given by the Franck-Condon Weighted Density of States. Typical values of this density of states are $\sim 10\,\mathrm{eV}^{-1}$ [105].

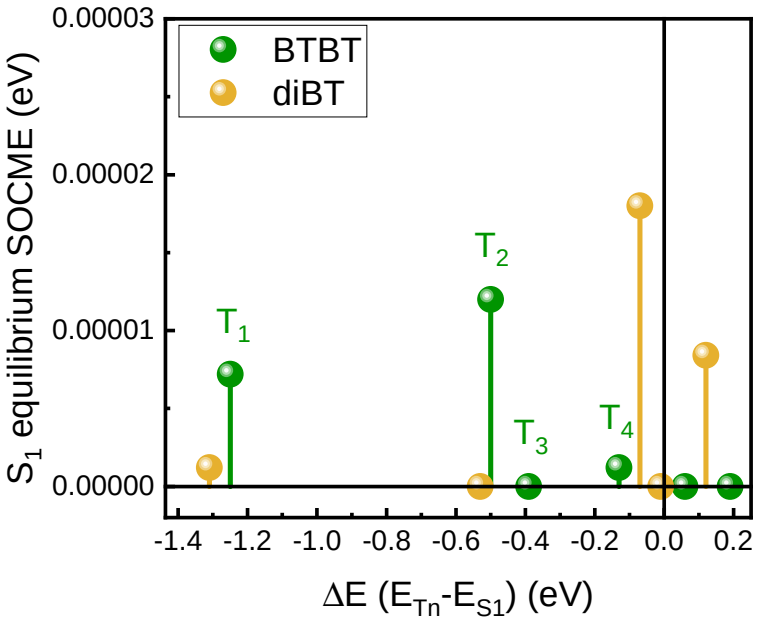

Figure 4.11. Spin-Orbit Coupling Matrix Elements $\langle T_n | H_{SOC} | S_1 \rangle$ at S_1 equilibrium geometry for BTBT (green) and di-BT (orange) plotted against the energy difference between T_n and S_1.

We calculated the spin-orbit coupling matrix elements between S_1 and the lowest 20 triplet excited states at both the Franck-Condon geometry and at the S_1 equilibrium geometry. Example calculations for BTBT and di-BT at the S_1 equilibrium geometry are shown in Figure 4.11. Using equation 4.4, we note that even for large densities of states (e.g. $10\,\mathrm{eV}^{-1}$ for each triplet), our SOCMEs give ISC rates of $\sim 1/(100\,\mathrm{ns})$ for di-BT and $\sim 1/(300\,\mathrm{ns})$ for BTBT: three orders of magnitude smaller than observed and with the opposite trend compared with experiment. These calculations demonstrate that direct *i.e.* pure electronic) intersystem crossing cannot explain the experimentally observed rates.

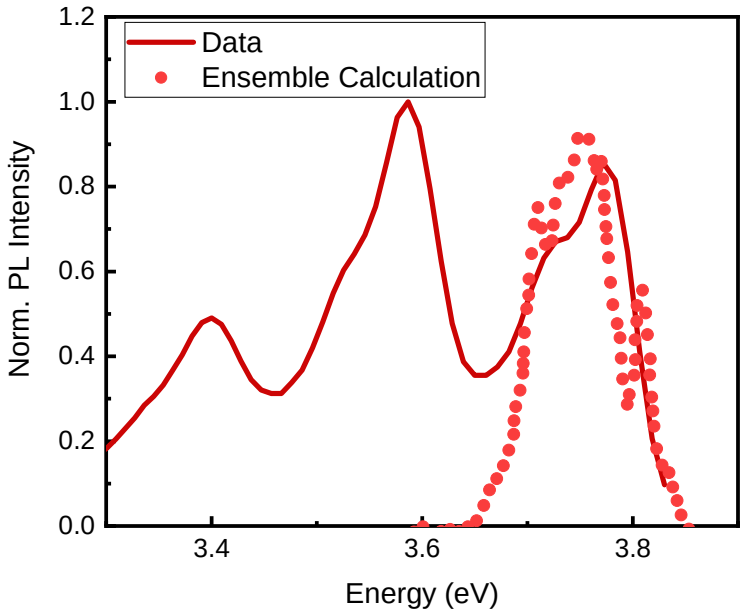

(a) 77 K

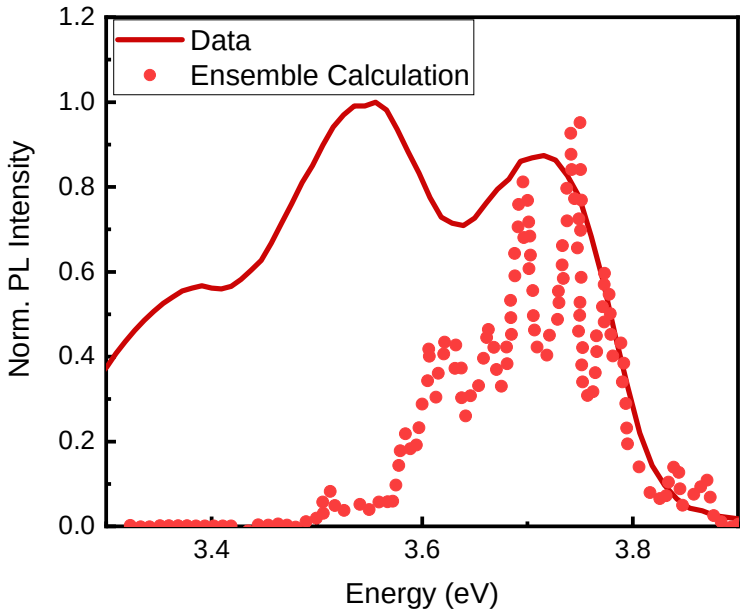

(b) 300 K

Figure 4.12. Comparison between calculated S_1 oscillator strengths using ~400 snapshots from MD simulations and measured fluorescence for C8-BTBT-C8 at (a) 77 K and (b) 300 K. The calculated spectra have been shifted by 0.13 eV to line up the high-energy edge and are convoluted with a Lorentzian lineshape of width 0.01 eV. We have not included a full quantum treatment of high energy modes in these calculations and so only the 0-0 energy is observed. The structure in the MD calculations is noise from under sampling.

4.2.7 Vibronic spin-orbit coupling.

Our inability to explain the experimental results using only direct intersystem crossing suggests that we cannot neglect the role of nuclear motion on the intersystem crossing process, i.e. the spin-orbit coupling between states can be considered to be modulated by certain 'inducing' vibrational modes. This is phenomenologically similar to the case of charge-hopping in organic semiconductors,[106]. The spin-orbit coupling between states S_1 and T_n can be near zero on average. However, displacement of certain nuclear modes may induce a coupling proportional to the displacement.
To attempt to qualify the nature of these inducing modes, we turn to molecular dynamics calculations. Here, we calculate the molecular dynamics of molecules in the ground- and the first excited singlet–states. To benchmark the calculations against experiment, we compare the calculated and experimental fluorescence spectra at 300 K and 77 K in Figure 4.12 [107]. We find that the calculated distribution matches the experimental broadening and that the calculated S_1-S_0 and T_1-S_0 reorganisation energies at 77 K (~200 meV and ~350 meV, respectively, calculated using an arithmetic mean) match the experimental values (232 meV and 281 meV) reasonably well. We also find that the calculated S_1-T_1 reorganization energy (0.11 eV) matches our experimentally determined value (0.06-0.13 eV) reasonably well. The broadening in the ensemble spectra reflects coupling to low-energy vibrational modes that can be treated classically and is related to λ, the classical Marcus reorganization energy with some effect from zero-point fluctuations.

We calculate the distribution of SOCMEs between S_1 and T_n and determine a mean value. These are shown in Figure 4.13 for the different triplet levels. Compared with the equilibrium values in Figure 4.11, the ensemble values are significantly larger. The intersystem crossing rate scales with the square of the SOCME (see equation 4.4) and therefore such changes will have a large impact on k_{isc}.
We estimate the rate of intersystem crossing using Marcus-Levich-Jortner (MLJ) formalism for the Franck-Condon Weighted Density of States. The MLJ density of states is given by

$$\rho_{FCWD}^{MLJ}(\Delta E) = \frac{1}{\sqrt{4\pi\lambda k_B T}} \sum_m \left[\frac{S^m e^{-S}}{m!} \times exp\left(-\frac{(\Delta E + \lambda + m\hbar\omega)^2}{4\lambda k_B T} \right) \right] \tag{4.5}$$

which includes a high-energy effective accepting mode ($\hbar\omega$) that must be treated quantum mechanically with Huang-Rhys parameter S and classical Marcus-type reorganization energy λ. By varying these parameters, we can estimate k_{isc}.

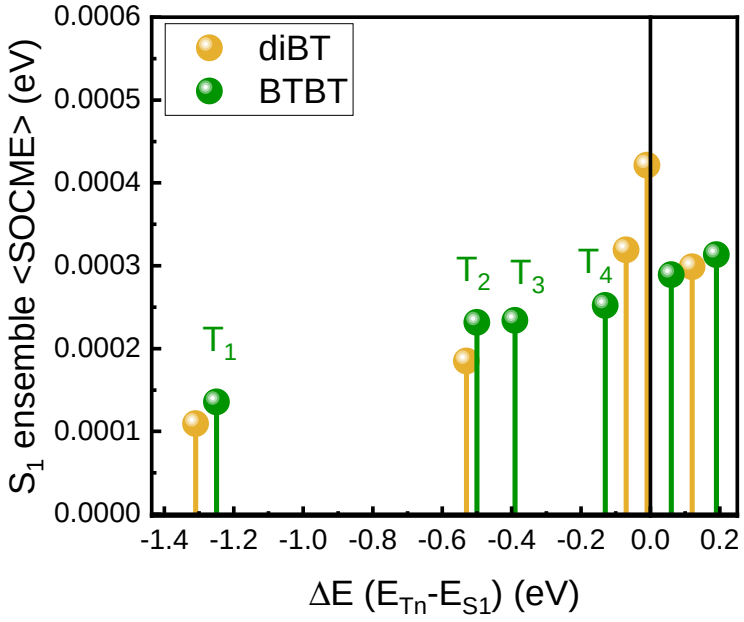

Figure 4.13. Ensemble-averaged Spin-Orbit Coupling Matrix Elements $\langle T_n | \widehat{H}_{\text{SOC}} | S_1 \rangle$ at S_1 geometry for BTBT (green) and di-BT (orange) plotted against the energy difference between T_n and S_1. Compared with the equilibrium geometry values in Figure 4.11, the ensemble values are over an order of magnitude larger.

Taking $\hbar\omega$ = 0.11 eV and S=0.5 (BTBT) and S=1 (di-BT) from our spectral analysis, and naïvely assuming similar values for all T_n, we vary λ and calculate the k_{isc}. This is shown in Figure 4.14. While the calculated values are roughly an order of magnitude smaller than the experimental ones, they nevertheless indicate an improved model for understanding ISC in BTBTs.

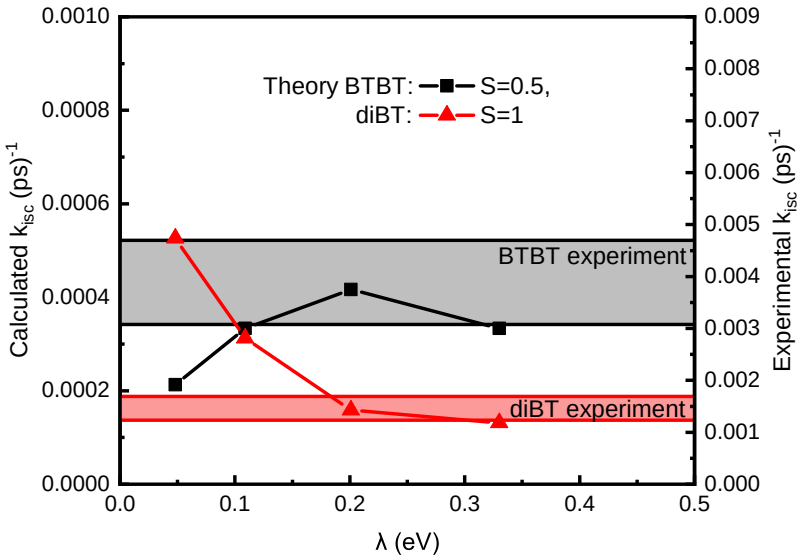

Figure 4.14. Calculated (left) and experimental (right) rates of intersystem crossing. The calculated values are plotted as a function of λ, the classical Marcus reorganization energy, see text for details. The experimental spread is calculated from the PLQY/Triplet yields in Table 4.5.

The ratio of BTBT/di-BT rates matches experimental values for $\lambda \sim 0.2$ eV, which is unexpectedly large. We also find that the theory cannot yet account for the slight observed temperature-dependence of k_{isc} shown in Figure 4.15.

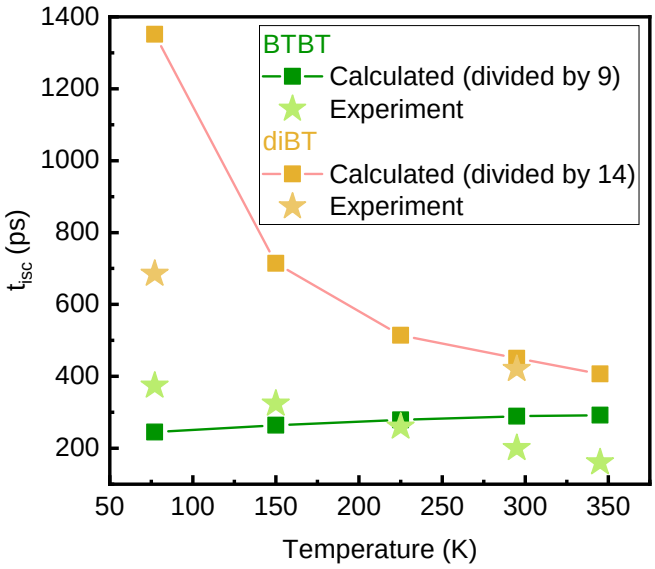

Figure 4.15. Experimental determination of k_{isc} for BTBT and di-BT (stars) compared with calculated rates. The rates have been calculated by varying the FCWD with temperature but keeping the SOCME and effective state energies constant. Factors account for diverse fitting stages and to compensate overstimation in the DFT calculations.

Nevertheless, we find that the calculated k_{isc} approaches the experimental value when the vibronic spin-orbit coupling is taken into account. To determine the effective tuning modes responsible for increasing the SOCME we have performed a principal component analysis of molecular motions that are correlated with increased SOCME. We find that the motion responsible for increased SOC can be isolated to a small number of components (57%, 3 components, ∼100% 8 components) of motions. The most important of these comprise ring-breathing and ring flexing motions, and are largely the same at all three temperatures and, surprisingly, in C8-BTBT-C8, BTBT and di-BT.

4.3 Conclusions

Spin-Orbit Coupling in high-mobility organic semiconductors is known to impact s*pin-relaxation* and intersystem crossing. However, understanding its molecular foundations remains as challenging as ever, SOC has been studied in *charged* molecules of BTBT derivatives and C8-BTBT-C8 molecules as well using ESR spectroscopy [59, 86]. Our work offers a deep view of SOC in neutral molecules[2], characterised via the intersystem crossing. We have found that intersystem crossing in these highly planar materials can only be explained by going beyond the Born-Oppenheimer approximation and include spin-vibronic terms. We also find that, *contrary* to previous studies [59, 86], the effective SOCME is *larger* in alkylated derivatives compared with the bare BTBT core. We believe that the only possible way to make compatible both results without completely discarding what the previous research showed, by the account of being mutually exclusive. It is to note, that the difference between the two measurements lies on the nature of the *charge density distribution* within the molecule[3]. We simply need to observe that patent difference in geometry between charged and neutral molecules. Our result further implies that a generic molecular SOC is not a meaningful approximation. We have fulfilled the questions posed at the set-up: on the origin of such anomalous absorption spectra, on the types of optical excitations created in the material and lastly, on the time scales and fates of such photogenerated excitations. We are now in a position to take these results as a model, as our *working-horse* for the rest of the Thesis.

Finally, note that it will be interesting to determine the effect of SOC on intersystem crossing in BTBT derivatives in the solid-state and indeed this is partially addressed in chapter 6. Excitonic interactions in the solid-state stabilise the singlet with respect to the triplet manifold. Naïvely, this would suggest more overlapping of the density of states, which translates in more triplet states on resonance with S_1, thus potentially leading to a rise in the effectiveness of the intersystem crossing rate. However, it is also likely that the low-energy vibrations responsible for inducing SOC in BTBT derivatives in solution are likely to be altered - or even *damped* - by solid-state interactions [94]. We find that SOC is highly sensitive not only to spin density distribution [59, 86], but also to coupling to low-energy vibrational modes. This opens the possibility to use vibronic tuning to alter spin behaviour, or spin–coherence, either through

[2] Which for some electronic devices is what matters.

[3] This is why is so vital to **grasp** the *tenet* of Density Functional Theory, where we care only about the *density* which minimises the ground state energy, which incidentally has one–and–only–one *space-geometry*, hence, by definition, a charged state cannot be a valid energy for the ground state, for it is an excited state. Moreover, let us remember that DFT formalism alone is restricted to the ground state, although Time–Dependent can be incorporated within the DFT framework in what is called (TD-DFT) which deals particularly well with excited states [35].

molecular design or even by optical excitation of specific vibrational modes [8].

5 BTBT substituted derivatives.

By replacing an existing atom or interchanging a functional-group in the molecules or macromolecules, we are effectively changing the electronic structure of the compound. When modifying the electronic structure, we are also doing a shift in the local electronic density which in turn modify the molecular dipole moment. When an electron-withdrawing atom or group is introduced in the molecular back-bone, it may induce changes in the electron cloud distribution hence changing the value of the transition dipole moment. In other words, since molecules as well as aggregates have intrinsic dipole moments due to the nature of the non-uniform distribution of positive and negative charges, this distribution gets modified upon substitution of an atom. This is of importance because it can tell us how molecules interact with electromagnetic radiation, and as we know that is what determines their photophysical properties too.
On the other hand, if we think of the model of ball and springs for atomic bonding, we can think of a change in the mass of one or many of the balls, as a result of exchange in the atomic number of the substituent atom. Ultimately this alters the force connecting the atoms, the importance of this resides from the fact that a change in the spring–constant is what finally leads to a shift in the frequency of the oscillations of the molecules. These oscillations refer to the equilibrium position a measure of the bond–length joining the atoms, in other words, they take place on the line forming the bonds, so after the introduction of a substituent group or atom the equilibrium position shifts from the unsubstituted molecule, as well as their associated vibrational modes. The substitution of heteroatoms in the π-conjugated system can significantly alter the local electron density and the bonding type and therefore affect the overall molecular properties. What we are seeing then, is that the tuning of the properties of a given material should possibly be controlled by design. So, that is why we do expect to see some impact on the spectroscopic properties of the molecules upon modifying the structure through substitutions.

5.1 Introduction

Usually, a starting point for novel development of organic semiconductors is to initiate with a known compound (*e.g.* pentacene, thiophene, pyrene etc) or a family of materials, like the *acenes* or fused *oligothiophene*s and modify

the structure step-wise. π-conjugated small molecules have received special attention for many reasons, one is because they provide significant advantages due to their limited π-extended core that can be easily modified with a variety of functional groups to finely adjust their optoelectronic and physicochemical properties. Additionally, their relatively simple synthesis, synthetic reproducibility, ease of purification, and high solubility are superior to their polymer counterparts. The substitutional approach has its origin from various sources, mainly to the need of developing better and more efficient materials to make organic semiconductors, on the other hand, to improve solubility, thermal stability, protection from oxidation or optical stability. These approaches have one goal in common, which is to significantly enhance some properties of the parent molecule. For instance, in the case of the acenes, we know that the anthracene and pentacene have excellent semiconducting properties but they lack either solubility or photostability, so in this particular case, the synthetic approaches end to address these issues. As in many processes, there are always compromises, a recurring drawback is achieving the same or better values for a given property after substitution. Like the charge carrier mobility of the parent molecule, for example in pentacene is quite high but not so in its derivatives. The nature of the substitutions is also important in intermolecular interactions, hence in molecular packing of organic crystals which is largely determined by the molecular structure itself. Like all small–ring compounds they are stabilized by bulky substituents. A simple and very bulky alkyl substituent is the *tert*-butyl group, which has been used by many authors to stabilize reactive moieties [21, 108, 109] and it also serves to hinder rotational interconversion. For molecules that resemble the acene backbone, the introduction of halogen atoms at the terminal benzene ring does not alter the planarity but modulates the bond lengths of the acene backbone [110]. In an interesting shift on approach, a team of researchers instead of substituting the thiophene ring or its derivatives, they rather attach a bithiophene (and a phenyl) to benzene and naphthalene ring [111]. It was found that the distance between the *ipso*-carbon[1] atoms of the thiophene rings is of importance since it induces dipole-dipole interactions affecting the molecular structure, photophysics and electrochemical properties as well as the photoluminescence [111]; compared with phenyl substitution bithiophene showed a bathochromic shift, their emission has a more n-π^* character and higher quantum efficiencies as well as longer lifetimes than phenyl substitution [111]. They concluded that these significant differences are linked with differences in the molecular structures rather than the symmetry or asymmetry of the molecules [111].

Sequential enhancement of device performance in organic semiconductors (OS),

[1]The ipso– prefix is used when two substituents share the same ring position in an intermediate compound. This could occur in an electrophilic aromatic ring substitution.

in particular OFET, is routinely achieved from two complementary routes: a device structural optimisation approach and strategic development of new organic semiconductors. It is for this reason that research of novel organic semiconductors materials has the possibility of making a breakthrough in the field of OS.
Another important effect caused by substituents are on *frontier orbitals*, those molecular orbitals are of extreme importance for the evaluation of molecular reactivity. Takimiya and coworkers found that highest occupied molecular orbital (HOMO) and lowest unoccupied molecular orbital (LUMO) levels increased by 0.5 eV from non-alkylated molecules to alkyl-substituted ones in thins films but not in solutions [112]. Materials prone to oxidation are more susceptible to donate an electron, which is a consequence of having HOMO with more negative energy[2]. Lowering the HOMO is one method of inducing air stability under transistor device operating conditions [113]. This is a major challenge for the development of practical OFET materials, that have to fulfil not only high performance but also high stability in the environmental conditions of operation. Organic semiconducting materials are actively developed for all these reasons and fulfil their potential. The issues here revolve the need to meet the stringent requirements of desired stability; for oxidation by air, photodegradation, thermal capacity to endure high temperatures, as well as precise control of molecular ordering in the thin-film state.
The majority of organic semiconductors have shown only unipolar transport characteristics in their OFET devices, *i.e.*, either hole-transport (p-type) or electron-transport (n-type) properties. Ambipolar semiconductors allow both holes and electrons to act as the charge carriers, which are important for applications like organic light-emitting transistors OLETs and complementary inverter circuits. This is the reason why ambipolar transistors have gained recently the focus in the research community, where importance is placed in having both n-type and p-type organic semiconductors with similar physical and electrical properties. OS achieving these conditions are difficult to find, for example, pentacene based OFETs exhibit hole mobilities one order of magnitude larger than the electron ones [114], but pentacene derivatives possess electron-transport properties when the aromatic framework is attached to high electron affinity moieties [115]. Moreover, in materials with known p-type or n-type conduction, an effective approach for interconverting them is by altering the chemical structure by adding strong electronegative substituents. In other words, n-type materials are produced by introduction of strong electron-withdrawing groups such as CN to the conjugate core or by substitution of the hydrogen atoms with halogen atoms -*halogenation* (e.g., fluorine, chlorine, bromine and iodine). Carbon–hydrogen–fluorine (C–H–F) interactions are instrumental in supramolecular organization in solid-state, with a typical π-stacking, which enhances the charge carrier mobility [116, 117]. Tuning with strong electronegative substituents, for

[2]With respect to the vacuum level.

example, is an effective approach for converting p-type organic semiconductors to n-type. Experiments on perfluorination done on three homologous classes of polyaromatic hydrocarbons for molecular electronics: acenes, pyrenes, and circumacenes showed a non-negligible change in charge transport properties. Perfluorination of compounds resulted in a reduction of charge-transfer rate in absolute terms. This effect was attributed to higher values of the molecular reorganization energies for perfluorinated compounds. Cardia *et al* [114] found a remarkable similarity in the charge-transfer rates for both holes and electrons of perfluorinated species and when comparing pentacene charge-mobility values with perfluorinated circumacenes they observed an increase upon perfluorination. Moreover, substitution with an electron-withdrawing group leads to the reduction in the adjacent C–C bond lengths, while chlorination elongates the adjacent C–C bond due to chlorine's weak electron-donating capability. These substituents, in turn, affect the electronic structure, which has a direct influence in the electron/hole injection barrier from the electrodes by terms of HOMO/LUMO levels. Understanding how these energy levels shift is of primary importance in device engineering,for instance, it is accepted that having a HOMO (LUMO) level lying within -4.9 to -5.6 eV (-3.6 to -4.5 eV) is highly desirable for it benefits device stability [110]. Low-lying LUMO energy levels under -4.0 eV avoid damage from undesired water or oxygen molecules. On the other hand, the electron affinities (EA) and ionization potential (IP) are closely related to the charge injection from the electrodes, which further determine the stability of the molecule [110, 115, 116].

Pentacene is a benchmark molecule for newly developed small-molecule organic semiconductors with superior hole mobility (even up to 40 $cm^2V^{-1}s^{-1}$) [110]. Pentacene-based electronic applications are limited due to poor ambient stability and solubility, this is why synthetic chemists have modified the molecule, one remarkable example is the TIPS-pentacene which is much more soluble and stable than its precursor. For instance, replacing the sp^2 carbon atoms with nitrogen may give rise to electron-transporting capabilities to a material. This approach is exploited in the work of Liu and coworkers where they develop a new series of pentacene derivatives [115]. LUMO and HOMO suffered also differences compared with its closest parent (TIPS-pentacene) when their energies shifted as a result of the location of the substitution and the number of substituent atoms. An overall lowering effect of the energy levels of the frontier orbital molecular orbitals appears when the nitrogen is introduced either in the periphery or in the centre of the core. Surprisingly, inserting N atoms in the 2nd and 4th rings of the pentacene framework has a more significant energy level lowering effect compared to a modification to the 1st and 5th rings [110]. Another striking discovery was that for chlorinated compounds, the LUMO levels are lower in energy than their fluorinated counterparts, even though Cl is less electronegative than F. This phenomenon is attributed to the conjugation effects from the Cl empty 3d

orbitals [115]. What their findings highlight is that all the N-heteropentacenes display similar HOMO-LUMO gaps, but the LUMO and HOMO positions are gradually lowered by incorporating more nitrogen atoms, which is why the energy gaps of all the molecules remain nearly unchanged. Moreover, with this kind of substitutions, the photostability, as well as the thermostability found was superior to those of TIPS-pentacene as well as pentacene. Thus inclusion of nitrogen and halogen into the conjugated core delivers more robustness to the semiconducting material. However, how the various intermolecular interactions are affected by the replacement of C atoms in the pentacene backbone with N atoms is still not fully understood.

Successful organic semiconducting materials should combine solid-state emission and charge transport properties together if organic light emission transistors (OLET) are to be realised. This remains a big challenge because of the contradicting design principles of solid-state emissive materials and charge transport materials. Solid-state emission may be affected by aggregation quenching, but this can be overcome by the addition of bulky side-chains to suppress close packing, but on the other hand, efficient charge transport is enhanced when planar structures form a dense π-stacking. So not surprisingly, acenes, which possess a planar skeleton for dense molecular packing and linearly extended π-conjugation for efficient intermolecular overlap, have been widely studied in the field of organic optoelectronics. As an example, anthracene exhibits both features; light emission and charge transport. It has a fluorescence quantum yield of 64% and a mobility of 0.02 $cm^2V^{-1}s^{-1}$ at 170 K for its single crystals [118].

After the initial rapid evolution of the organic semiconductors, it was clear that there were two leading organic semiconductor representatives: pentacene and oligo/polythiophenes. It was just a matter of time to combine those two structural classes into one molecule. Inserting thiophene units into the acene backbone resulted in ladder-type thiophene-containing π-conjugated molecules, namely the *thienoacenes*.

5.1.1 Benzothieno[3,2-b]benzothiophene emergence

Among the most famous and widely explored organic semiconductors, thienoacene-based derivatives were and still are of particular interest because they exhibit high mobilities coupled with excellent air stability. Thienoacenes are linearly fused thiophene rings, a molecular structure which has been widely studied as an organic semiconductor, in particular for organic field-effect transistors (OFETs) in the last decade [4, 21, 113, 119–122]. Thienoacene derivatives possess highly delocalised π-electrons and low-lying highest occupied molecular orbital (HOMO) energy level, which contributes to their outstanding charge transport and air stability. Their large intermolecular orbital overlap is promoted by the nonbonded sulfur–sulfur and $\pi - \pi$ intermolecular interactions. In this

thienoacene family of compounds, it is generally accepted that the π-extended conjugation enhances the carrier mobility. Currently, in order to make highly extended thienoacenes two approaches are used: the fused route and the oligomer route. Where in the former case the objective consists of increasing the number of π-units by linking one unit to another one so that they are sharing one C=C double bond, and in the latter, it focuses on extending the thienoacene core through the formation of a C-C bond between two adjacent π-units [122].
Among various chemical moieties for organic semiconductors, [1]benzothieno[3,2-b]benzo-thiophene (BTBT) is a strong workhorse candidate for its promising high-performance in organic field-effect transistors (OFETs). The BTBT core contains four aromatic rings fused in a linear manner like in tetracene although its closest electronic analogue is *chrysene* to which is isoelectronic. In this highly extended π-electron system, the *aromatic sextet* of the five-membered ring is completed by the sulfur atom, supplying two π electrons.
The application and synthesis of BTBT derivatives have attracted much research interest. C_n-BTBTs with alkyl substituents on both sides of BTBT core reported to be highly soluble and films made with these compounds have exhibited record high hole mobilities. Among them, Minemawari and coworkers described a solvent-antisolvent technique where mobilities were up to 31.3 $cm^2V^{-1}s^{-1}$, moreover in the work of Yuan *et al* it was reported a so-called *off-centre spin-coating method* with record high field-effect mobility up to 43 $cm^2V^{-1}s^{-1}$ for C8-BTBT although no other publication with such technique has ever appeared [5, 93]. C_N-BTBTs with mono-substituted alkyl chains showed relatively low solubility and showed mobility up to 17.2 $cm^2V^{-1}s^{-1}$ via vacuum deposition method.
Heavy chalcogen atoms such as sulfur and selenium have larger atomic orbitals and higher polarisability than their acene counterparts, so their contribution to intermolecular interaction enables effective intermolecular orbital overlap. This gives a rationale in engaging with new synthetic routes to achieve such fused oligothiophenes, Ebata and coworkers have synthesised chalcogenophene-fused aromatic sub-structures, such as benzo[1,2-b:4,5-b']dichalcogenophenes, naphtho[1,8-bc:5,4-b'c']dithiophenes, [1]benzochalcogenopheno[3,2-b] and 2,7-dipheneyl[1]benzothieno[3,2-b][1]benzothiophene (DPH-BTBT) [113] which showed a superior stability performance under ambient conditions (≈ 250days). Our focus is on its BTBT core, which is also the main core for our target molecules. [1]benzothieno[3,2-b] [1]benzothiophene (BTBT) core contains four aromatic rings fused in a linear manner like tetracene does yet its electronic structure does not resemble it.

In the review article by Takimiya and coworkers [120] the most commonly encountered thienoacene derivatives containing more than two thiophene rings are

classified. These are divided into four broad classes, which mainly accounts for the location of the thiophene units within the molecule, and whether they are placed next to each other or separated by other rings. Among the many interesting results from their work, a key message would be that the sulfur atoms arrangement (having larger atomic radii) do influence intermolecular orbital overlap. This was attributed to the different enhancement on the intermolecular contacts induced by the sulfur. Moreover, the authors pointed out an experiment where a striking spectral shift had taken place when exciting two isomers of diphenyl-naphthodithiophenes (DPh-NDT); the *anti–isomer* –where the sulfur atoms seat on opposing sides of the molecule, and the *syn–isomer* where the atoms are placed on the same side of the molecule was the sole responsible for the shift.

When the sulphur atoms sat on opposite sides of the long backbone the spectrum redshifted 30 nm compared with the case for the *syn–isomers* which contain sulfur atoms on the same side of the molecular periphery, see figure below. They rationalise such observation with symmetry arguments and its consequential extension of the delocalised π-electrons; the centrosymmetric anti–isomers are delocalised over a wider range, whereas the axisymmetric *syn–isomers* are more localised between two neighbouring molecules. They conclude stating that their electronic structures differ significantly, even if it is true that most if not all of the thienoacene derivatives have many similarities in their molecular structure and packing, being the commonest the π–stacking or herringbone type. They found that the strength of the electronic coupling largely depends on the geometry of the frontier orbitals regardless of the packing structure. Both the molecular electronic structure, the frontier orbitals (mainly the HOMO) geometry and the packing structure in the solid-state are critical to determining device performance.

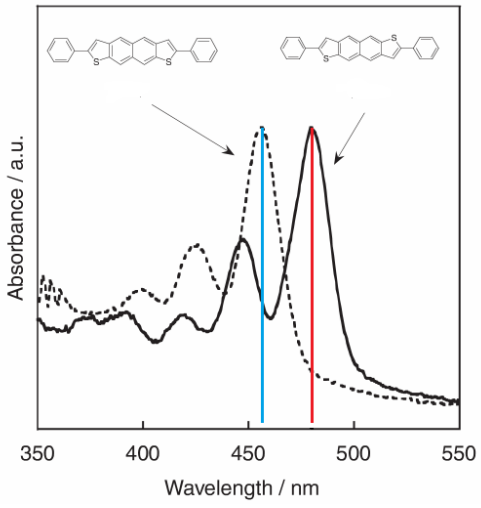

Figure 5.1. Absorption spectra of syn and anti isomers of DPh-NDT. Adapted from reference [120].

5.2 Results

It should be clear by now, that a complete description of a material necessarily must include a detailed account of the optical properties. Despite this, we have found a gap in the understanding of the optical properties of all of these materials. Nonetheless, there are few attempts to bring light to these issues, for instance in the article by Fernandez *et al* [109], authors used total electron yield (TEY) and fluorescence yield (FY) simultaneously in photoabsorption spectroscopy (NEXAFS–near-edge X-ray absorption fine structure) to probe the density of unoccupied states of tBut-BTBT. Although it is true that many of these studies briefly refer to UV-Vis spectra, as far as we are concerned the use of time-resolved techniques is completely absent. We intend to bridge this gap in this section. We have used various spectroscopic techniques to understand the photophysical properties and to further suggest design principles.

BTBT		
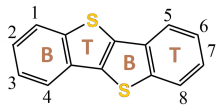		
NH_2-BTBT	NO_2-BTBT	tBut-BTBT
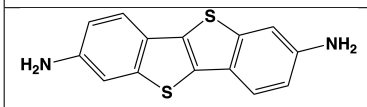	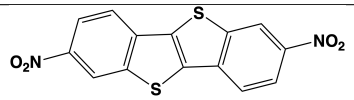	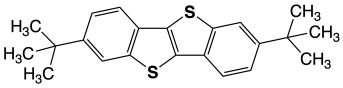
Br-BTBT	I-BTBT	C8-O-BTBT
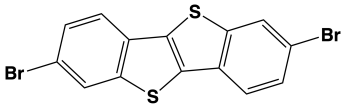	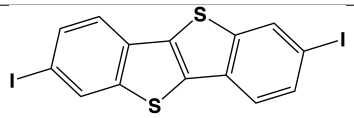	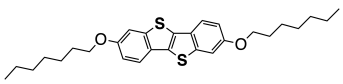
C6F13-BTBT		
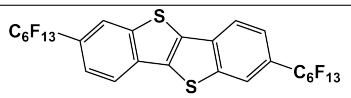		

Table 5.1. BTBT substituents.

5.2.1 2,7-diamine-[1]benzothieno[3,2-b][1]benzothiophene

UV-Vis absorption spectroscopy.

In the NH_2-BTBT molecule, a pair of amine groups are attached to the BTBT core on each side of the π-conjugated backbone. Here the NH_2 has two electrons in the non-binding orbital. Its absorption spectrum shows just one broad band

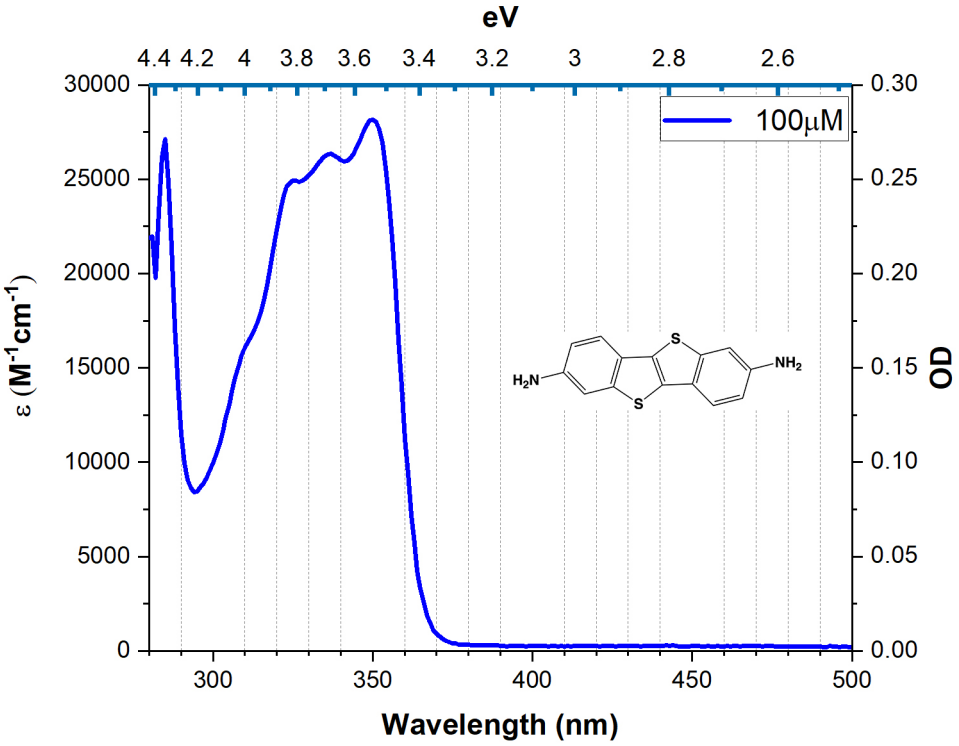

Figure 5.2. Absorption spectra for 100μM NH_2-BTBT in toluene at 293 K.

extending from 300 nm to 360 nm (4.10 eV to 3.5 eV) peaking at ~350 nm. Upon closer inspection of the spectrum, three peaks are readily observable, although there is a broad peak which using the same argument for the C8-BTBT molecule, is due to a small energetic difference between the first (S_1) and second singlet excited states (S_2). Their location are to be found in the immediate vicinity of 350 nm (3.54 eV), 338 nm (3.66 eV), and 325 nm (3.81 eV), the first peak is attributed to the first singlet excited state transition ($S_0 \rightarrow S_1$) with vibronic progression spacing close to the 120 meV of the C=C stretching mode, so we know that the $S_0 \rightarrow S_1$ optical transitions strongly couples to this mode. Finally, the featured absorption spectrum has what appears to be a slight shoulder located at 310 nm (3.99 eV). Compared with C8-BTBT we can consider the absorption spectra to be redshifted and broader. It is believed that the NH_2 group in this case further lowers the LUMO level with the consequential lower energy of the optical band-gap.

Photoluminescence

The fluorescence emission spectra of the NH_2-BTBT compound at 293 K are depicted in figure 5.3. On this graph, we see the photoluminescence for various excitation wavelengths, with just one emission band extending from 350 nm to 420 nm (3.54 - 2.95 eV) with a broad emission tail. In this case, a first

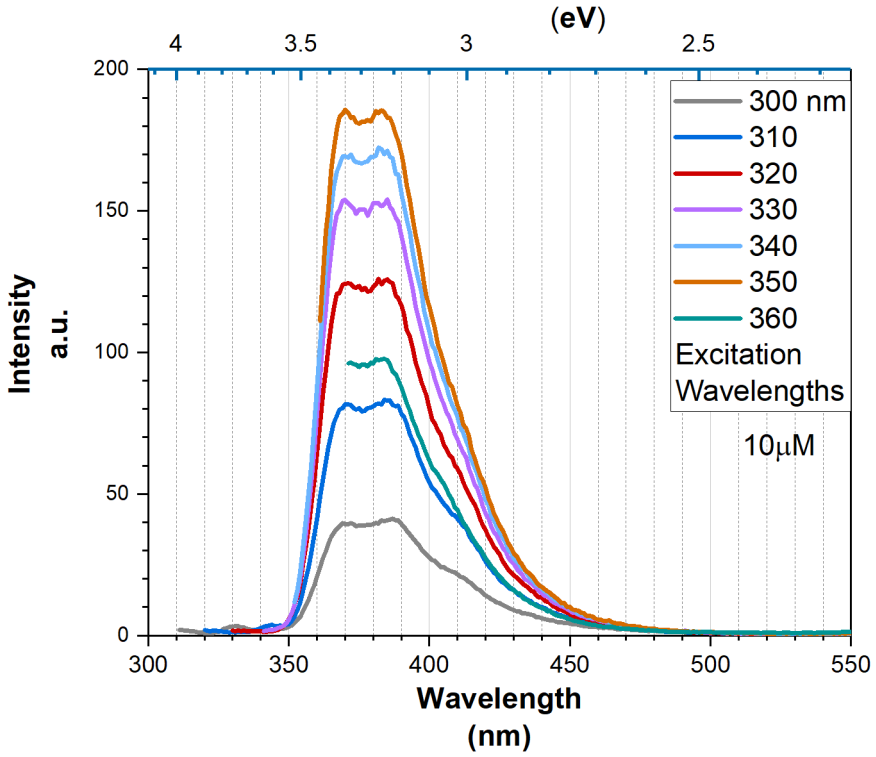

Figure 5.3. Photoluminescence spectra of 10 μM of NH_2-BTBT molecule in toluene, for various excitation wavelengths.

thing to notice is that the maximum of emission is reached when the excitation wavelength corresponds to the maximum of the absorption spectrum, as should be expected. Due to there being no excitation wavelength dependence, we can conclude that the emission spectrum is caused only by one emissive species corresponding to the transition of first excited singlet state to the ground state ($S_1 \rightarrow S_0$). The location of the emission band is centred at 380 nm (3.26 eV), corresponding to a Stokes shift of 0.28 eV. Upon closer inspection, we note that the spectrum is well described by a Franck-Condon progression and a slight red-shifted intensity in the region of 410 - 420 nm, probably caused by impurities or a small fraction of aggregates.

In figure 5.4 we can compare the normalised absorption and emission spectra in a single graph. We notice the small Stokes shift of hundreds of meV, and the region of self-absorption which is relatively small. We see that the maximal extension runs from 350 nm (3.54 eV) to 450 nm (2.75 eV). Finally, we have draw a couple of arrows to denote the excitation wavelengths used for the transient absorption experiments used for all of the target molecules.

Transient Absorption Spectroscopy

In figure 5.5 we present the data extracted from the transient absorption experiments. The experimental probe extends from 330 nm to 720 nm and

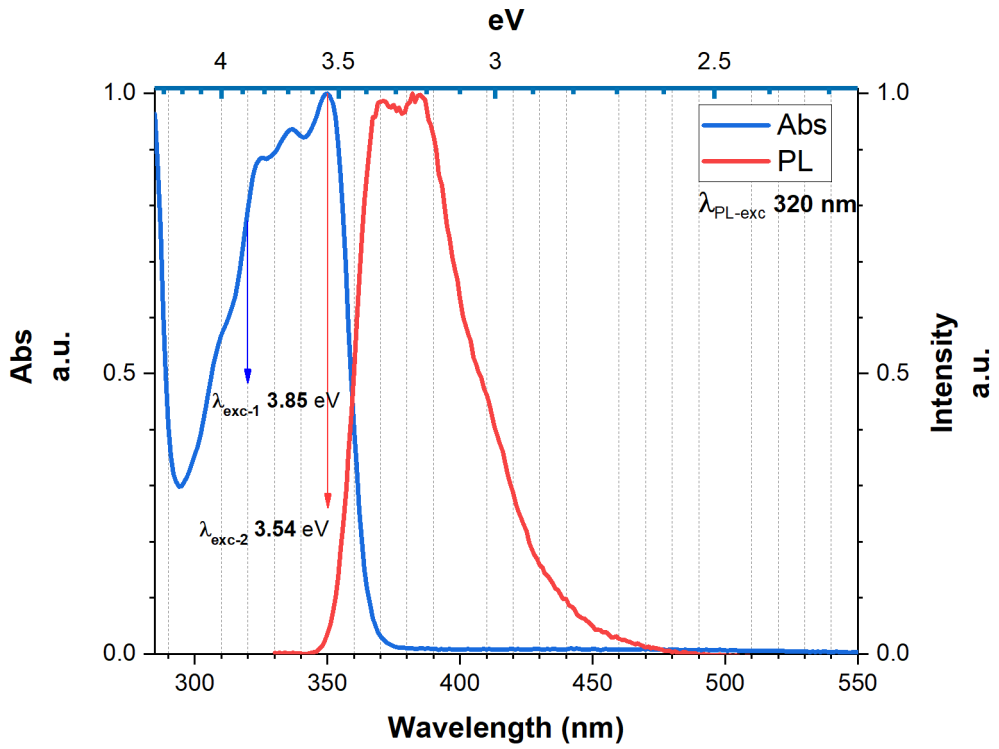

Figure 5.4. Normalised absorption (100 μM) and photoluminescence (10 μM) spectra of NH_2-BTBT in toluene solution.

from 2 ps to 6500 ns. For the 320 nm excitation wavelength we can clearly distinguish various points: First, we see that at early times there is evidence of solvent relaxation because the spectral shape at 2 ps is visibly broader than the rest of the spectra at later times. By 5 ps the $\frac{\Delta T}{T}$ signal has reached the minimum corresponding to the photoinduced absorption of the singlet manifold. By 100 ps, the signal has decreased almost half of its intensity and has slightly shifted towards the blue part of the spectrum. At 160 ps the positive signal attributed to the stimulated emission has disappeared completely and the only remaining positive signal is due to the ground state bleach that gradually is reduced over time. Looking carefully we see the spectral shape remains the same after the first 325 ps but the $\frac{\Delta T}{T}$ signal continually decreases. By 6.5 ns we are left with two bands: a positive band centred around 350 nm due to the GSB of the absorption as well as emission spectra see figure 5.4, and a negative photoinduced absorption band, centred at 490 nm (~2.52 eV).

Figure 5.5 (b) shows TA spectra for the 350 nm excitation wavelength. The transient absorption spectral shape and the overall appearance closely resembles that of panel (a) for the excitation wavelength at 320 nm. We can clearly resolve two peaks in the positive $\frac{\Delta T}{T}$ signal, corresponding to the maximum of the steady–state absorption and the photoluminescence emission maximum (*cf* figure 5.4). Comparing excitation at 320 nm and 350 nm, we observe that the stimulated emission relative to the ground state bleach is more intense with the

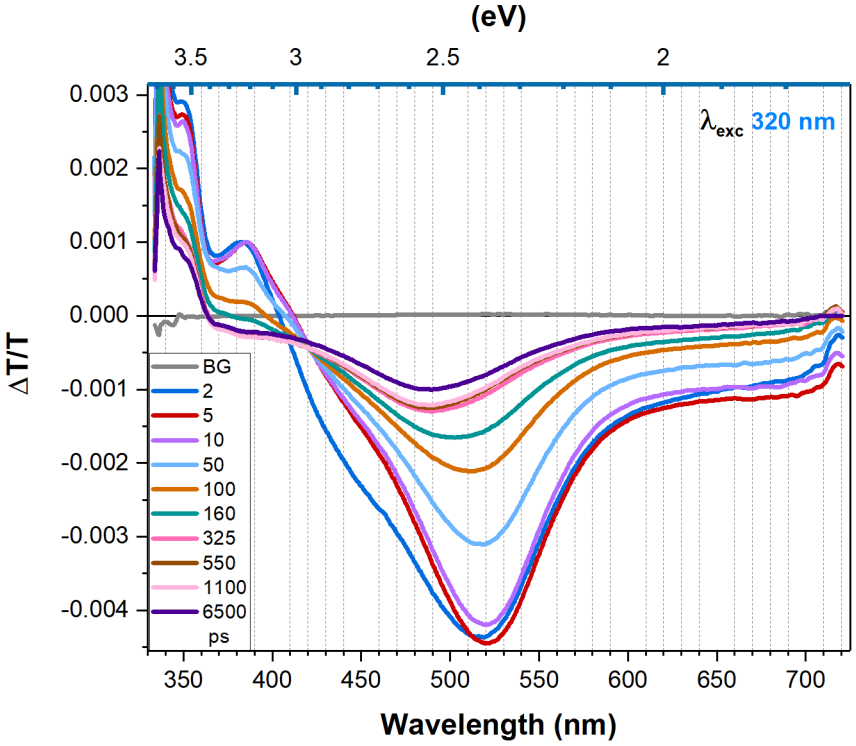

(a) TA $\lambda_{exc_1} 320nm$

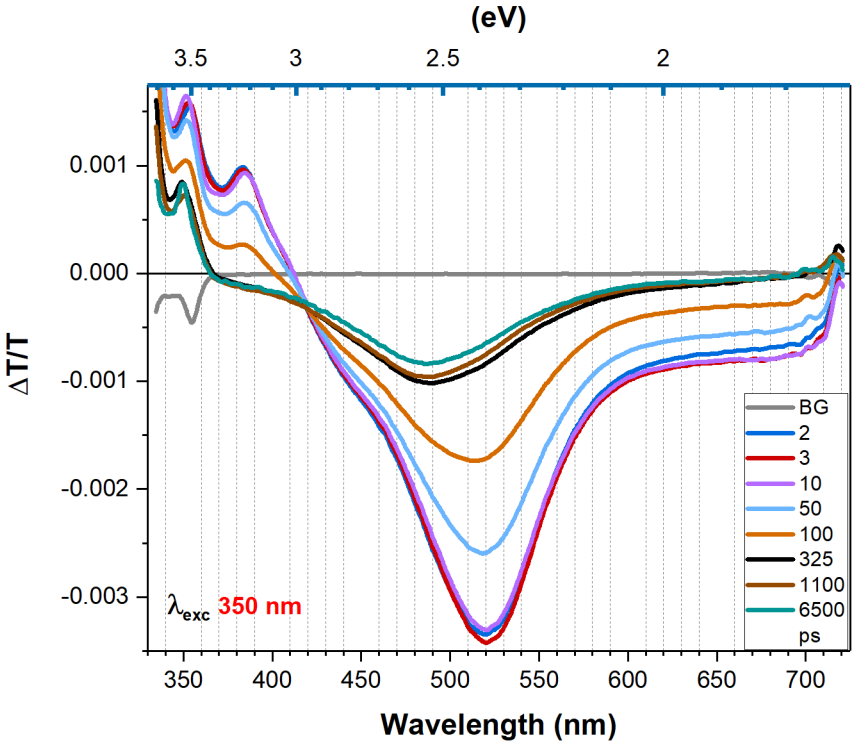

(b) TA $\lambda_{exc_2} 350nm$

Figure 5.5. Transient absorption of 100 μM of NH_2-BTBT in toluene, for the given excitation wavelengths. In the figure the spectral shape is shown for various times delays.

350 nm excitation. Likewise, the early-time (<10 ps) spectra are broader with 320 nm excitation wavelength compared with the excitation at 350 nm.
In figure 5.6 (below), we have condensed all the previous figures so the features previously discussed are clearly observed. Note that for both excitations the GSB dominates the positive feature, at both earlier and later times. Although for the 350 nm excitation wavelength the stimulated emission (SE) is more intense, which is not completely true since the $\frac{\Delta T}{T}$ signal is more intense for the 320 nm excitation wavelength.

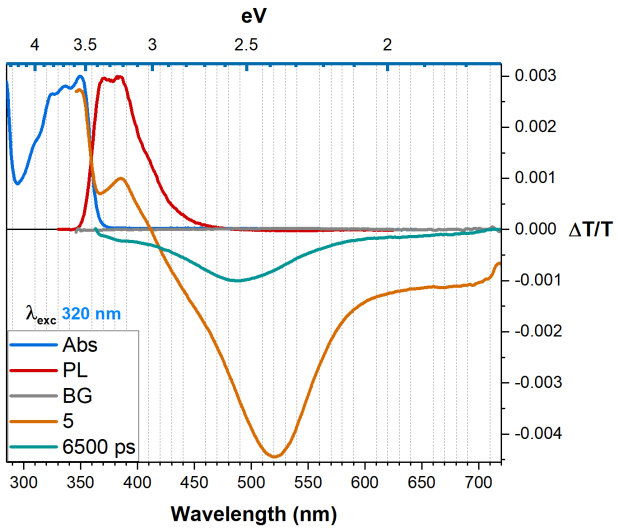

(a) TA $\lambda_{exc_1} 320nm$

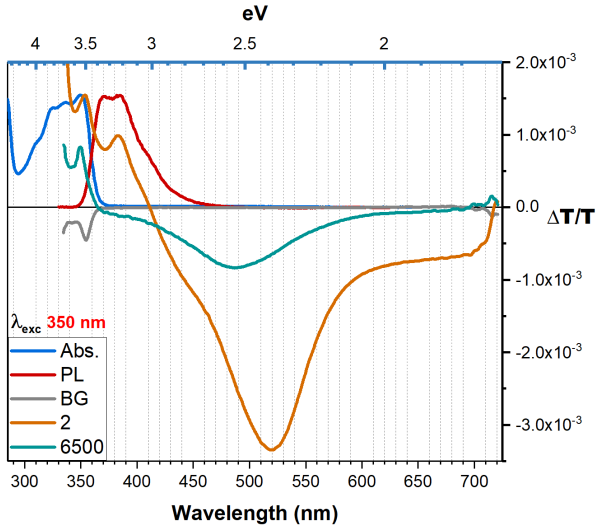

(b) TA $\lambda_{exc_2} 350nm$

Figure 5.6. Transient absorption of both excitation wavelengths, absorption and photoluminescence of NH_2-BTBT.

Finally, we propose that the NH_2-BTBT molecules undergo intersystem crossing from S_1 as well. This claim is inferred by our previous knowledge on the behaviour of the C8-BTBT. Since the spectral features although distinct are

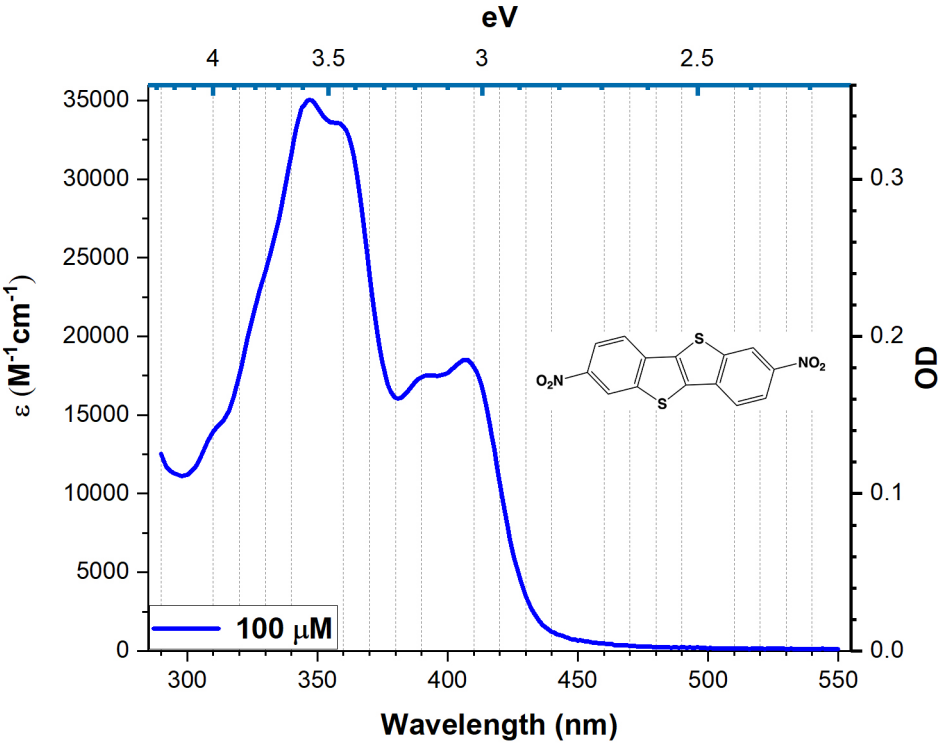

Figure 5.7. Absorption spectrum of 100μM NO_2-BTBT in toluene at room temperature (293 K).

analogous: we see that at later times there is virtually no stimulated emission, and also an isosbestic point placed at 430 nm (2.88 eV) which is located close to the one of C8-BTBT. Furthermore, the species is long-lived (> 6.5 ns) which strongly suggests that it is due exclusively to triplets. The ISC time-constant in this case is estimated to be $\tau_{\text{ISC}} \sim 100ps$.

5.2.2 2,7-dinitro-[1]benzothieno[3,2-b][1]benzothiophene

UV-Vis absorption spectroscopy.

For this molecule, a couple of nitro groups were attached to the BTBT core on each side of the π-conjugated backbone. The absorption spectrum shows one broad absorption band spreading from 310 nm to 420 nm ($\approx$ 4.0 to 2.95 eV) with two resolved peaks located at 345 nm (3.6 eV) and 410 nm (3.06 eV). At first glance, these two features look to originate from S_1 and S_2, however as we discussed further below this assignment is not entirely correct, for the low energy part of the absorption could be due to undissolved dimers. The last statement stems on the experience during sample preparation, for this material was difficult to dissolve even after heating the solution and stirring, such that

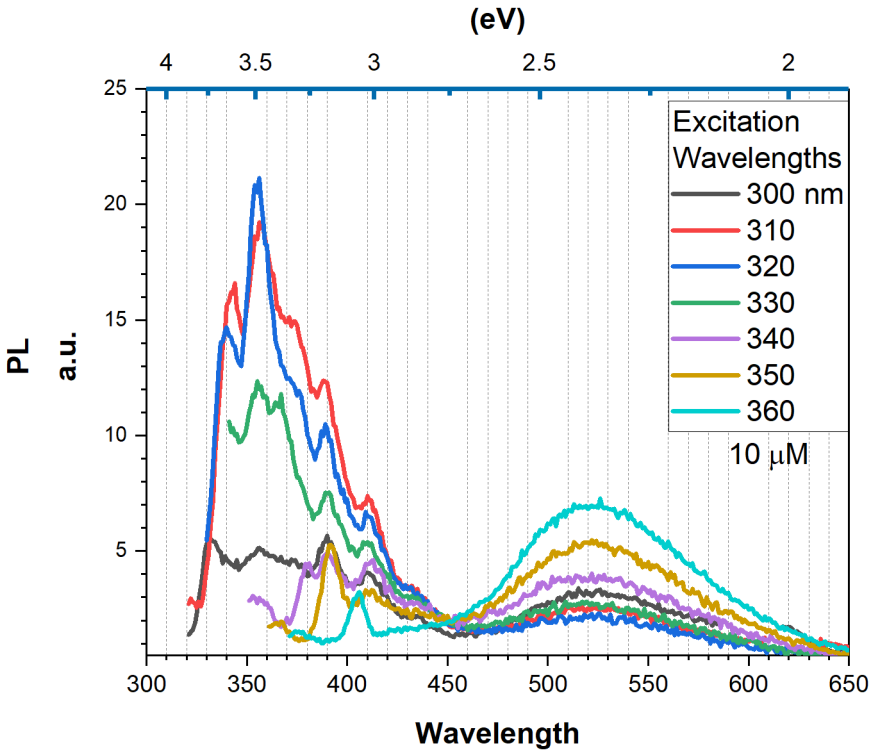

Figure 5.8. Photoluminescence spectra of 10 μM of NO_2-BTBT molecule in toluene, for various excitations wavelengths.

at even a concentration of 1 mM the solution was turbid, which indicates poor solubility.

Photoluminescence

Figure 5.8 presents the fluorescence emission spectra of the NO_2-BTBT compound at room temperature (293 K). The first thing to notice about these spectra is that the molecule has a very low PLQY which was barely visible in the fluorimeter, hence we expect that the dominating deactivation processes occur non-radiatively. Second, we observe non-Kasha-Vavilov emission when exciting above 340 nm (3.64 eV). Given the proximity of the two absorbing features, we conclude that they originate from two different populations within the sample. Excitation energies below 340 nm resulted in pronounced excimer-type emission. This is generally a result of significant intermolecular interaction and suggests a population of dimers within the sample, which is consistent with our observations of low solubility when preparing the solutions. To examine this further we studied the TA spectra, exciting above and below this excitation wavelength.

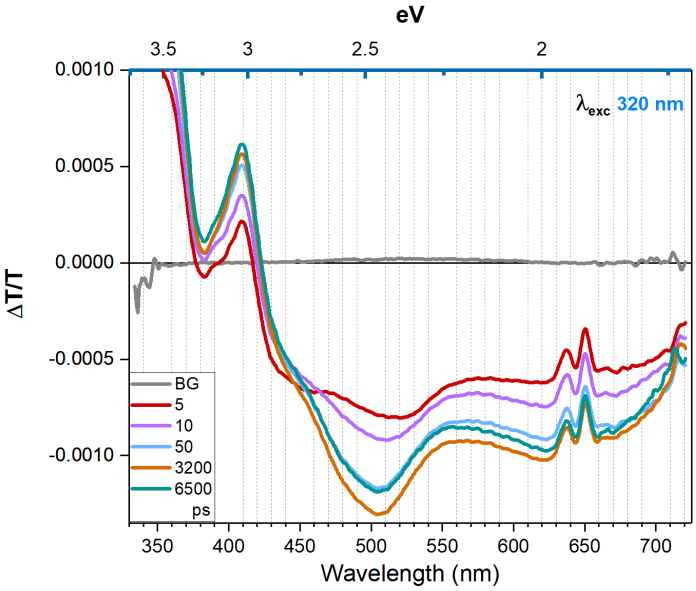

(a) TA $\lambda_{exc_1} 320nm$

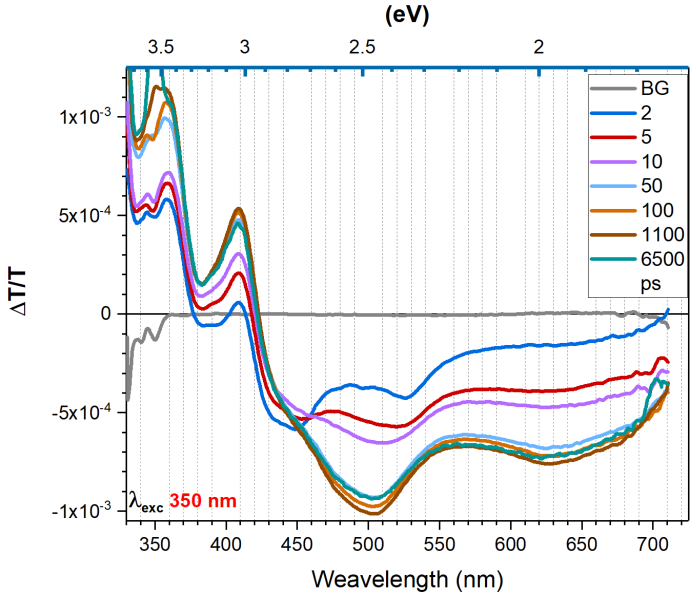

(b) TA $\lambda_{exc_2} 350nm$

Figure 5.9. Transient absorption of 100 μM of NO_2-BTBT in toluene, for the given excitation wavelengths.

Transient Absorption Spectroscopy

Figure 5.9 shows transient absorption spectra with excitation at 320 nm (a) (into the second absorption band, *i.e.* high-energy) and at 350 nm (b). In both cases, the ground state bleach appears to increase during the first nanosecond. This phenomenon is likely to be caused by the decay of a strong overlapping photoinduced absorption, which peaks towards the blue and at ∼525 nm. This feature decays to reveal the pronounced GSB and PIA peaked at ∼500 nm with a shoulder at 630 nm. Despite the difference in photoluminescence behaviour, the PIA features are similar with both 320 nm and 350 nm excitation. The main difference is the change in GSB ratio: with the 320 nm excitation the initial GSB is dominated by a feature at 345 nm (ratio $\frac{\Delta T}{T}_{345nm}/\frac{\Delta T}{T}_{410nm} \approx 6$), while excitation at 350 nm shows a much weaker 345 nm feature (ratio $\frac{\Delta T}{T}_{345nm}/\frac{\Delta T}{T}_{410nm} \approx 2$). Changes in relative GSB with excitation wavelength point to different populations within the sample, in agreement with the PL and what we have been mentioning all along. We therefore conclude that this sample is made up of monomers (absorption at ∼ 345 nm) and dimers (absorption at ∼ 410 nm). The dimers can then relax in the excited state to produce red-shifted excimer-like emission whilst the monomer shows typical fluorescence. In conclusion, the complex nature of this sample precludes the possibility of using it as a controlled model system and we therefore make no further comments on it.

5.2.3 2,7-di-tert butyl-[1]benzothieno[3,2-b]benzothiophene

UV-Vis absorption spectroscopy.

For this molecule two tert-butyl groups have been attached to the BTBT core at the 2 and 7 positions. Figure 5.10 shows a broad absorption band extending from 340 nm (∼3.6 eV) to 290 nm (∼4.3 eV) peaking at 313 nm (3.96 eV). Despite the convoluted appearance of the spectrum, four peaks are clearly resolved, located at 308 nm (4.02 eV), 313 nm (3.96 eV), 321 nm (3.86 eV) and 330 nm (3.75 eV). This molecule's absorption spectrum has a striking similarity with the shape and locations of the peaks of C8-BTBT, which perhaps is not surprising if we realise that the function of the bulky tert-butyl substituents is the same of the octyl chains in the latter, which as we mentioned in the introduction, is to aid in solubility and crystal packing. Hence, in close analogy with C8-BTBT, this spectrum is the result of two excited singlet states which are energetically close. We suggest then, that $S_0 \rightarrow S_1$ transition is to be found in 330 nm (3.75 eV) and the $S_0 \rightarrow S_2$ transition to the maximum peak of the

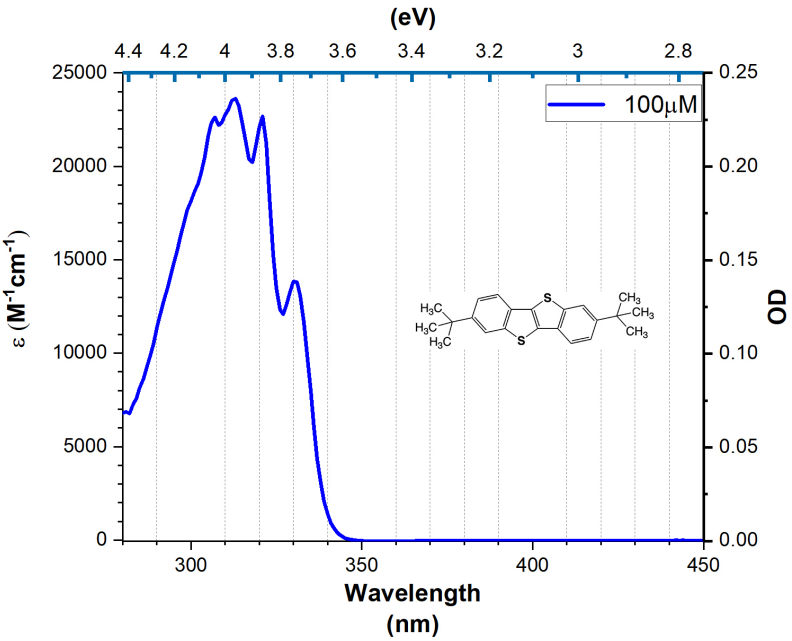

Figure 5.10. Absorption spectra of 100μM tBut-BTBT in toluene at 293 K.

absorption located at 313 nm (3.96 eV).

Photoluminescence

The fluorescence emission spectra of the tBut-BTBT compound in toluene at room temperature are depicted in figure 5.11. From the figure we observe one emission band ranging from 330 nm (3.75 eV) to 440 nm (2.81 eV) with two readily identifiable peaks; located at 341 nm (3.63 eV) and the maximum peak of emission at 356 nm (∼3.5 eV). Upon closer inspection we can also see a shoulder at 375 nm (∼3.3 eV). Finally we note that for the 340 nm excitation the emission has reduced its value significantly.

In figure 5.12 we compare absorption and emission spectra of But-BTBT normalised to the maximum value measured. In this tBut-BTBT molecule the similarities with the steady-state spectroscopy of C8-BTBT are truly remarkable; shape and location of absorption and emission peaks, as well as the extension of the emission tail. We notice an overlapping region of absorption and emission around 330-340 nm, which should be reflected as a positive signal in the transient absorption (TA). Finally, from the plot we note a small Stokes shift which indicates the rigidity of the molecular structure of tBut-BTBT.

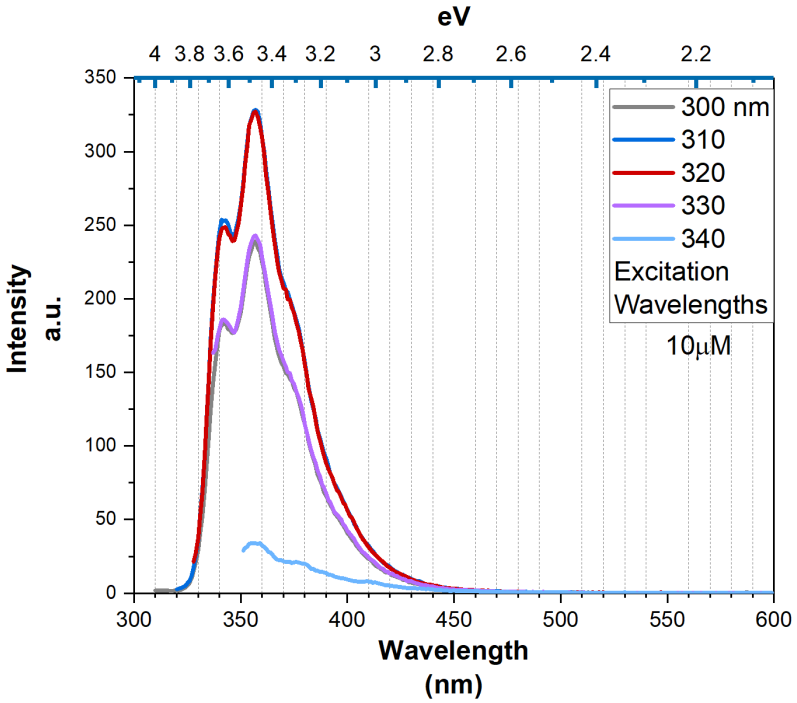

Figure 5.11. Photoluminescence spectra of 10 μM of tBut-BTBT in toluene, at various excitation wavelengths.

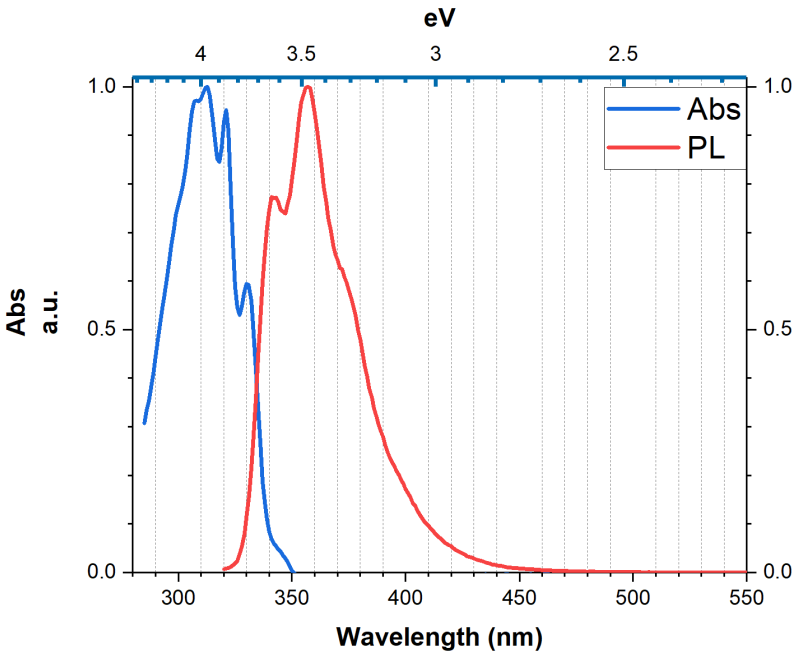

Figure 5.12. Normalised absorption (100 μM) and photoluminescence (10 μM) solution spectra of tBut-BTBT in toluene.

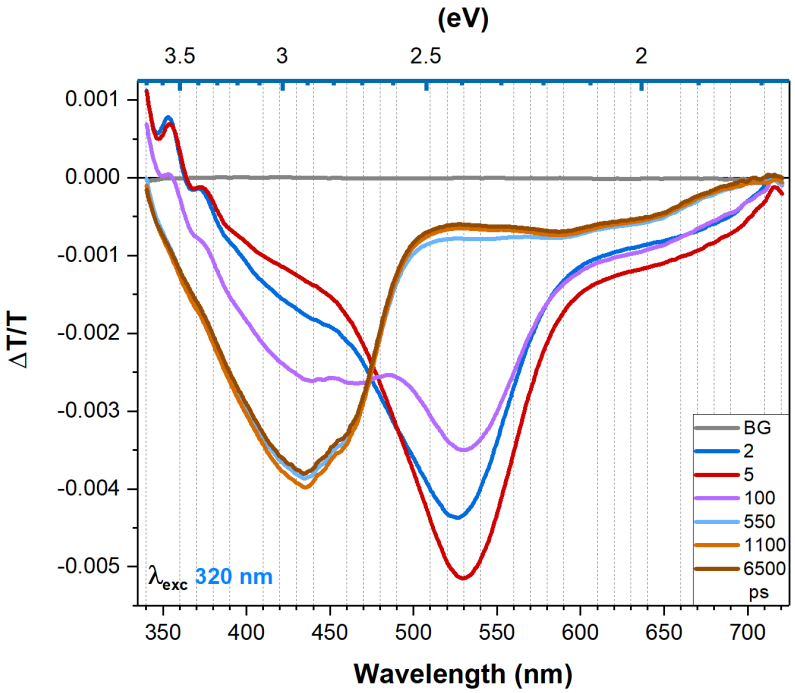

(a) TA spectrum at $\lambda_{exc}320nm$

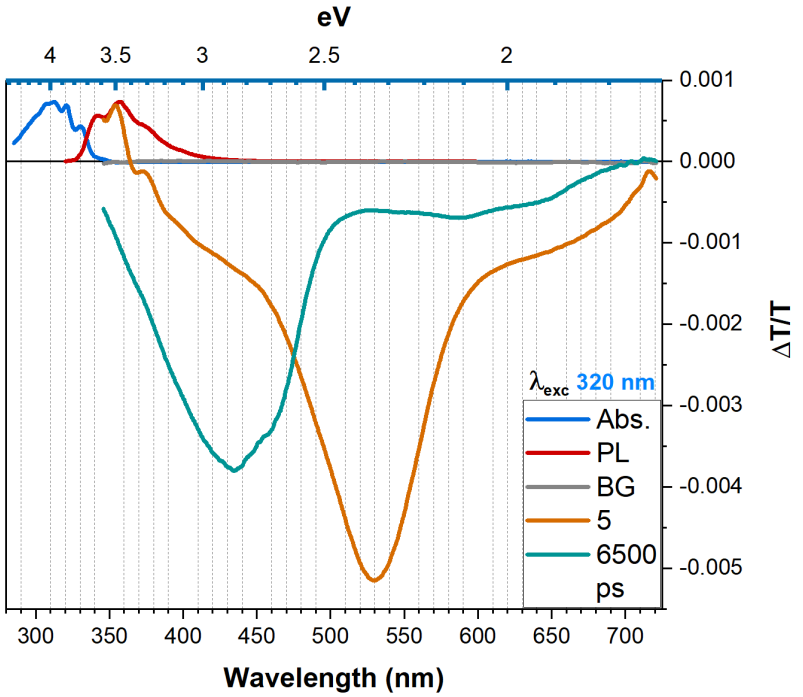

(b) Transient absorption, absorption and photoluminescence of tBut-BTBT.

Figure 5.13. Spectroscopical signaturest of But-BTBT in solution.

Transient Absorption Spectroscopy

In figure 5.13 (a) we present the data extracted from the transient absorption experiment at the given excitation wavelength. The parallelism with C8-BTBT is further increased when we observe the overall behaviour of the transient absorption spectra: for instance, we see that the positive $\frac{\Delta T}{T}$ should be associated with stimulated emission since it appearance originate in the same region of the photoluminescence spectrum, moreover we note that by the time the TA experiment reached the first 100 ps this signal has disappeared almost completely in agreement with what we showed for C8-BTBT. Additionally, we can identify an isosbestic point located at 475 nm suggesting an interconversion of species, moreover we note two photoinduced absorption (PIA) bands with clearly two distinct time formations; the earliest peaking at 530 nm (2.33 eV) which incidentally is almost identical with the one for the C8-BTBT molecule, and the longer lived PIA band peaking at 435 nm (2.85 eV) also in the same region of C8-BTBT. Accordingly, we assign the former PIA to the singlet excited state absorption and the latter PIA caused by triplet state absorption.

5.2.4 2,7-dibromine-[1]benzothieno[3,2-b][1]benzothiophene

A natural way for probing spin–orbit–coupling is increasing the atomic number of some part of the chromophore. In this section, we have probed the effects on the optical properties of the BTBT core with bromine and iodine substituents at the 2 and 7 positions (see table 5.1). Also, we have studied what happens when we substitute at the same positions: tert-butyl, NH_2, NO_2, C8-O and when we take a hexyl chain and replaced their hydrogen atoms by means of fluorination.

UV-Vis absorption spectroscopy.

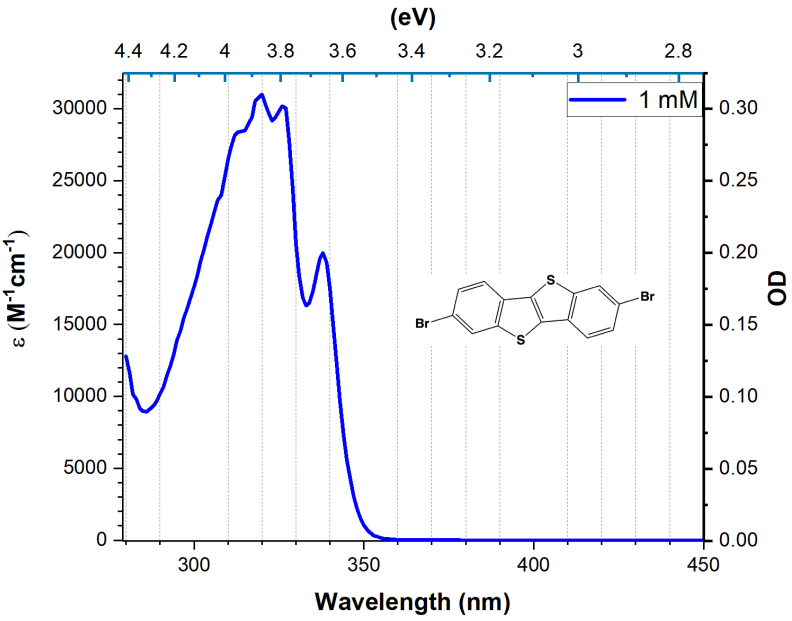

Figure 5.14. Absorption spectra for 1 mM Br-BTBT in toluene.

Figure 5.14 shows the absorption spectrum of Br-BTBT. We observe from the spectra that it has an absorption onset roughly starting at 350 nm (3.54 eV) and finishing at 290 nm (4.27 eV).

The spectra for Br-BTBT looks similar to C8-BTBT, so we infer in close analogy to C8-BTBT that this is likely to have the S_1 and S_2 so close in energy. We cannot tell apart the spectral features because they overlap and the resultant spectrum is devoid of simple vibronic structure. Nonetheless four faint peaks are resolved, which is the same number we had for C8-BTBT and BTBT, although their location has changed to 338 nm (3.66 eV), 327 nm (3.79 eV), 320 nm (3.87 eV) and 313 nm (3.95 eV).

Photoluminescence

Figure 5.15 depicts the fluorescence emission spectra of the Br-BTBT compound at room temperature. On the figure we see only one emissive peak which does not seem to be excitation dependent, ruling out excimer emission and aggregation induced emission, which further implies there is only one emitting species. The emission maxima are located at 365 nm ($\sim 3.4eV$), and as expected from the absorption spectrum the excitation wavelength at 320 nm produces the most intense signal. Although the spectral shape does not seem to change much with excitation, we can see some processes taking place around 380 nm (3.26 eV) and like C8-BTBT it has a long tail of emission extending up to 500 nm

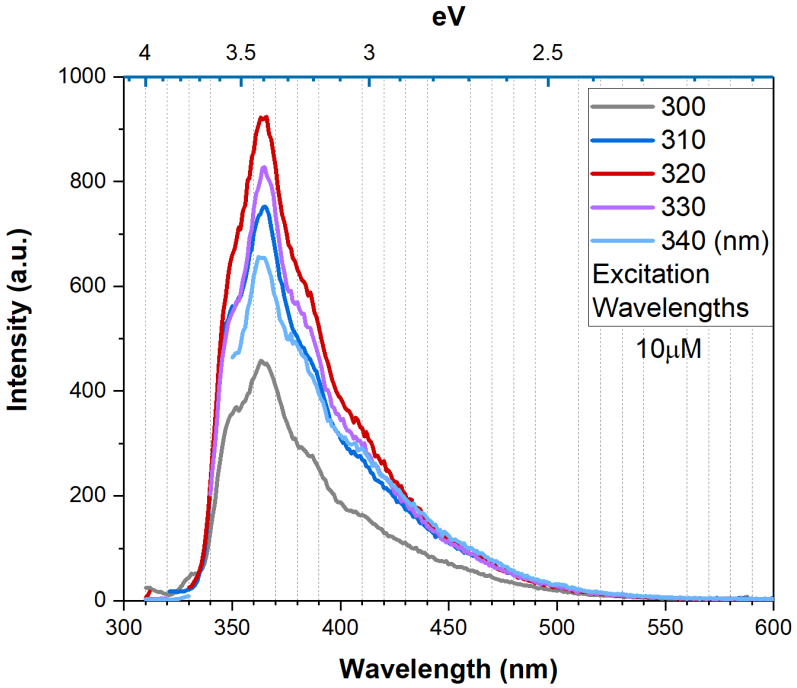

Figure 5.15. Photoluminescence spectra of 10 μM of Br-BTBT molecule in toluene, for various the excitation wavelengths shown.

(2.48 eV).

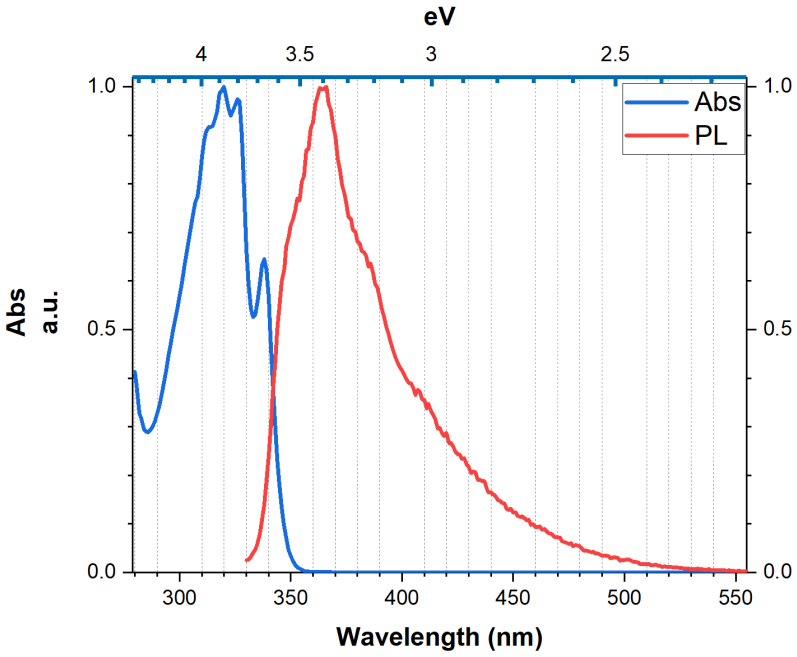

Figure 5.16. Normalised absorption (1 mM) and photoluminescence (10 μM) spectra of Br-BTBT in toluene solution.

When plotting together emission and absorption we quickly realise that

between 350 nm (3.54 eV) and 330 nm (3.75 eV) there is an overlapping region of absorption and emission. Finally, from the steady-state experiments we can see that given the fact that the 0-0 transition is not clearly identifiable, a rough estimate between the maxima of absorption and emission gives a Stokes shift of 0.5 eV. This value is considered to be relatively large, suggesting a significant effect of solvent relaxation taking place.

Transient Absorption Spectroscopy

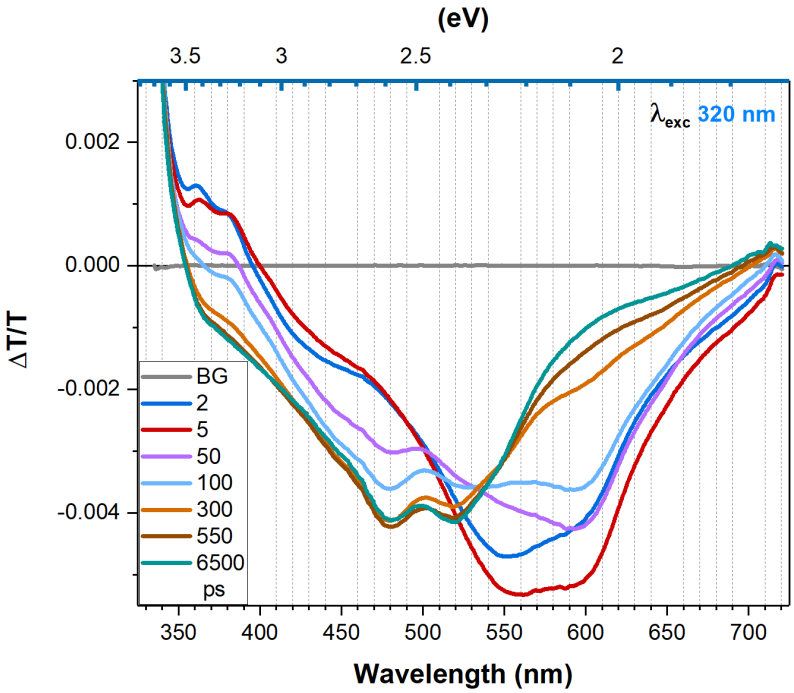

(a) TA $\lambda_{exc_1} 320nm$

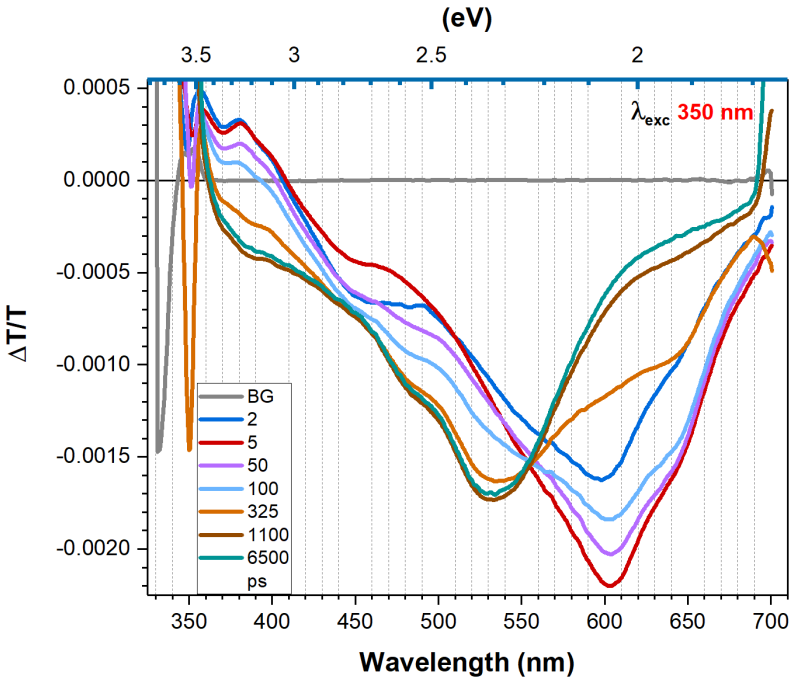

(b) TA $\lambda_{exc_2} 350nm$

Figure 5.17. Transient absorption spectra of 100 μM solution of BR-BTBT in toluene. Figure shows different times delays.

From figure 5.17 we see a defined positive $\frac{\Delta T}{T}$ signal from 400 nm to 350 nm ($\sim$ 3.10 - 3.54 eV). From figure 5.15 it should be clear that the origin of this

feature is due to stimulated emission from the singlet state, which looks to live less than 200 ps. On the redder part of the spectra we identify a negative $\frac{\Delta T}{T}$ signal that reaches a minimum value within the first 5 ps of the experiment. We assign this peak to be a photo-induced absorption (PIA) band of singlet manifold nature, in accordance with what was previously found for C8-BTBT. Upon a more detailed look, we note how this PIA band decreases more rapidly closer to 550 nm (2.25 eV) than for the region close to 600 nm (2.06 eV). By the first 100 ps the initial PIA has broadened and shifted to the blue region and by 300 ps the signal has decreased almost completely. Moreover, we distinguish that the initial PIA has shifted to the 500 nm (2.48 eV) and remains unchanged from 500 ps. Finally, we observe that around 510-530 nm (2.43 - 2.33 eV) there is a feature thought to be an isosbestic point is smeared out.

Panel (*b*) of figure 5.17, presents the transient absorption spectra with 350 nm band-edge excitation wavelength. At first glance, we note the pump scatter is considerably higher at this excitation for in the immediate vicinity of 350 nm (3.54 eV) and 700 nm (1.77 eV) $\frac{\Delta T}{T}$ signal appears to oscillate between positive and negative values. Again, we see a positive $\frac{\Delta T}{T}$ signal from 2 ps ranging from 410 nm (3.02 eV) down to 350 nm (3.54 eV). Nonetheless, it seems to have slightly longer-lived stimulated emission, which by the time of 325 ps it has completely disappeared. The photoinduced absorption band located at 600 nm (2.06 eV) looks sharper and better defined and compared to the 320 nm excitation decreases with similar spectral shape the first 100 ps, for at 325 ps the $\frac{\Delta T}{T}$ peak signal shifts abruptly from 600 nm (2.06 eV) to 530 nm (2.33 eV). From 325 ps onwards the spectral shape remains unchanged and almost without loss of intensity by the end of the experiment at 6.5 ns. From comparison drawn from the 320 nm excitation wavelength we notice an evident redshift of the singlet band from the peak centred around 575 nm (2.15 eV) for λ_{exc_1} to 600 nm (2.06 eV) for λ_{exc_2}. Furthermore the second longer lived PIA has a single peak at 530 nm (2.33 eV) for λ_{exc_2} in contrast with the previous excitation which had two; located at 480 nm (2.58 eV) and 520 nm (2.38 eV).

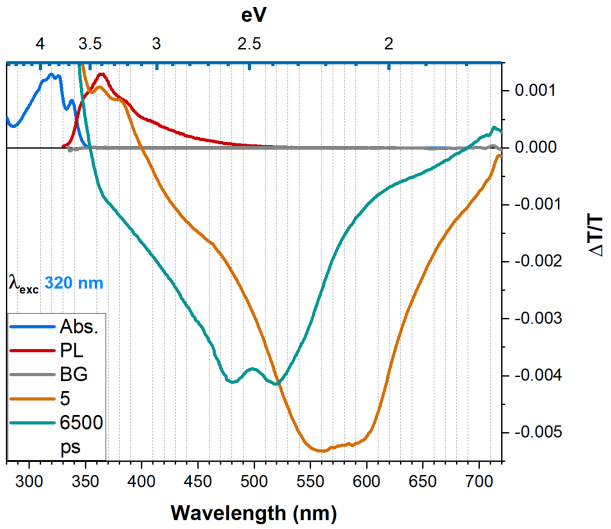

(a) TA $\lambda_{exc_1} 320\,nm$

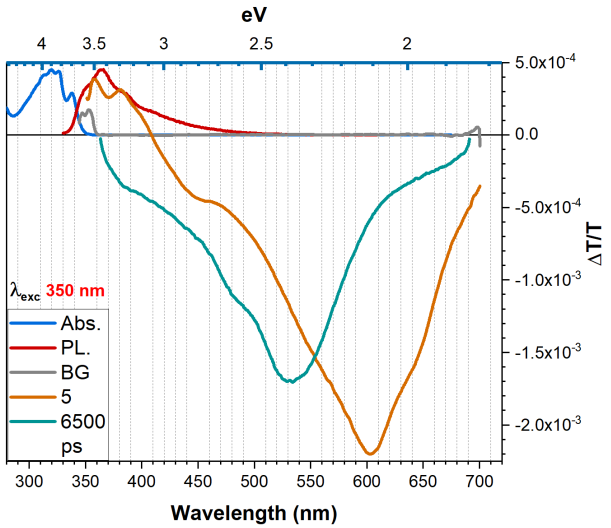

(b) TA $\lambda_{exc_2} 350\,nm$

Figure 5.18. Transient absorption at both excitation wavelengths, with absorption and photoluminescence of Br-BTBT.

Despite the fact that there is a certain excitation wavelength dependence, the behaviour is quite analogous to that of C8-BTBT - a shorter lived excited state evolving to another longer lived excited state. This means, that our assignment of the excited states will be the same for both excitations $\lambda_{exc_1} = 320\,nm$ and $\lambda_{exc_1} = 350\,nm$: a photoinduced absorption band that is close to 600 nm (2.33 eV) due to excited singlet state absorption, and another PIA band located around 520 nm (2.38 eV) that corresponds to triplet state absorption.

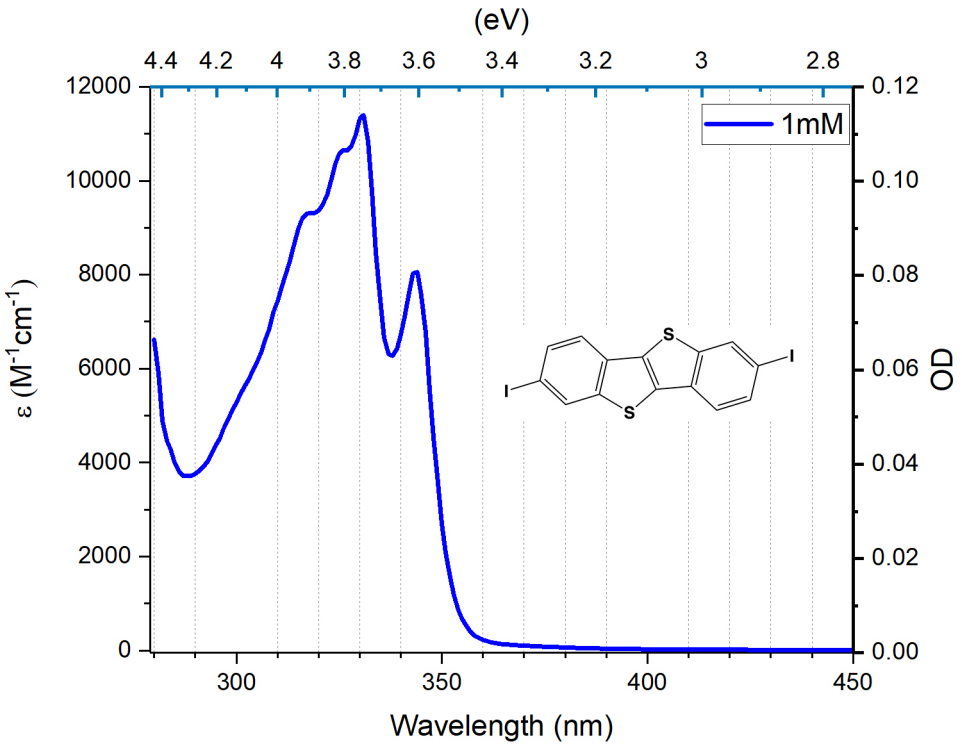

Figure 5.19. Absorption spectra for 1 mM I-BTBT in toluene.

5.2.5 2,7-diiodo-[1]benzothieno[3,2-b][1]benzothiophene

UV-Vis absorption spectroscopy.

Figure 5.19 provides an insight into the electronic structure of the 2,7 di-iodine substitution, by means of its absorption band extending from roughly at 350 nm (3.54 eV) and finishing at 290 nm (4.27 eV). The sharpness of the peaks is probably the most noticeable aspect of the spectrum in figure 5.19, nonetheless, it is still a broad absorption band. The wavelength for maximum absorption is to be placed at 330 nm (∼3.75 eV), followed by smaller shoulder peaks at 326 nm ($\sim 3.8eV$), another at 318 nm (3.91 eV), and the reddest first peak right at the onset at 345 nm (∼3.6 eV). Next to note, is that the absorption coefficient value is almost half that of the brominated compound. We conclude that the broad spectrum is once again due to two close singlet states that mix effectively.

Photoluminescence

Figure 5.20 presents the fluorescence emission spectra of the I-BTBT compound at room temperature. From the figure we immediately note a sharp contrast with the bromine substituents, the PLQY is very low, suggesting that fluorescence does not compete effectively with non-radiative deactivation processes. In this case, the spectra are so convoluted that is not possible to make further

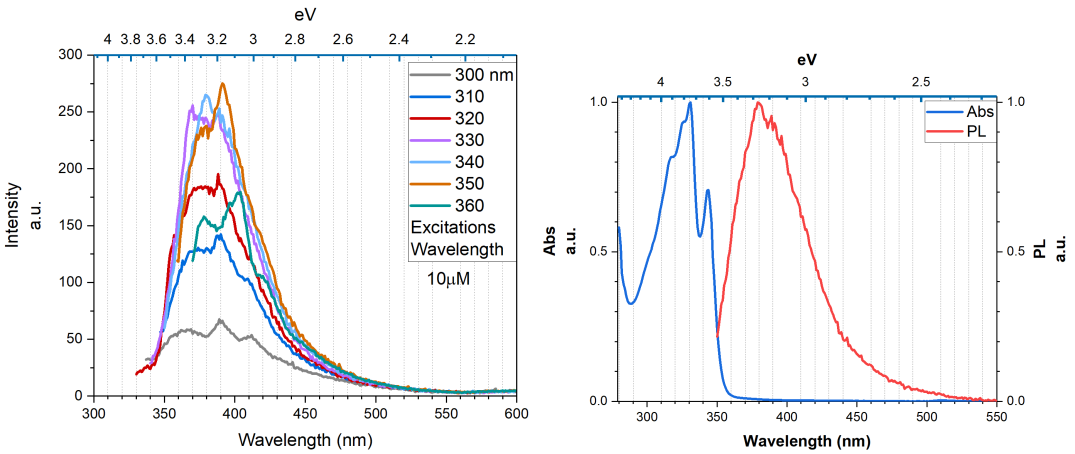

(a) PL of 10 μM solution of I-BTBT at various excitation wavelengths.

(b) Normalised absorption and PL spectra at 320 nm excitation

Figure 5.20. Photoluminescence and absorption spectra of I-BTBT

remarks, although we can definitely tell it doesn't seem to present excitation dependence nor excimer emission.

When plotting together emission and absorption we quickly realise that between 350 nm (3.54 eV) and 330 nm (3.75 eV) there is an overlapping region of absorption and emission. Finally, from the steady-state experiments we can see that given the fact that the 0-0 transition is not clearly identifiable, a rough estimate between the maxima of absorption and emission gives a Stokes shift of 0.5 eV. This value is considered to be relatively large, suggesting a significant effect of solvent relaxation taking place.

Transient Absorption Spectroscopy

Figure 5.21 presents the TA spectra of I-BTBT. For both excitation wavelengths we see a defined positive $\frac{\Delta T}{T}$ signal ranging from 420 nm to 350 nm ($\sim$ 2.95 - 3.54 eV). From figure 5.20 it should be clear that the origin of this feature is due to stimulated emission from the singlet state, such $\frac{\Delta T}{T}$ signal lives more than 300 ps. On the other hand, around 600 nm (2.06 eV) in the redder part of the spectra we identify a negative $\frac{\Delta T}{T}$ signal that reaches a minimum value in the first 5 ps. We associate this $\frac{\Delta T}{T}$ signal peak to a photoinduced absorption (PIA) to a singlet manifold. Upon closer inspection of the TA spectra we can clearly see a strong resemblance for the same excitation wavelength to the brominated compound, which means that at the 550 ps there is no significant $\frac{\Delta T}{T}$ signal left from the 600 nm peak. There is also a new PIA with two faint peaks at 510 and 550 nm (2.43, 2.25 eV) which remains unchanged from this time and by 6500 ps does not decrease in intensity. Finally, we note at around 540-550 nm (2.29

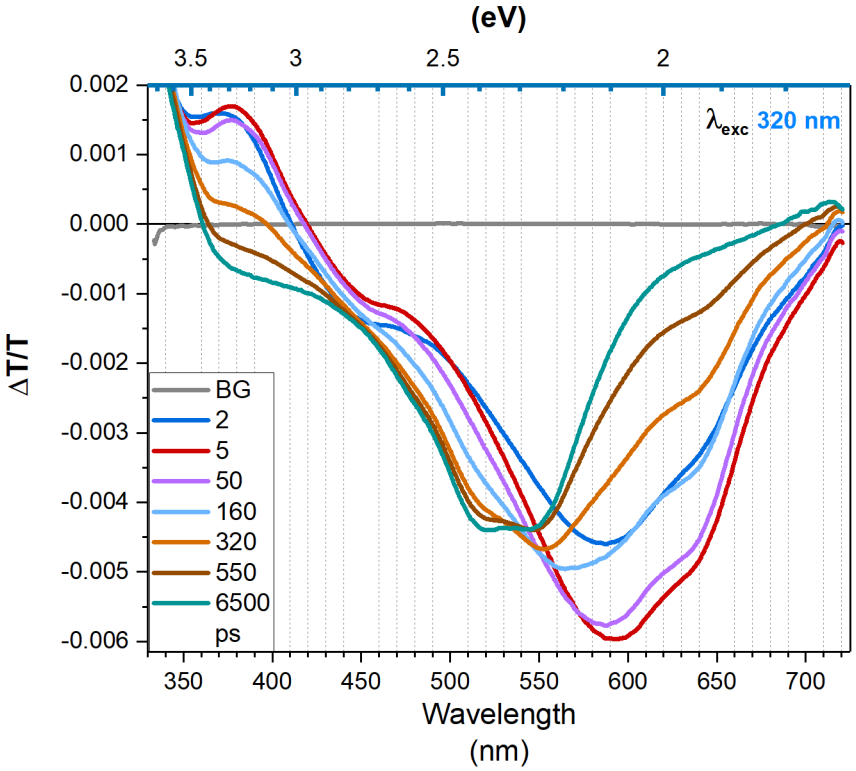

(a) TA $\lambda_{exc_1} 320nm$

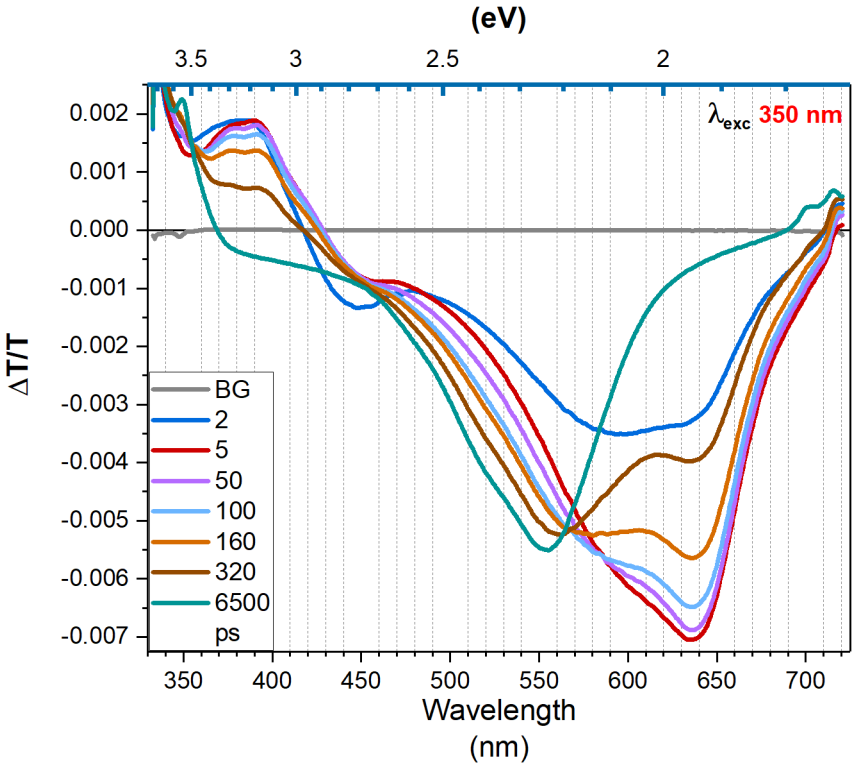

(b) TA $\lambda_{exc_2} 350nm$

Figure 5.21. Transient absorption spectra of 100 μM solution of I-BTBT in toluene. Each panel shows different times delays.

- 2.25 eV) there is a feature that could be an isosbestic point.

Panel *b* of figure 5.21, presents the transient absorption spectra of the 350 nm excitation wavelength. At first glance we that the similarities with the brominated compounds persist for this excitation wavelength as well. Again, we see a positive $\frac{\Delta T}{T}$ signal from 2 ps ranging from 440 nm (2.81 eV) down to 350 nm (3.54 eV). Comparing with previous excitation we should identify the value of the $\frac{\Delta T}{T}$ signal is almost the same. Nonetheless, it seems to have slightly longer-lived stimulated emission. Although both excitations are similar, there is a redshift of the $\frac{\Delta T}{T}$ negative peak from 600 nm (2.06 eV) to 650 nm (1.90 eV). The photoinduced absorption band located at 650 nm (1.9 eV) looks sharper and better defined compared to the 320 nm excitation. It can be seen that the way it decays is not quite like the previous excitation, for by 160 ps there are clearly two peaks where for 320 nm excitation they do not exist. Finally, we note that the second PIA which is longer lived, has just one sharper peak at 550 nm (2.25 eV) in contrast with the previous 320 nm excitation which had two.

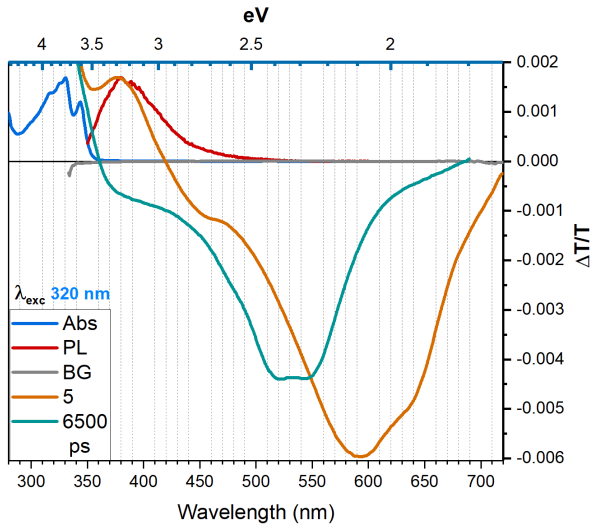

(a) TA $\lambda_{exc_1} 320\,nm$

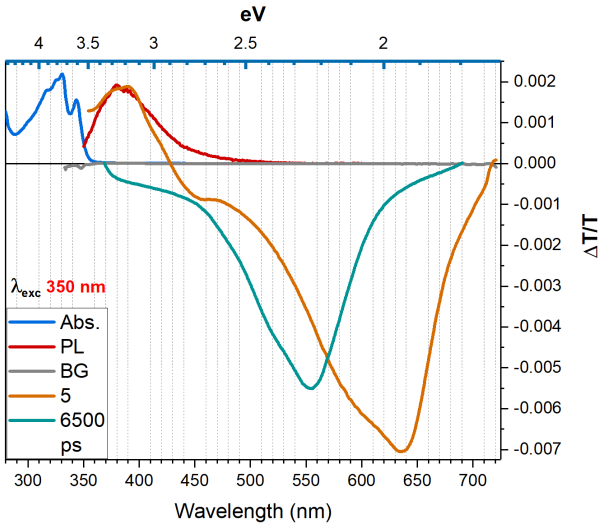

(b) TA $\lambda_{exc_2} 350\,nm$

Figure 5.22. Transient absorption of both excitation wavelengths, absorption and photoluminescence of I-BTBT.

Despite the fact that there is indeed certain excitation wavelength dependence, the behaviour is quite analogous –a shorter lived excited state evolving to another longer lived excited state. For this reason we assign the excited states in accordance with the previous substituents: a photoinduced absorption band close to 600 nm (λ_{exc_1}) and 650 nm (λ_{exc_2}) due to excited singlet state absorption, and another PIA band centred around 530 nm (λ_{exc_1}) and 550 nm(λ_{exc_2}) that corresponds to triplet state absorption. The time-constatnt for ISC in this system is $\sim \tau_{isc} = 500$ps.

5.2.6 2,7-Dioctyloxy-[1]benzothieno[3,2-b][1]benzothiophene

UV-Vis absorption spectroscopy.

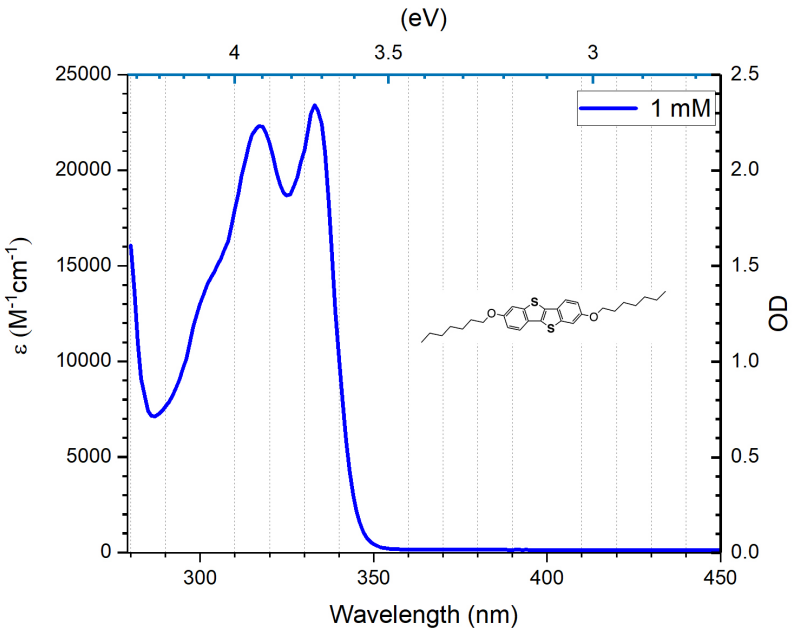

Figure 5.23. Absorption spectra of 1mM C8-O-BTBT in toluene.

For this molecule two alkoxy donating groups have been inserted at the 2 and 7 position of the BTBT core. Figure 5.23 shows a broad absorption band extending from 350 nm (∼3.54 eV) to 290 nm (∼4.3 eV) with two absorbing peaks with almost same intensity; peaking at 333 nm (3.72 eV) and 317 nm (3.91 eV) and what appears to be a shoulder at ∼305 nm (4.06 eV).

Photoluminescence

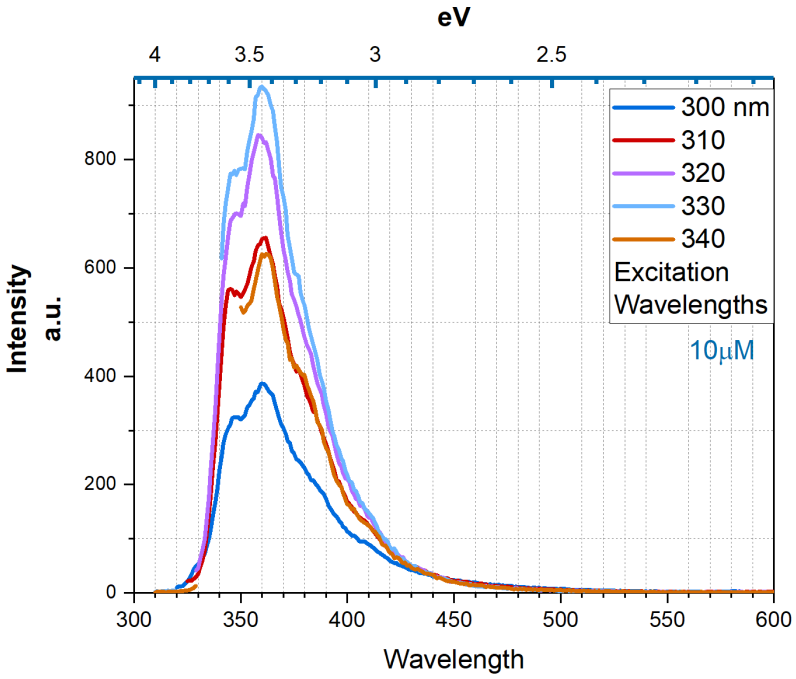

Figure 5.24. Photoluminescence spectra of 10 μM of C8-O-BTBT in toluene, at various excitation wavelengths.

The fluorescence emission spectra of the C8-O-BTBT compound in toluene at room temperature are depicted in figure 5.24. From the figure we observe one emission band ranging from 330 nm (3.75 eV) to 470 nm (2.63 eV) with one readily identifiable peak; located at 360 nm (3.44 eV) and another weak emission peak at 343 nm (~3.61 eV), which, upon closer inspection of the excitation wavelengths, we note it is more defined at the 320 nm excitation. Furthermore, from the figure we can assume not to have small aggregates nor formation of excimer since for we see no excitation dependence. Compared with the others it has the longest tail of emission.

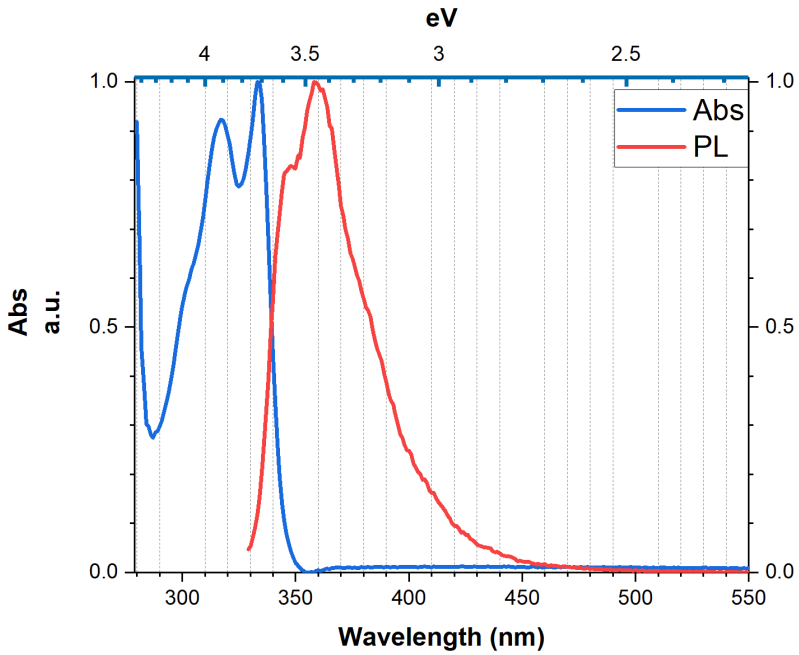

Figure 5.25. Normalised absorption (1 mM) and photoluminescence (10 μM) solution spectra of C8-O-BTBT in toluene.

In figure 5.25 we compare absorption and emission spectra normalised to both maxima. We see a small overlapping region of absorption and emission around 330-350 nm, which should be reflected as a positive signal in the transient absorption (TA). Finally, from the plot we note the smallest Stokes shift from all studied molecules suggesting the rigidity of the molecular structure of C8-O-BTBT.

Transient Absorption Spectroscopy

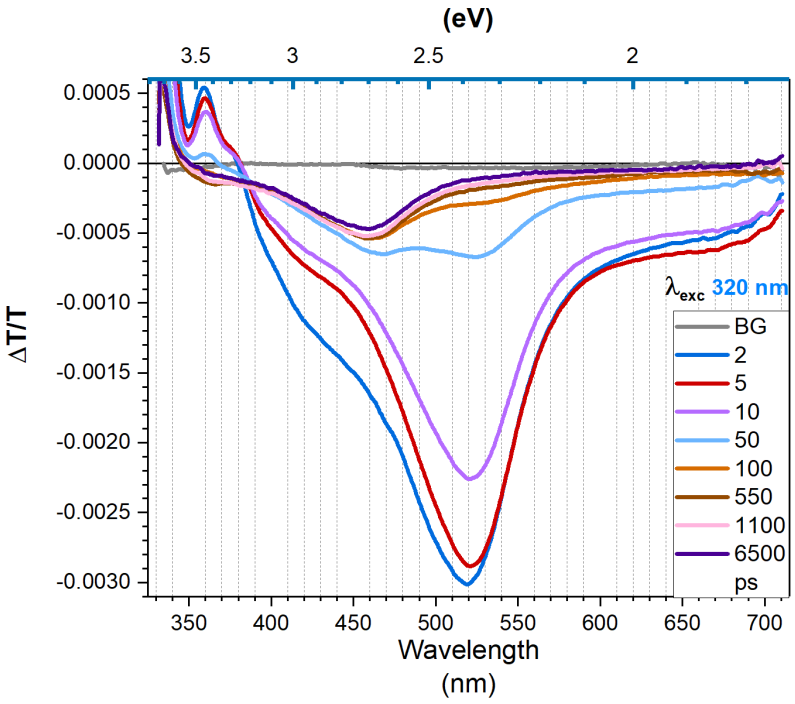

(a) TA spectrum at $\lambda_{exc}320nm$

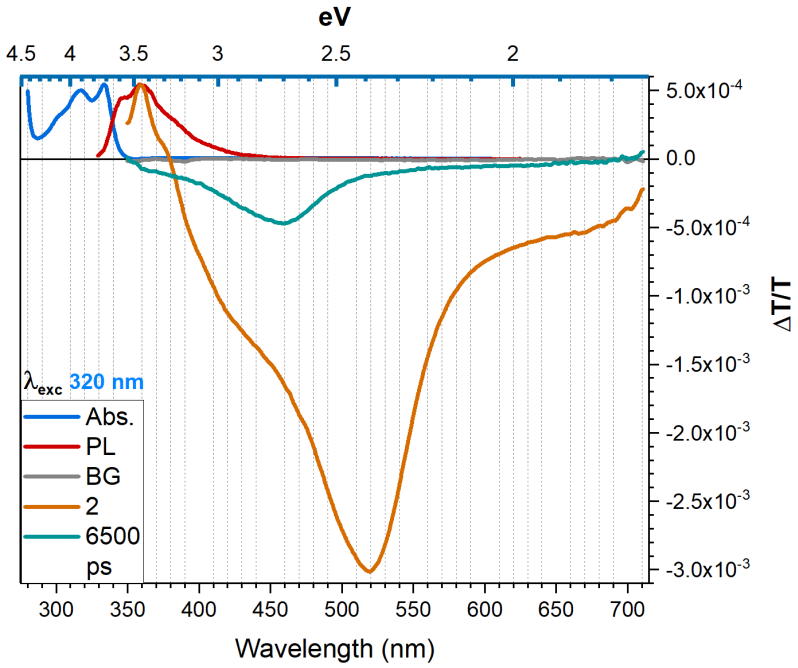

(b) C8-O-BTBT spectroscopical signatures.

Figure 5.26. Transient absorption, absorption and photoluminescence of C8-O-BTBT.

In figure 5.26 (a) we present the data extracted from the transient absorption experiment at the given excitation wavelength. We see a positive $\frac{\Delta T}{T}$ signal located at 360 nm (3.44 eV) which reaches a maximum at 2 ps and decreases with the

same shape and by 50 is minimal and by 100 ps it has vanished. On the other hand, the transient absorption spectrum reaches a minimum of the $\frac{\Delta T}{T}$ signal at 520 nm (2.38 eV). This signal decreases rapidly within the first 50 ps, and although no evident isosbestic point exists, from there it evolves and shifts to the left to be placed at 460 nm (2.69 eV) and appears to remain without further significant changes from 100 ps onwards till the end of the experiment at 6.5 ns.
We take all this into account and plot it in panel (b) of figure 5.26. To conclude we associate the PIA band at 520 nm due to singlets manifold and the longer-lived PIA at 460 nm (2.69 eV) to triplet state absorption.

5.2.7 2,7-fluorohexyl[1]benzothieno[3,2-b][1]benzothiophene

UV-Vis absorption spectroscopy.

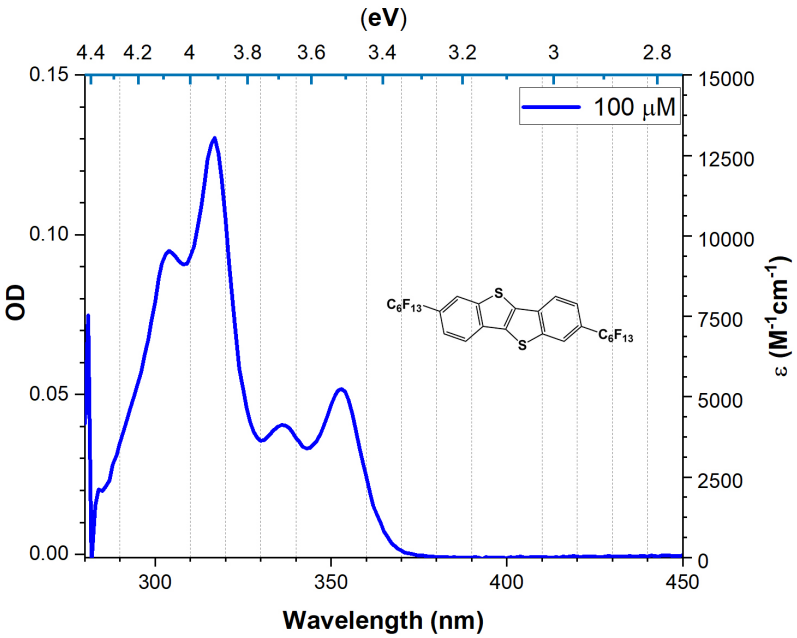

Figure 5.27. Absorption spectra of 100μM C6-F13 in toluene.

For this molecule, two fluorinated hexyl chains were attached at the 2,7 position of the BTBT core. The absorption spectrum shows one broad absorption band spreading from roughly 280 nm to 370 nm ($\approx$ 4.42 to 3.35 eV) with four resolved peaks located at 303 nm (4.09 eV), 317 nm (3.91 eV), 336 nm (3.69 eV) and 353 nm (3.51 eV). We note a low molar absorption coefficient. These features seem to originate from well spaced S_1 and S_2, although as for the NO_2-BTBT case the low energy part of the absorption could be due to undissolved aggregates. This material was hard to dissolve, such that at even a low concentration of 100 μM

the solution was turbid which indicated partial solubility.

Photoluminescence

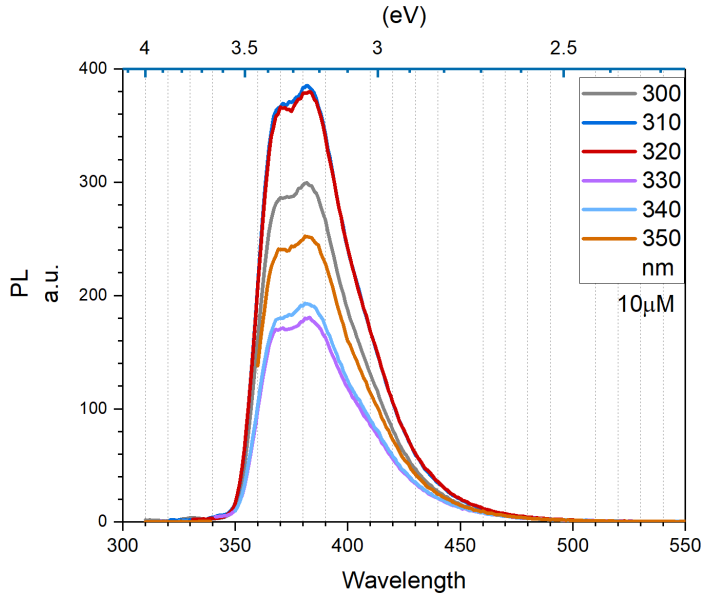

(a) PL spectra of 10 μM of C6-F13 in toluene.

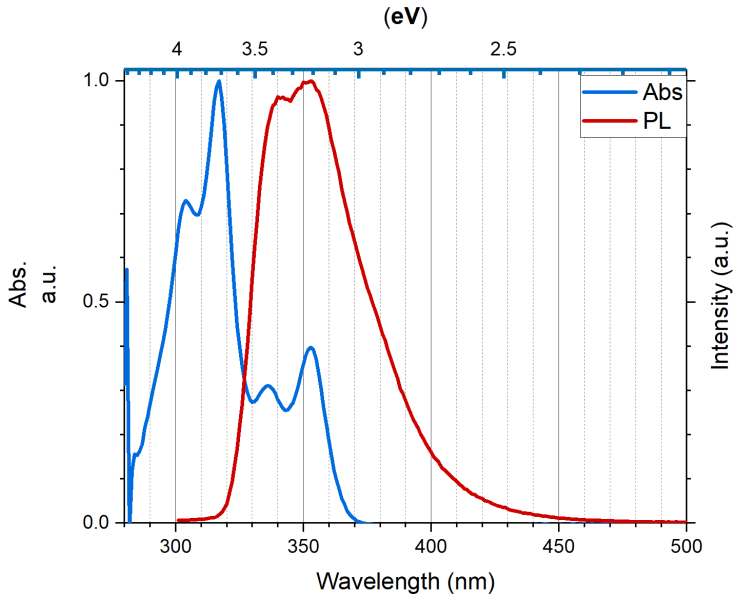

(b) Normalised absorption and emission.

Figure 5.28. Steady state spectroscopy of C6-F13 in toluene.

Figure 5.28 (a) presents the fluorescence emission spectra of C6-F13 as function of excitation wavelength. The first thing to notice about these spectra is that the molecule has a low PLQY. Secondly, we observe a lack of structure in the emission which contrasts with what was observed in the absorption, for we can faintly distinguish two peaks one ~370 nm (3.35 eV) and at ~380 nm (3.26 eV).

Figure 5.28 (b) makes evident the similitude with the previous molecule (nitro substituents) and reveals strong overlap of the spectra and non-Kasha emission. Contrary to what we see for the NO_2-BTBT, we cannot see an evident excitation dependence for the spectral shape. In this case the spectrum remains the same above and below the 350 nm excitation wavelength. To examine this further we studied a the TA spectra, exciting below this threshold and at this wavelength.

Transient Absorption Spectroscopy

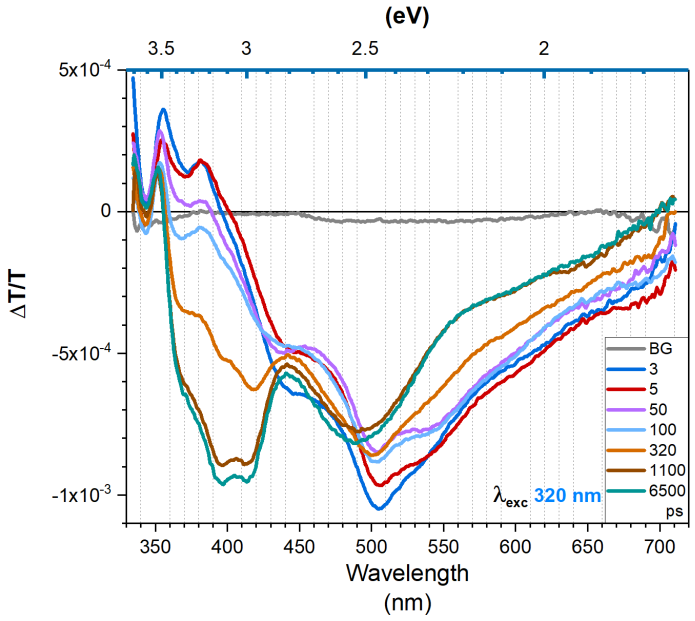

(a) TA $\lambda_{exc_1} 320nm$

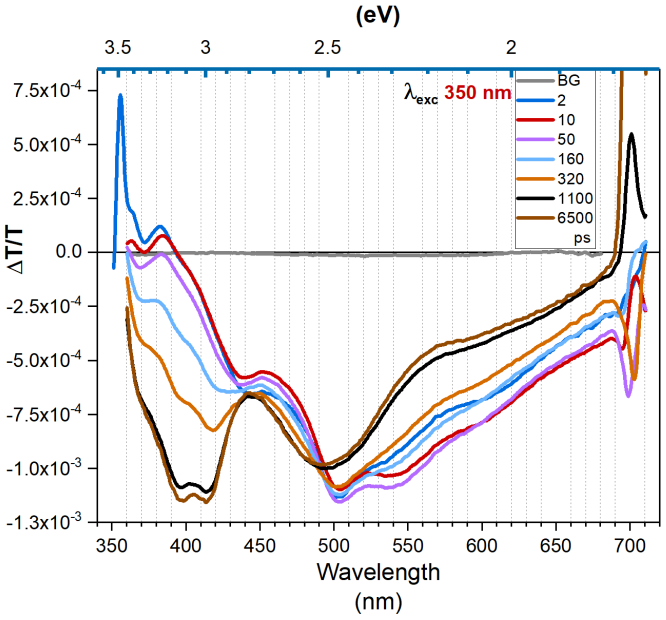

(b) TA $\lambda_{exc_2} 350nm$

Figure 5.29. Transient absorption of 100 μM of NO_2-BTBT in toluene, for the given excitation wavelengths.

Figure 5.29 shows transient absorption spectra with excitation at 320 nm (a) (into what we believe is the monomer region) and at 350 nm (b). In both cases, a positive $\frac{\Delta T}{T}$ signal is roughly ranged from 410 nm to 350 nm (3.02 eV - 3.54 eV) which we can assign to stimulated emission, which in the case of the 320 nm excitation seems to be present at all times in the region of 350 nm. For the negative features of the $\frac{\Delta T}{T}$ signal, we observe that at early times (less than 320

ps) for both cases there seems to be a photoinduced absorption band peaking at 500 nm (2.47 eV) whereas for the 320 nm excitation this peak looks to be sharper and narrower in contrast to the 350 nm excitation wavelength. We see that around 320 nm a new negative $\frac{\Delta T}{T}$ signal starts to emerge peaking at 400 nm (∼3.10) which increases as time passes by and last till the end of the experiment. Finally, for the 350 nm excitation, we see a strong signal at 700 nm due to the pump and unconnected to the optical properties of the molecule. In conclusion, the complex nature of this sample precludes the possibility of using it as a controlled model system and we, therefore, do no further comments on it.

5.3 Conclusions

In this final section, we summarise what we have learnt from the introduction of substituent groups in the BTBT core. We start by acknowledging that our data set can be split into two subsets: those substituents that followed the behaviour of the BTBT core and its most important derivative C8-BTBT, and the two outliers which we consider to be aggregated.

In chapter 4 we described rapid intersystem crossing in BTBT and its alkylated derivatives. Here we have extended the study to include a larger set of molecules containing the BTBT core. From the materials studied, we can extract the following assertion: We can say that for those substituents that do follow the overall photophysical behaviour of C8-BTBT, we observed the same feature in their absorption spectra: one broad absorption band, with almost the same lowest lying absorption onset at ∼350 nm (3.54 eV) and an absence of vibronic structure. We adjudicate such observations to the nature of the electronic structure of the BTBT core, which is inherited to their substituents, for several pieces of data were clear regarding this aspect –namely absorption, photoluminescence, and the transient absorption spectra.
In all cases we observe overlapping S_1 and S_2 excited states. This means that the the closeness of the S_1 and S_2 dominates the absorption features, which is vividly manifested in the absorption spectra of tBut-BTBT, Br-BTBT and I-BTBT (see corresponding figures 5.10, 5.14 and 5.19) which are the spectra that most resemble C8-BTBT. Excitation into the absorption band leads to prompt $S_1 \rightarrow S_n$ absorption features, followed by rapid decay of the S_1. In all cases we observe triplet features in the TA spectra. We therefore conclude that rapid ISC is occurring in all of the above molecules.

Material	τ_{S_1} (Coarse estimate)
BTBT	200 ±5 ps
BTBT-C8	170 ±5 ps
C8-BTBT-C8	120 ps ±5 ps
tBut-BTBT	200 ±5 ps
Br-BTBT	500 ±5 ps
I-BTBT	500 ±15 ps
NH_2-BTBT	100 ±15 ps
C8-O-BTBT	30 ps ±20 ps

Table 5.2. Rate of intersystem crossing for BTBT substituents.

Finally, what we can extract from the transient absorption data, again with the exception of the special cases, is that the intersystem crossing is preserved. However, the trend we observe in table 5.2 is highly counter-intuitive. Generally, incorporation of heavy elements such as Br (Z[3]= 35) or I (Z= 53) should speed up ISC. In this case, the S_1 lifetime instead appears to be lengthened, from $\sim$ 200 ps in BTBT to 500 ps in I-BTBT suggesting slower ISC. Conversely, the most rapid S_1 decay occurs in C8-BTBT ($\tau_{S_1} \sim 30$ps). In the latter case, despite the rapid decay we observe no clear isosbestic point and only weak final $T_1 \rightarrow T_n$ absorption. Assuming the $T_1 \rightarrow T_n$ cross-section is similar in all BTBT derivatives (a reasonable hypothesis given the localised nature of triplet states), we could estimate the relative yield of triplets at 6 ns and we would find that the yield of triplets in C8-O-BTBT is smaller than that of tBut-BTBT. This suggests that additional non-radiative processes occur in the C8-O-BTBT molecule. The most likely candidate is internal conversion caused by the alkoxy chain. Similar behaviour probably occurs in the NH_2-BTBT molecule.

After taking all our substituent systems in consideration we may concede that the photophysics of BTBT containing systems turned to be sensible after all, but shockingly counter-intuitive in other ways. Like when we were expecting that brominated and chlorinated substituents will speed the rate of intersystem crossing, and when it turned out not to be the case, quite the opposite effect, table5.2 verifies this fact. What is most striking perhaps is that even taking into consideration that these values are coarse estimates, it looks like the time-constants are at least twice as halogenated materials. The slow S_1 decay in

[3]atomic number

Br-BTBT and I-BTBT is less easy to understand. The redshifted absorption, photoluminescence and transient absorption spectra compared with BTBT alludes excitation delocalisation into the bromine or iodine atoms. We would, therefore, expect an increase in SOC and a corresponding speeding up of ISC. This does not seem to occur, instead, the time-constant of ISC slows down. We postulate that this is due to the Br- or I- quenching out-of-plane vibrational motion that drives ISC in BTBT and its alkylated derivatives. This could be understood by more planar geometries in the excited states, precluding the out of plane motion.

6 Controlled aggregation and thin films of C_8-BTBT

How do we proceed from isolated molecules in solution to the macroscopic solid-state? An often too complex problem to solve, so no one has a proper answer to it. Although, what can be done, is either to solve its closest-next problem, alternatively building from the closest-known solved problem. Let us review what we have done so far; we presented in previous chapters an in-depth description of the photophysics of C8-BTBT, *with this understanding our main conclusion was that in these molecular* π*-electron system the out–of–plane (*OOP*) vibration is the sole mechanism responsible to enable the intersystem crossing processes and in the case of* BTBT, *the addition of octyl side-chains speeds it further, in a non-negligible way. Then we moved the research forward to study the effects when electron-withdrawing and electron-donating substituents are introduced into the* BTBT *core. Our discovery proved that there is no obvious heavy atom effect in connection with the* ISC *in these* BTBT*-systems, for ultimately the addition of Bromine and Iodine to the* BTBT *core slowed down the rate of* ISC*. We have pondered on this, and we speculate that it could be understood if we note a plausible effect of the '*in-plane*' vibrations of the heavier atoms. They may pose too much strain to the already delicate interplay of the* out-of-plane *vibrational modes originating in the core and the spin-orbit-coupling, which we think is what drives the intersystem crossing. What this means, is that it could be quite possible that there is a damping of the key* OOP *vibrations modes involved in* ISC*. We may think of this in a rather cartoonishly way by picturing the typical '*tumbling*' –the jumping device; heavier atoms would mean more tension, so less jumping and consequently less height for each jump, regarding the tumbling as the molecule plane and the person jumping up and down the* OOP *vibrations. So far, we have dealt only with solutions, but in doing so we have left out virtually all of the existing solid-state applications, for the majority of optoelectronic applications the focus is on solid-state devices. To bridge this gap, here we concentrate on what happens to the photophysical properties of* C8-BTBT *as we go from small aggregates to the solid-state. Contrary to solutions, where molecules move more freely -or diffuse, in the solid, it is clear that the molecular environment changes, now our molecules are no longer confined to the solvent cage, and they are readily able to interact with same molecules or new ones. Therefore, is obvious that we expect to see changes in the photophysical properties of the material.*

6.1 Introduction

6.1.1 Motivation

Our world faces several seriously critical challenges: an ever **INCREASING** energy demand, constrained resources, limited space, massive losses of biodiversity, humongous generation of waste (household and Industrial), contamination of land, water and air; with their obvious global impact on climate change. Many, naïvely believe that is science's duty to rescue us all, to '*solve-it-some-how*', to engage and defeat these issues. The dark truth is that none of such scientific responses, if any, will significantly alleviate these global issues, unless we forcefully expedite the implementation of solutions that are already available, with the understanding that of much needed collective-global paradigm shift.

Quite surprisingly, 'synthetic biology' is seen by some, as a very plausible solution to many of these problems for a quick survey of such topic the reader is directed to J. Davies' *Synthetic Biology* [123]. The selling point for promising applications in the nanosciences (where the typical paradigmatic frontier between physics, chemistry and biology blurs) is to tackle such pressing issues and solve long-standing problems. Succesful research along these lines is achieved whenever its relevance focuses on the wider community as well as the value and priority of such problems. Thus, no surprises in the enormously stacking research to find alternatives for our current energy consumption/production problem. These solutions range widely; from the long establish solar cells, commercially available from 1955 in their silicon [10] and still dominant version to their now branched type for organic and hybrid semiconducting materials as well as the perovskite solar cells, which have gained strong traction in the past decade, with unprecedented 22.1% certified efficiency to light-harvesting antenna complexes with DNA tuned efficiencies [124] and to genetically engineered microalgae for commercial biofuel production [125].

Photobiology and Biophysics now are either departments by themselves or they account for a significant division of cross-faculty departmental research resources. A quick way to rationalise this behaviour is by acknowledging two facts: Firstly, organic semiconducting polymers, as well as small molecules, have an intrinsic resemblance to many biomolecules. We just have to look at some of them (see figure6.1 below), for in one hand we have the porphyrin molecule, and on the other hand, we have the chlorophyll and haemoglobin molecules to view this striking link. This is a natural appeal for biological applications.

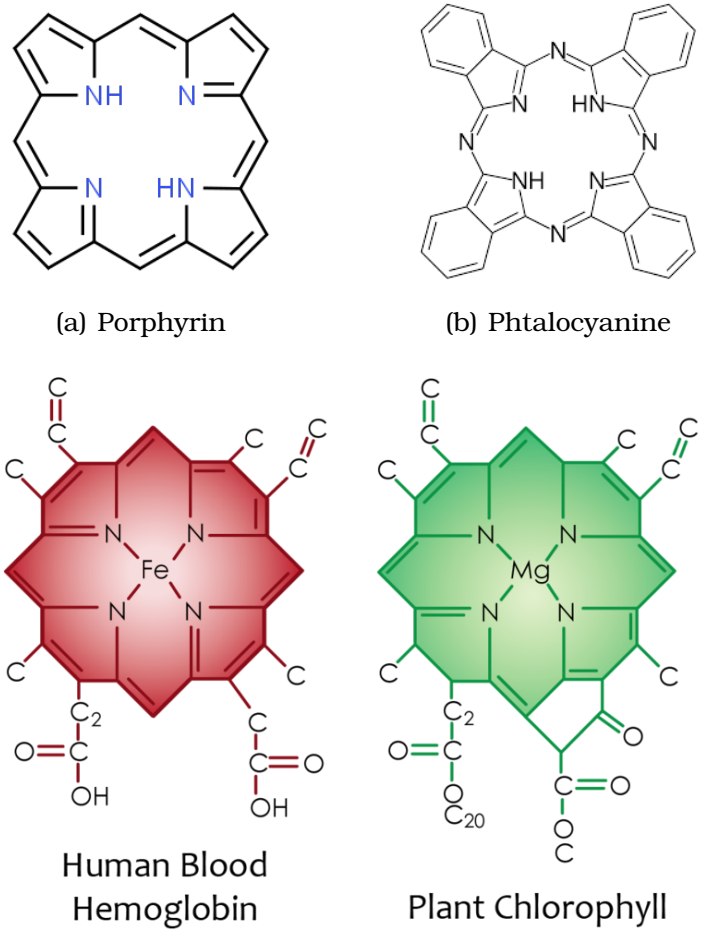

(a) Porphyrin

(b) Phtalocyanine

(c) Fundamental Biomolecules

Figure 6.1. Visual support for our claim about the striking similarities among biomolecules and organic semiconducting molecules.

Secondly, the fact that certain processes are dealt remarkably well within biological systems; two major exemplars are light-harvesting antenna complexes and their instrumental role in photosynthesis as well as light-induced charge separation processes [123], for not mentioning how spectacularly well done DNA does its block-building. Researchers have already produced molecular moieties that outperform their biological counterparts [126]; by extending their spectral range or by increasing the absorption coefficient. Thus researchers have devised different routes; one is to directly modify the existing natural proteins via genetic engineering, and another approach that has gained momentum, is the development of novel water-soluble light-harvesting proteins[1] as an alternative to those found in nature for applications, *e.g.* to capture solar energy [127] or to manipulate plexciton (plasmon-exciton) coupling by site-specifically binding synthetic proteins to gold nanostructures [128] (see

[1] Hence the sophisticated term '*De novo*'-proteins, maquettes etc.

figure 6.2 below). Our focus centres on the latter route - the development of new proteins. So, molecules like tetrapyrroles, porphyrins, chlorins and related molecules are always producing new publications, for they serve as stepping stones to new improvements[127–135]. Due to the particular wavelengths of absorption and emission of these molecules, which are known and can be tuned.

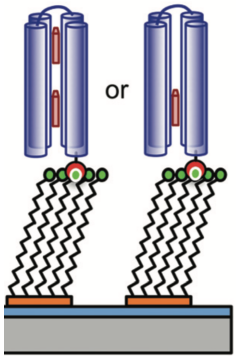

Figure 6.2. Schematic representation of Q-dot and complex binding. Adapted with permission from [128].

6.1.2 Synthetic proteins brief history

One of the main biological discoveries of the past century was the establishment of the central role of proteins in life in general, they are responsible for regulating many structural, chemical, and behavioural cell processes. Such as providing structure to cells and organelles, molecular transport from one location to another, *e.g.* diffusion of water and urea molecules through the *phospholipid bilayers* is accelerated by a transport protein -*symporter* [136]- and for instance, in cell behaviour they also play an instrumental role in *cytogenesis* [137]. Since Friedrich Wöhler in 1828 successfully synthesised the urea molecule [123], previously known only to living organisms, production of proteins - both naturally occurring and synthetic - remain at the forefront of research and development in industry and medicine. DNA is without a doubt another instrumental discovery of the twentieth century, in particular, its capability to build proteins from instructions stored in it. This concept led to the birth of modern biotechnology, which goes back to the 1970s when the group led by Yamada famously synthesised the first gene - when they made an artificial copy of yeast gene [123]. The idea of synthesising DNA and having cells to use it to make proteins, instead of making the proteins directly from pure chemistry is a radically different approach, that has added the rapid development of biotechnology. So, not surprisingly two medically important developments followed suit: When the human hormones *somatostatin* and *insulin* were successfully produced with genetically engineered bacteria in 1976

and 1979 respectively [123]. More recently, a great example of a real-world application of synthetic biology is the *Arteminisic acid* synthesis. *Artemisinin* is found in wormwood plant (*Artemisian annua*) and its importance lies in connection to its anti-malarial properties, a disease that kills around one million people worldwide. Synthetic biologist Jay Keasling won a Bill and Melinda Gates Foundation grant for cheaply producing artemisinic acid by bacterial production, incorporating genes from the plant and the *brewer's yeast* to optimize the production of the artemisinic acid from which simple chemical purification yields artemisinin.

Biological systems have already solved the problem of light-harvesting and energy storage in an impressive and highly efficient way. All bio-inspired machines cannot rival biology - which currently is 5 times more efficient by any man-made technology. Biological systems are useful for their performance, in particular, *electron-transfer* processes, which is essentially a controlled flow of electrons, basis of all electronic devices[2]. Everything in biology is driven by electron transfer [138], in particular processes like oxygen binding, respiration, detoxification, charge separation, reducing CO_2 and of course photosynthesis that takes place in plants and other organisms [137]. So, one obvious application is in light-harvesting and energy conversion. Take for example Grätzel Solar cells, where light-activated pigments directly relatable to plants and photosystems creates electrical energy by diffusion of electron-donor and acceptor by diffusion in fluids. So the idea is to make solid-state structures with de-novo proteins, similar that appear in nature that reproduce what biology does but are significantly less complex.

Proteins are attractive for they have precisely defined structures, theoretically offering control of both the density and orientation of binding sites for optically active ligands. Advances in genetic engineering of light-harvesting proteins have aided researchers to explore a wider range of questions and deepen our understanding of photosynthesis. Like it was exemplified in DNA *origami light-harvesting structures* shown by Hemming and coworkers in 2016 [124].
Photosynthetic antenna complexes capture sunlight with extraordinary efficiency, they funnel this energy into reaction centres to drive the formation of charge-separated states. In purple bacteria and chloroplasts, the capture of photons leads to the formation of excitons, which are delocalised across several pigment molecules within the bio-complex via coherent electronic coupling; this has prompted an intensive spectroscopic investigation of light-harvesting

[2]But in cellular processes; sodium, potassium and calcium ions are transported [137] too.

complexes (LHCs).

6.1.3 The '*Maquette* approach for protein design

In the '*maquette*' approach, Dutton and coworkers [134] iteratively develop a minimal four-helix scaffold. By beginning with a generic protein genetic-sequence designed only to adopt a simple helical bundle fold and iteratively adding engineering elements onto this stripped-down protein chassis to increase the number to four. Maquettes are synthetic proteins that consist of α–helical bundles that may be designed from scratch to incorporate cofactors. Proteins made by this method, integrate sophisticated functions into a protein with sequences that are entirely unrelated to any natural protein hence the flamboyant term -*de novo*. These four α–helical proteins, in a single sequence of amino acids, that self-assemble to form a bundle that envelops histidine binding sites that can bind to a variety of ligands including tetrapyrroles[135], as well as synthetic chlorins [128, 135], and more recently carothenoids[139].

De novo protein design also known as the *maquette* approach, draws on the long-established methods used by architects and sculptors in which simple models, maquettes, are progressively altered to give more detailed characteristics. *De novo* protein design involves the rational engineering of simple peptide structures to fulfil the desired function. The principle of maquette design is to have a simple primary amino acid sequence to achieve a desired protein structure and function, starting from these structures, details can be included through an iterative process. The development of maquettes was also inspired to test current understanding of protein folding, for instance, maquette designs have solely adopted α-helical secondary structures, for various reasons, principal among them is the stability of helices in solution, which avoids the formation of aggregates commonly found in model β-sheet structures. Finally, the binary patterning of polar and non-polar residues within helical sections affords a simple design approach that can facilitate predictable self-assembly and structure.
Maquettes are human-made macromolecular structures, that to say it coarsely, form -cavities within, they use the Van-der-Waals and hydrogen bonding which accounts for hydrophilic and hydrophobic regions in proteins to assemble themselves. Biochemistry knowledge and ethical legislation have evolved so far that protein-building genes can be inserted into *E. Coli* to produce tetra α-helical structures. Our tetrahelical protein design strategy implied an intramolecular hydrogen bonding in α-helical peptides results in two helical turns every seven residues. Binary patterning of polar (*P*) and hydrophobic (*H*) residues according to the general HPPHXPX repeat motif (X may be either H or P) which resulted in water-soluble, four-helix bundle maquette proteins engineered to incorporate non-biological chromophores.

6.2 Sample Preparation

Protein synthesis and maquette binding was performed by collaborators from the Department of Biomedical Science (University of Sheffield, UK).
All the maquette producing genes discussed were purchased from DNA 2.0 (now ATUM) and provided in the plasmid. The BT6 maquette was modified by substituting the four histidine residues for alanine residues, generating the variant named BT64A. As the histidine residues are believed to be located in or near the hydrophobic cavity of the protein, these changes were predicted to progressively increase the hydrophobicity of the core. In figure 6.3 we have shown the typical maquette structure in panel (a) where the four pillar proteins (bright colours: red, blue, green and yellow) previously mentioned are visible, and in panel (b) we see at the centre of the figure a red coloured structure which we identify with an organic pigment used in previous research from our spectroscopy-group, and in the right part of the panel, we depict what happened in that carotenoid case, where two molecules go inside the cavity form in the core of the maquette.

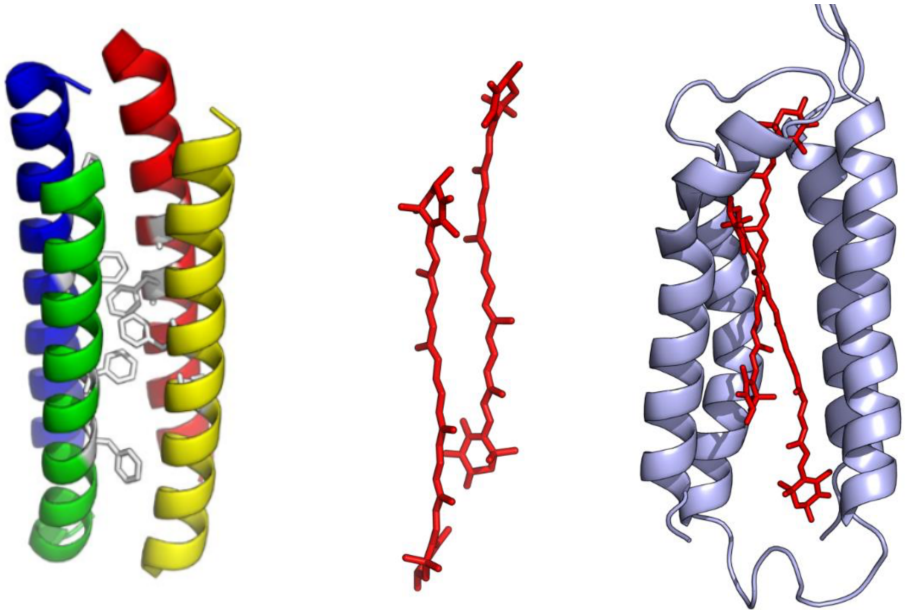

(a) (b)

Figure 6.3. (a) Structural model of tetrahelical BT64A Maquette-protein, hydrophobic phenylalanine residues are highlighted in white. (b) BT64A protein (purple) with astaxanthin dimer(red) unbounded and bounded (left and right respectively). Figure adapted with permission from Dr. Daniel Polak.

All maquette proteins were produced and purified from E. coli BL21 (DE3). Briefly, 500 mL cell cultures were grown at 37 °C to an optical density of OD∼0.6

at λ =600 *nm*, after which production of the maquette was initiated through induction of the bacterial promoter. Following induction, cells were cultured for a further 4 h at 37 °C before lysis by sonication. Following clarification of the cell lysate, maquettes were initially purified by immobilized metal affinity chromatography (IMAC).

C8-BTBT was solubilised in 100% (DMSO) at 60°C with sonication to give stock solutions of (269 μM) with the ground-state absorption recorded after dilution to 54 μM. Briefly, the stock C8-BTBT solution was added in a 1:4 (v/v) ratio to a solution of 50 mM HEPES[3] (pH 8.5) containing the maquette (label as BT64A), with the concentration of protein 20-fold less than that of the chromophore. The incorporation reaction was incubated for 30 min at 4, 37 and 50 °C, before four-fold dilution with chilled 50 mM HEPES and filtration (0.2 μ m pore diameter). The filtered solution was then applied to AEC column[4] to remove unbound pigment.

As was mentioned before, due to the biological nature of this sample, our collaborators were tasked with the synthesis of the maquette proteins and our task was the analysis of the spectroscopical characterisation. Hence, all further information related to the synthesis and other characterisation techniques used for maquette-proteins is contained the thesis entitled 'De novo designed proteins for applications in research and biotechnology' by Dr Andrew G. Sutherland [140].

6.3 Results

In this section, we present for the first time (as far as we are concerned) a detailed study on the spectroscopy features of this maquette: chromophore complex. To place our findings in context, we have reproduced the main spectroscopical findings of the chapter 4 in the following figure.

[3] *(4-(2-hydroxyethyl)-1-piperazineethanesulfonic acid)* or simply HEPES, is a sulfonic acid buffering agent. HEPES is widely used in cell culture, largely because it is better at maintaining homoeostasis, HEPES resembles water as far as dissociation is concerned - it decreases as the temperature decreases. It is for this reason that HEPES is an effective buffering agent for maintaining proteins at low temperatures without loss in structure nor function.

[4] A variant of *Ion exchange chromatography* which uses anions.

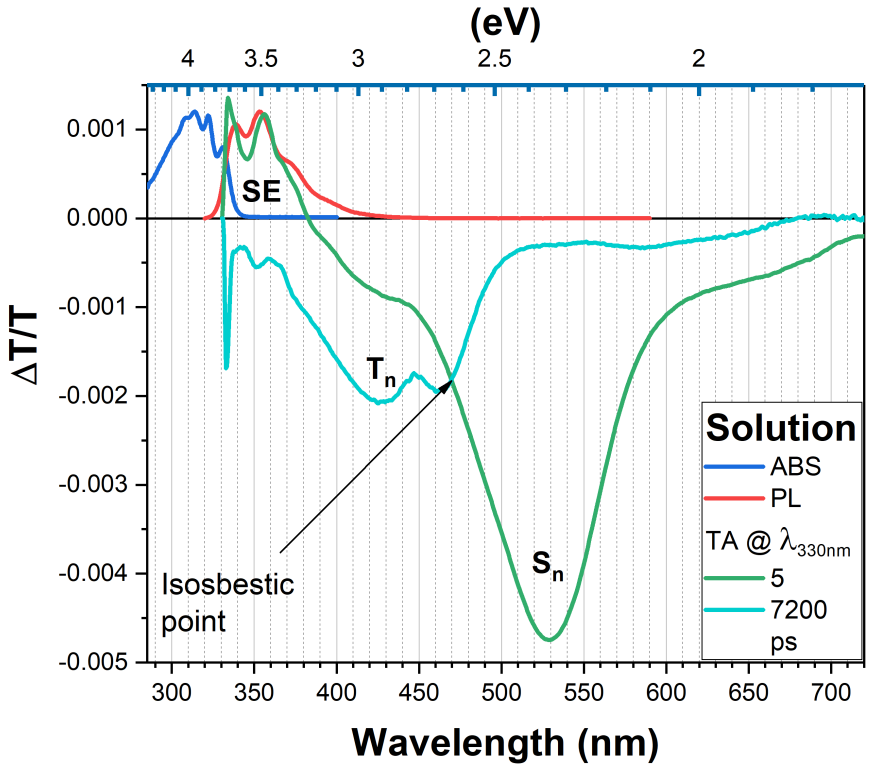

Figure 6.4. Spectroscopical fingerprint C8-BTBT in toluene solution at room temperature. From left to right; Abs. (blue curve), PL. (red curve) and Transient Absorption depicting photoinduced absorption for both excited state manifolds: singlet (S_n) (green curve) and triplet T_n (cyan curve). Notice the region labelled as **SE**, here the overlapping between green curve and the PL curve is remarkable. Since the pump wavelength is close to 330 nm, this explains why we see sharp spikes in the left hand side of the TA curves, finally we have labelled *isosbestic point* as the place where TA spectra at 5 and 7200 ps intersects, in this point excited species population are equal.

Figure 6.4 condenses all the photophysical knowledge of C8-BTBT, it shows the absorption spectra (blue curve), which at this point we understand its convoluted and structureless caused by the presence of S_1 and S_2 in near viccinity. Moreover, our DFT calculations estimated a higher value for S_2's oscillator strength, which is why we don't identify the (0-0′) transition with the highest intensity. Next, is the PL in the red curve that presents vibronic structure from the S_1 Kasha emission, followed by the transient absorption signatures (at shorter time in green and longer time in cyan) that clearly depict the photo-induced absorption of a singlet manifold, the isosbestic point and the PIA band corresponding to excited-state absorption of the triplet manifold.

6.3.1 Maquettes

UV-Vis Absorption

Figure 6.5 represents the steady-state absorption spectrum of C8-BTBT embedded in the maquettes. Analogously, as occurred to C8-BTBT, we proceeded to find the optimum pump pulse wavelength for the initial excitation.
In the figure from panel (a), we identify two main band-peaks, the strongest located in the 210 – 260 nm (5.9 – 4.7 eV). The second, less absorbing band extending from 310 nm (∼4 eV) peaking at 360 nm (3.44 eV) is where we are going to concentrate for reasons exposed further below. As commonly observed in other molecular systems, a redshift in the absorption spectrum appears from isolated molecules to molecules in aggregation. This is generally caused by molecular aggregation, in our case, the bathochromic shift is around 30 nm (0.31 eV). We see significant absorption in the monomer region which is not the case for the thin film. Which means we have other absorbing species, this seems interesting, for it looks like we are in fact tuning the amount of aggregation among the molecules. Indeed, the interaction of the maquettes and the fluorophore molecules takes place, and as a result the absorption spectrum changes. What we see then, from comparing the isolated molecules in solution is that the position of the peaks have changed, and some of them have been suppressed completely. In the complex, the spectrum looks cleaner with more defined features but a bit broader than for the monomer case.

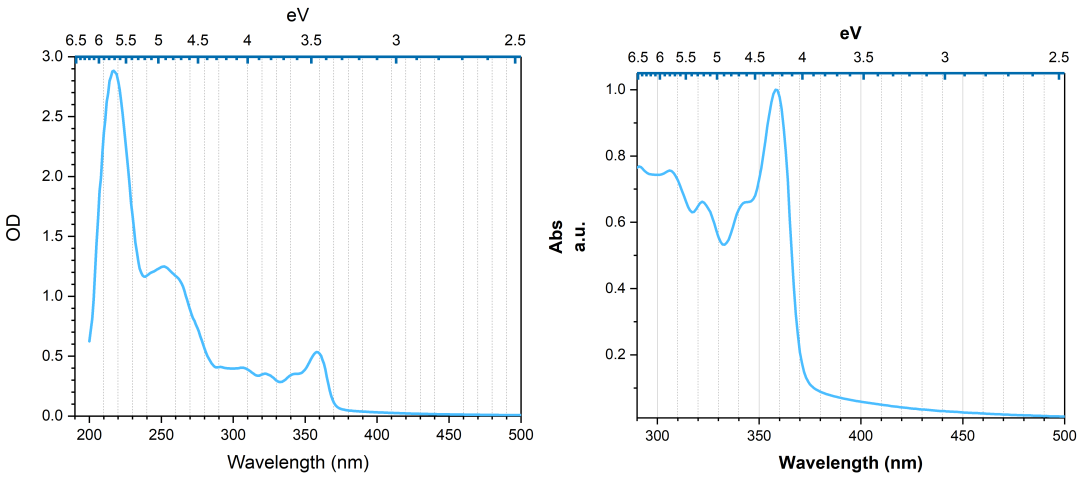

(a) Optical density of chromophore complex.

(b) Absorption normalised to S_1 peak of absorption.

Figure 6.5. Absorption Spectra of C8-BTBT embedded in a maquette protein in buffer solution.

Photoluminescence

Figure 6.6 further below, in panel (a) depicts the fluorescence emission spectra of C8-BTBT-maquettes complex, excited in ten-nanometre interval from 300 nm to 360 nm (4.13-3.44 eV). On this graph, we see emission from various excitation wavelengths, with two emission bands extending from 300 nm to 510 nm (4.13-2.43 eV). We observe that the 300 nm (4.13 eV) excitation wavelength creates a somewhat different spectrum than the other excitations, we think this is caused by residual emission from other chromophores in the sample. Followed by the less emissive band ranging from 370 nm to 400 nm, and finally a broad featureless highly emissive band. From the panel (b) of the figure, we observe that regardless of the excitation wavelength the spectral shape remains unchanged. The less emissive band peaks at 370 nm and the second peak from left to right to be found at 390 nm (3.35 eV, 3.18 eV) showing a clear mirror image of the absorption spectrum, with vibronic structure, suggesting it comes from exciton emission having a small Stokes-shift of 0.09 meV. While the second more and more emissive band peaks at 430 nm (2.88 eV), we see a vibronic shoulder at 460 nm (2.69 eV), this band is considerably shifted to the red compared to the main exciton emission, and we tentatively assign it to excimer emission.

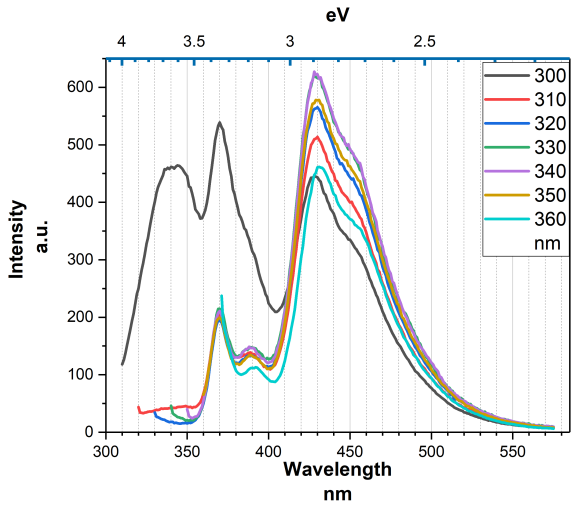

(a) Photoluminescence spectra for different excitation wavelengths.

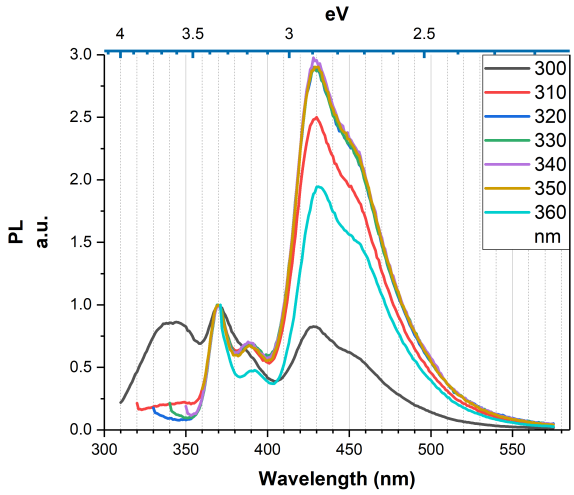

(b) Emision normalised to the S_1 emission peak.

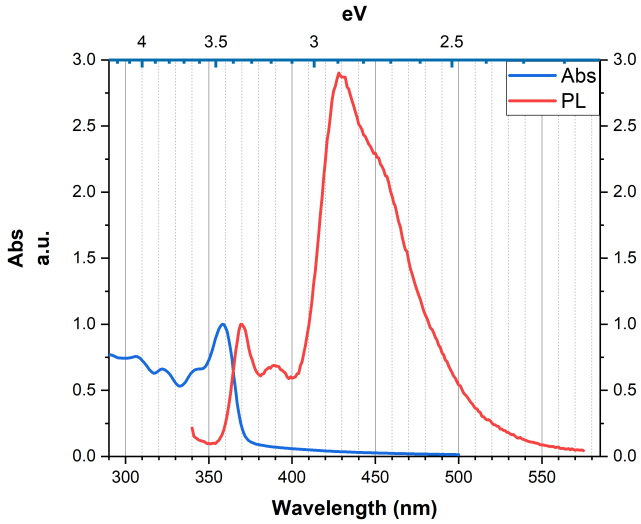

(c) Absorption and Emission normalised to the S_1 peak. In order to highlight the small Stokes-Shift as well as the mirror symmetry of excitation and emission for S_1.

Figure 6.6. Steady state spectra of C8-BTBT embedded in a maquette protein in buffer solution.

Time Resolved-Photoluminescence

What figure 6.7 shows, is an interesting comparison among photoluminescence experiments; the steady–state extracted in the previous section (solid red line) and the one obtained through time-resolved photoluminescence experiments.
By carefully observing the TR-LP we show that emission in the excitonic region (peak at ∼370 nm) starts within the first 10 ps (solid thin yellow line) and until 50 ps is the only emission. By the first 100 ps, exciton emission has reached the maximum, and excimer emission has already started. Within the first 250 ps the excimer emission reaches its maximum light emission, and by 1 nanosecond excimer emission is the only light falling on the detector. This is the reason why on the steady-state PL we saw that the highest intensity peak corresponded to the excimer emission, now is understood when noting that those emitted photons are being collected for longer times than those corresponding to excitonic wavelengths. Thus, even that the majority of intensity in the TR-PL comes from excitonic emission, it lasts considerably less than excimer emission which is in agreement with what is shown in the steady-state photoluminescence. These results could be suggesting the existence of a short-lived species (due to excitonic emission) and a longer one (due to excimer emission). To understand this behaviour in more detail, we gather more information through *Transient Absorption* experiments at different excitation wavelengths for probing the origin of the emitting species; one for the excitonic region (centred at $\sim$ 330 nm) and one for the excimer region (*idem* $\sim$ 360 nm).

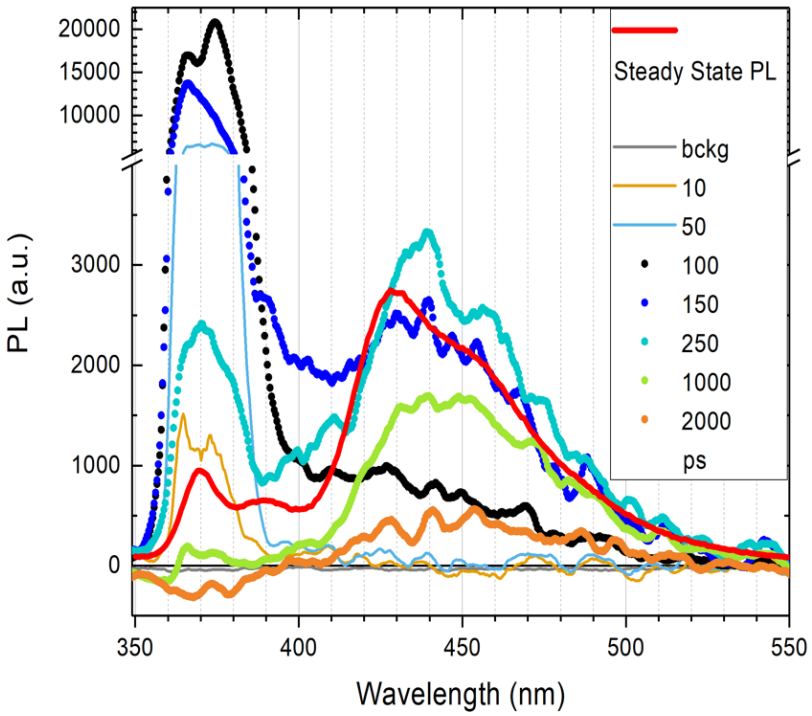

Figure 6.7. Time-Resolved PL spectra of C8-BTBT:Maquettes complex for various times, ranging from 10 ps to 2 ns. Comparison shown among TR-LP and steady-state (solid red line) reveals two emission times.
λ_{exc} at 330 nm.

Transient Absorption

To deepen our understanding we carry TA spectroscopy experiments and cases like this are where TA prowess is fully enshrined, for it comes to light the nature of dark states, and population dynamics are revealed, as well as to supplement what we already now from steady-state spectroscopy and time-resolved photoluminescence data.

We use a couple of beams of light roughly centred at 330 nm wavelength to excite the monomeric-type absorbing region, and another one, centred around 360 nm wavelength to coincide with the peak of the excitation for the films of C8-BTBT and for is close enough for the maquette complexes, see figure 6.8 below.

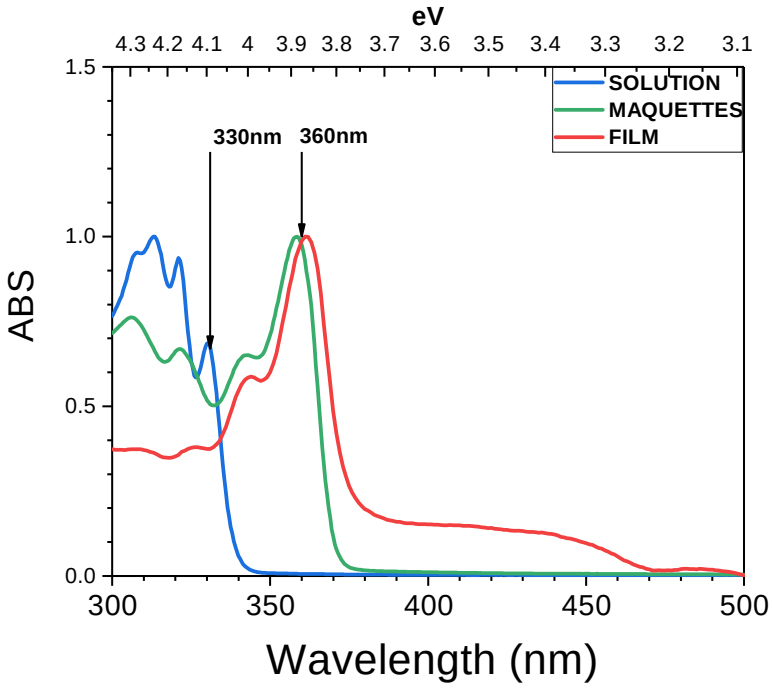

Figure 6.8. UV-Vis absorption spectra of C8-BTBT in different molecular environments.

Figure 6.9 shows the colour map of TA for different pump fluences. At first glance, from panel (a) to (c) seems they are not to be significantly different, the same can be said to panels (d) to (f). Moreover, comparing the top and bottom panels the differences are negligible, which suggest no excitation wavelength dependence as well as no fluence dependence. Which is quite fascinating for in a 2010 study albeit in aqueous Gold Nanorods suspensions [141] authors found that at low excitation fluences, the energy is distributed into two modes. They concluded that the bleaching and relaxation times are directly related to energy distribution into different modes, which are excitation wavelength and fluence dependent. It was worth to mention simply for highlighting the importance of certain modes, and by modes we mean of course *vibrational-modes* as we have stated relentlessly.

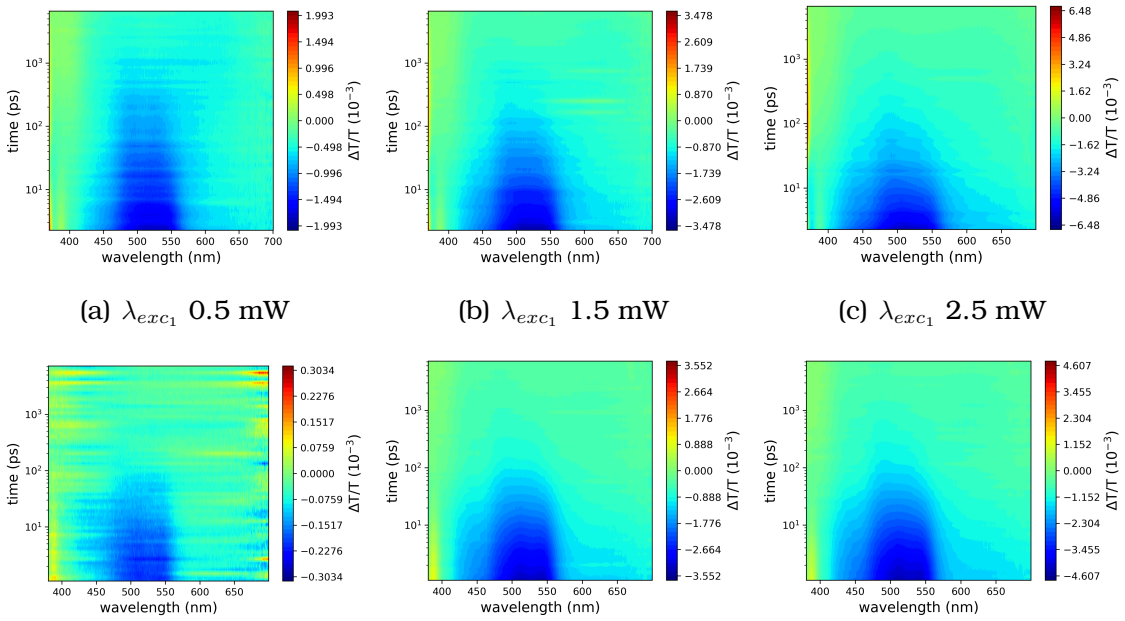

(a) λ_{exc_1} 0.5 mW (b) λ_{exc_1} 1.5 mW (c) λ_{exc_1} 2.5 mW

(d) λ_{exc_2} 0.45 mW (e) λ_{exc_2} 1.5 mW (f) λ_{exc_2} 2.5 mW

Figure 6.9. Pump fluence dependence on the transient absorption of the C8-BTBT:maquette complex. Figure depicts TA 2-D Maps, where the $x-axis$ denotes wavelength, the $y-axis$ time and colour bar represents the $\frac{\Delta T}{T}$ signal. Excitation at 330 nm (top row) λ_{exc_1} and at 360 nm (bottom row) λ_{exc_2}.

Further in figure 6.10, we start looking at a general similarity among both excitations wavelengths in the TA. For both excitations, a negative $\frac{\Delta T}{T}$ signal indicates an excited state photoinduced absorption, ranging from 400 nm to 700 nm. It reached a minimum within the first 5 ps, and then by 50 ps it has already decayed more than half, we note also, that by this time the band is broad and featureless. By the 1000 ps (1 ns) the signal lacks any peak and is spread over the entire probe range, from this point in time onwards there seems to be no significant change in the spectral shape, hence no changing dynamics.

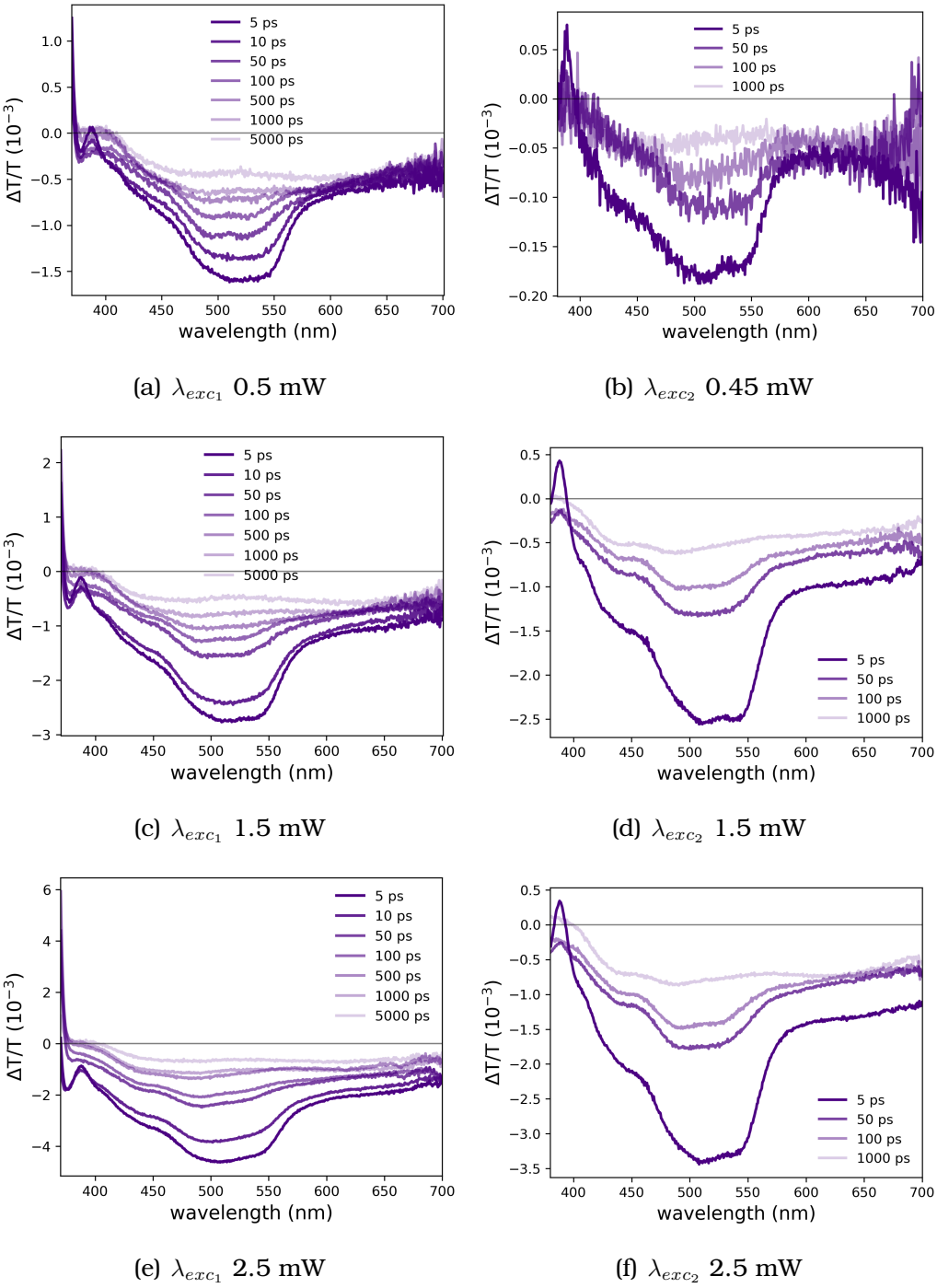

(a) λ_{exc_1} 0.5 mW (b) λ_{exc_2} 0.45 mW

(c) λ_{exc_1} 1.5 mW (d) λ_{exc_2} 1.5 mW

(e) λ_{exc_1} 2.5 mW (f) λ_{exc_2} 2.5 mW

Figure 6.10. Pump fluence and excitation wavelength dependence on transient absorption spectra of C8-BTBT:maquette complex excited at λ_{exc_1} 330 nm and λ_{exc_2} 360 nm.

Summary

Finally, what we have gathered so far, is an absorption spectrum featuring two absorbing regions; one believed to be of a small amount of monomers and a more pronounced absobing feature due to aggregates composed of at least two molecules per maquette as was found to be the case in the carotenoid study

that we mentioned before. Moreover, when studying the emission spectra we came to the conclusion that it comes from two type of excitations –from excitons and excimers. Thus, in order to discover the origin of such extraneous emission we performed transient absorption and that ended telling that eventhough there seems to be a long-lived optical specie there is no evidence pointing out for it to be from triplet origin. For we did not found its signature. Furthermore, this figure highlights a very interesting phenomenon - a plausible effective mixing of singlet and triplet as panel (b) timidly suggests.

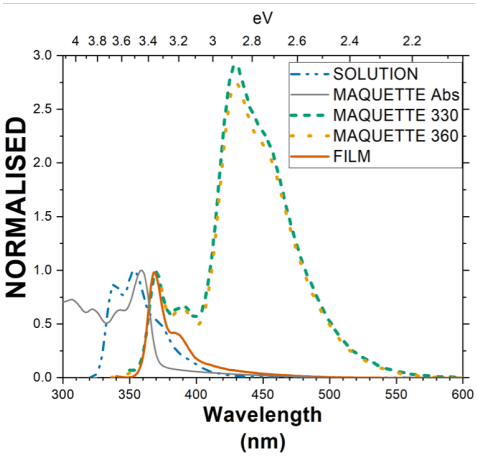

(a) UV-Vis steady-state Spectroscopy data comparison. Complex absorption in solid light-gray curve, solution PL emission in dashed light-blue, 8-BTBT:Maquette complex emission for selected walengths in dashed green and yellow and Thin-Film emission in solid orange line.

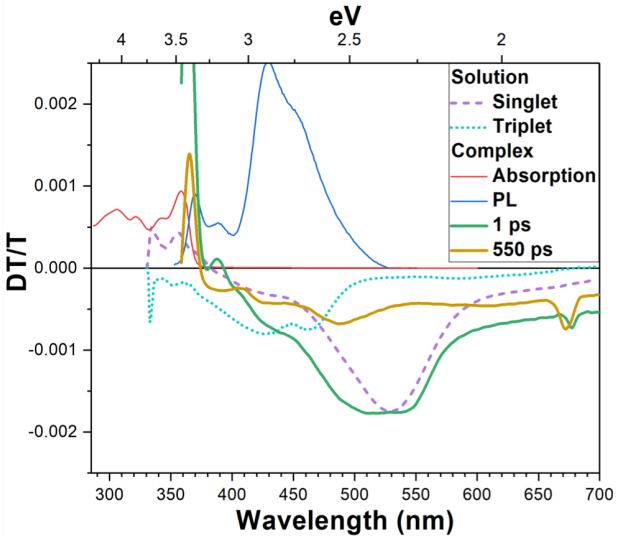

(b) Both c8-BTBT solution and c8-BTBT:Maquette complex TA main features comparison. Note how there is vaguely resemblance between dotted and solid lines.

Figure 6.11. c8-BTBT:Maquette complex spectroscopical fingerprint. Transient absorption spectra for selected times. For the Maquettes the sharp lines at 350 nm and at 720 nm are due to residual 330 nm laser excitation and its second harmonic generated pulse.

6.3.2 Thin Films

Evaporated films were made while working in collaboration with Dr Luke Rochford from Warwick University as well assistance with the AFM and X-ray characterisation.
In figure 6.12 we show the non-optical characterisation of the evaporated thin film. We can see how the surface of our sample is smooth and with the typical "terrace" growth of molecular layers (in gradient colours) similar to what has been reported previously, *e.g.* the work published by Liu and coworkers [142]. In the panel (b) of the same figure, we can appreciate the high crystalline nature of the sample supported by the sharp nature of the X-ray peaks.

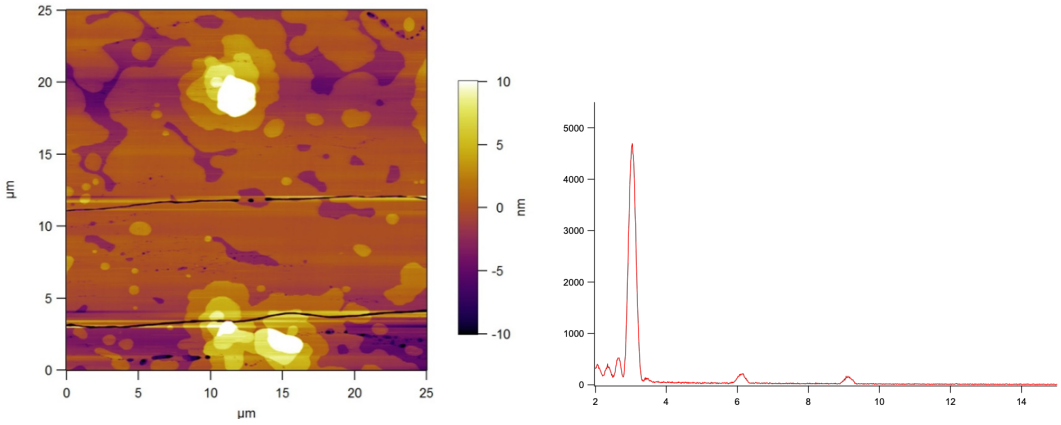

(a) AFM (b) X-Ray

Figure 6.12. Atomic Force Microscopy and X-Ray characterisation of 80 nm thick film of C8-BTBT.

UV-Vis Absorption

Figure 6.13 presents the steady–state absorption spectrum of C8-BTBT in films. In a complete analogy with the maquettes, we identify the maximum absorption peak located at 360 nm (3.44 eV). We note a striking difference in absorption spectra resulting from different coating techniques for in the case of drop-casting the film produced more emissive peaks as well as more structured. Furthermore, the maxima peaks for the absorption of the samples do not completely overlap, with the drop-cast film been slightly blue-shifted. Films and the maquette spectra are significantly different, for on the one hand, we see a dim blue-shift of the main absorption peak for the drop-cast film, on the other hand, we see significant absorption in the monomer region which is not the case for the thin films. Which could mean that we have other absorbing species, this is interesting since it looks like we are in fact tuning the amount of aggregation among the molecules. What we see then, by comparing it to the isolated molecules in solution that the position of the peaks have changed

and some of them have been suppressed completely, in the bio–complex the spectrum looks cleaner with more defined features but a bit broader than the monomer case.

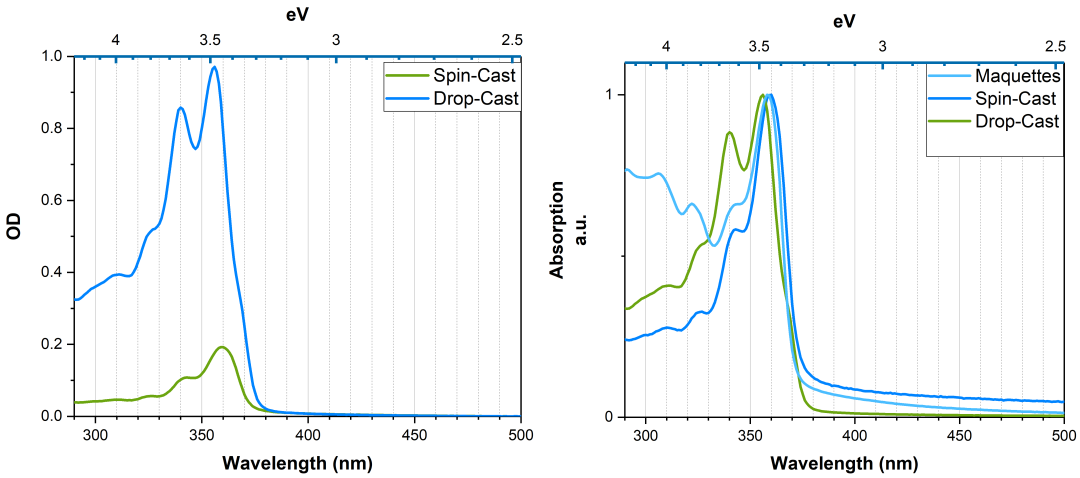

(a) Optical density of solution-process film.

(b) Absorption normalised to S_1 peak of absorption.

Figure 6.13. Absorption Spectra of C8-BTBT in Film produced by spin casting and drop casting and comparison with maquettes.

Photoluminescence

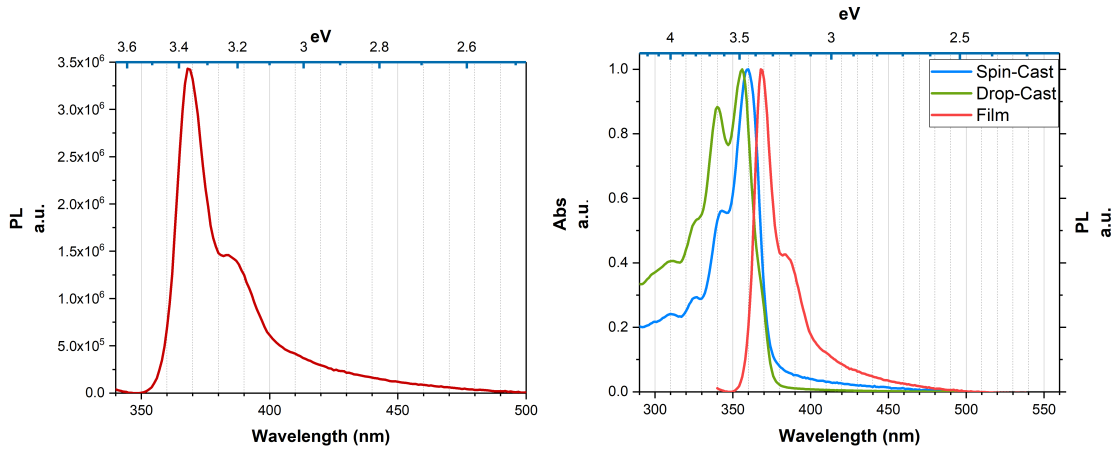

(a) Emission Spectrum of evaporated C8-BTBT thin film

(b) Absorption and Emission normalised to the S_1 peak.

Figure 6.14. Steady state spectra of C8-BTBT thin films.

Figure 6.14 (a) depicts the fluorescence emission spectra of C8-BTBT thin films. On this graph we see emission from one broad band, peaking at 370 nm (3.38 eV) and a shoulder located at 385 nm (3.22 eV). Panel (b) of the figure shows the normalised absorption and emission spectra showing a mirror image with vibronic structure.

Transient Absorption

To increase our understanding we carry TA spectroscopy at 360 nm excitation wavelength. Figure 6.15 shows the colour map of TA for different film samples. At first glance from panel (a)–(c) seems no obvious difference appear to emerge, the signal in the spin-cast film is significantly weaker than the other two and the signal arising from the drop cast film looks to live longer and to be narrower. Although, the spectral shape and peak positions do not change much.

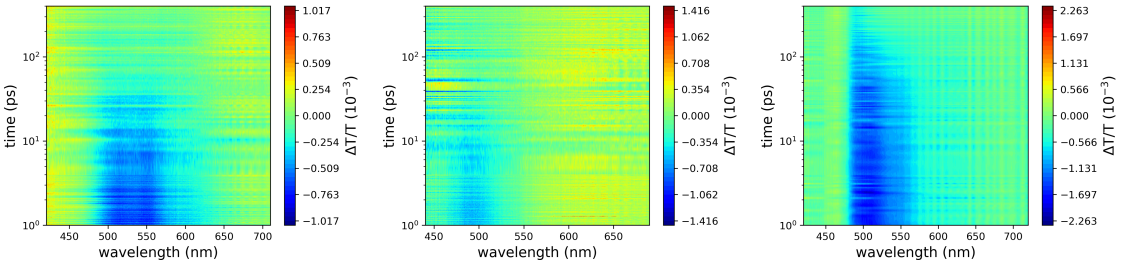

(a) Evaporated Film (b) Spin-cast Film (c) Drop-cast Film

Figure 6.15. Transient absorption spectra of C8-BTBT in various films excited at 360 nm.

Figure 6.16, revel more subtle differences among the samples. From left to right we observe a positive signal in the 450 nm region which could be due to stimulated emission, for from the PL we have non-negligible emission in such region. An excited state absorption with two peaks, one close to 500 nm and the other one at 550 nm. Panel (b) has the weakest signal, which explain the apparent positive signal in the redder part of the spectra, but nonetheless has the same PIA at 500 nm. Finally, on panel (c) we encounter a sharp signal at 500 nm, which anticipated from the 2-D map has longer lifetime. All samples had in common the signal at 500 nm, which from all the previous evidence points to be due to singlet excited state absorption. Additionaly, there seems no to be any indication of triplet formation nor triplet state absorption which mimic the results for the protein–complex. As we have mentioned previously, reproducibility in films is difficult to achieve thus the non-neglible differences in the TA data.

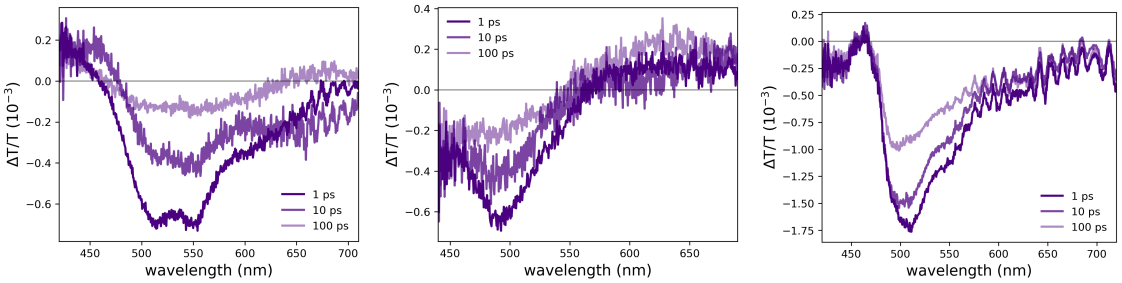

(a) Evaporated Film (b) Spin-cast Film (c) Drop-cast Film

Figure 6.16. Pump fluence and excitation wavelength dependence on transient absorption spectra of C8-BTBT with diverse film morphology, excited at λ_{exc_1} 330 nm and λ_{exc_2} 360 nm.

Finally, figure 6.17 shows what we have found for the solid state photophysics of C8-BTBT in contrast with the solution spectral features. In the figure we have

depicted the solution TA in dotted lines and the results from the films in solid lines. The steady-state spectroscopy of the film appears in blue (absorption) and in red (emission). What perhaps is most interesting emerges when we pay close attention to the right–hand side of the figure where we can see a faint overlapping of the single signature and the initial times for the films, and at the right-side note how well the stimulated emission matches the fluorescence spectra.

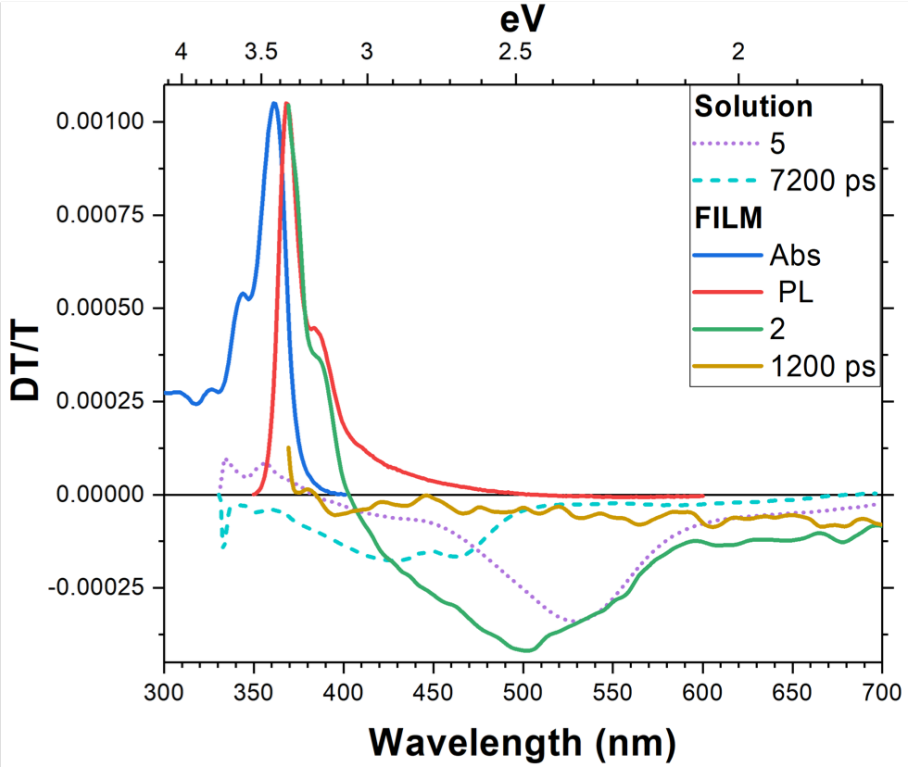

Figure 6.17. Comparison of absorption, photoluminescence, and transient absorption features among solution and films.

6.4 Conclusions

Our message to the patient reader should go along these lines:

> *'The experiments shown here, strongly point to **out-of-plane** vibrations as **the** central mechanism that enables intersystem crossing for the* C8-BTBT *(a fused-thienoacene) and by extension from this work of* BTBT-*systems too.'*
>
> (On ISC by JGV)

Both, the thin films and the maquette-chromophore complexes, revealed to have similarities and strong resemblances in the ground state absorption spectra. Nonetheless, experimental data showed that the two small absorbing peaks below 360 nm are present only in protein complexes, whereas in films these are absent. So, these non-vanishing absorbing species are believed to be evidence of monomeric-type of absorption. Furthermore, experimental spectroscopy data showed how complexes absorb and also emit at differently wavelengths to both solution and thin films as was shown by the photoluminescence data by the appearance of a broad band emission far beyond the one corresponding to the singlet state band cut-off, which strongly elicits the existence of excimers. As far as the *transient absorption* experimental data concerns, there is no substantial evidence for neither intersystem crossing nor for triplet-state formation taking place, whether we excited at 330 nm the monomeric-type of absorption region nor at 360 nm the thin film and the bio-complex absorption region. The TA spectra always appeared to be the have the same spectral feature, the one of a *singlet*. We believe, what is occurring in these complexes and solid-state thin films is that as soon as we tampered with the *out-of-plane* motion of the molecules by spatial confinement [5] in the maquettes or the solid-state, we disrupt the mechanism responsible for enabling the intersystem crossing. Hence, all spectroscopic features seem to originate from singlet excitons, however, there is a cautious observation that with this new '*hybrid*' singlet exciton which has a broader and longer-lived character, which in other materials is know to occur [143, 144], is suggested from our TA data, possibly being inherited by triplet-monomeric 'memory'.

[5] By virtually just 'clamping' them together

7 Summary and Outlook

Concluding Remarks.

Many applications of phosphorescence are inherently restricted to solid–state applications[1] so a full understanding on the photophysics of such devices is of paramount importance to the organic electronic industry but that cannot occur if first the basics of ISC in solutions is not unravelled, the results of these three investigations openly demonstrate how to achieve a great deal of understanding on metal-free planar organic molecules systems of this fundamental spin–process - the intersystem crossing mechanism.

In chapter 4, we laid out a model for the ISC mechanism in the BTBT molecule and its most commercially successful derivative the C8-BTBT. This work represents the first full photophysical characterisation of C8-BTBT in different molecular environments as far as our knowledge concerns, and we prove that the origin of ISC in solution is due the coupling of specific vibrational modes, namely *out–of–plane* vibrational modes, such modes are thought to be caused by the C–S bonding dynamics. We found that the role of alkyl-chain substitutions goes beyond a solubilising one, as was pointed out from the quantum mechanical calculations where we found that the oscillator strength parameter associated with the S_1 state grew in accordance with the addition of alkylated chains. Moreover, we found that side chains had also vibrational influence in the motion of the molecule since some of those vibrations effectively produce motion that is orthogonal to the molecular plane.

In chapter 5, we brought an array of different molecules all sharing the same BTBT core, two of them proved to be too complex to make further deductions, but the rest of them showed a non-trivial ISC trend where counter–intuitive results were found, we saw no increase in the ISC rate through halogenated substitution, on the contrary. All of these strongly pointing at the now evident spin-vibronic mechanism for ISC in these type of molecules. By adding these atoms quite likely we managed to tamper with the vibrations responsible of unravelling ISC.

Finally, in chapter 6 we made use of novel techniques developed in our institution that enabled us to embed C8-BTBT in maquette proteins, this allowed us to take insights on the aggregation effects in photophysical properties. We found,

[1] Trivial examples of phosphorescent materials are the glow-in-the-dark toys, ceiling-figures stickers, paints, wristwatch and clock dials that glow after being charged with a bright light

that ultimately ISC does not take place in the solid–state, this was puzzling for the energetics of the triplet states in solution and the singlet state in solid are close, so we would have expected an actual increase in the rate which was not the case. Instead, we saw a complete quench of it whilst at the same time an increase in the singlet lifetime, this *a-priori* it could be thought to be correlated but more study is needed. By having our molecules embedded in the maquettes we modified the optical response, unknowingly we suppressed in all likelihood the out–of–plane vibrations that are responsible for such fast ISC in solution. A similar argument can be applied to the films, yielding the same result – the lack of intersystem crossing in the solid state.

7.1 Outlook

We suggest the use of circular dichroism spectroscopical techniques by means to decipher the question of how many molecules go inside the maquette or if any of the chromophores is been attached to the exterior of the maquette. These issues will benefit enormously with the aid of quantum chemical calculations without a doubt *e.g.* their Raman modes, which could be compared with experimental values. Once a satisfactory method is established to determine aggregates structures, this work could be extended to a vast range of similar materials; both chromophores as well as maquettes proteins. This would provide an invaluable resource in the development of a robust structure-property *design-rules* for intersystem crossing tuning.

Bibliography

1. Dou *et al.* 25th Anniversary Article: A Decade of Organic/Polymeric Photovoltaic Research. *Advanced Materials* **25,** 6642–6671. https://doi.org/10.1002/adma.201302563 (2013).
2. Li, G., Zhu, R. & Yang, Y. Polymer solar cells. *Nature Photonics* **6** (2012).
3. Virkar, A. A., Mannsfeld, S., Bao, Z. & Stingelin, N. Organic Semiconductor Growth and Morphology Considerations for Organic Thin-Film Transistors. *Advanced Materials* **22,** 3857–3875. ISSN: 1521-4095. https://doi.org/10.1002/adma.200903193 (2010).
4. Ebata, H. *et al.* Highly soluble [1]benzothieno[3,2-b]benzothiophene (BTBT) derivatives for high-performance, solution-processed organic field-effect transistors. *Journal of the American Chemical Society* **129,** 15732–3. ISSN: 0002-7863. https://doi.org/10.1021/ja074841i (2007).
5. Yuan, Y. *et al.* Ultra-high mobility transparent organic thin film transistors grown by an off-centre spin-coating method. *Nature Communications* **5,** 3005. ISSN: 2041-1723. https://doi.org/10.1038/ncomms4005 (2014).
6. Liang, J., Schiff, E., Guha, S, Yan, B. & Yang, J. Hole-mobility limit of amorphous silicon solar cells. *Applied Physics Letters* **88,** 063512. https://doi.org/10.1063/1.2170405 (2006).
7. Bengtson, S., Sallstedt, T., Belivanova, V. & Whitehouse, M. Three-dimensional preservation of cellular and subcellular structures suggests 1.6 billion-year-old crown-group red algae. *PLOS Biology* **15,** e2000735. ISSN: 1545-7885. https://doi.org/10.1371/journal.pbio.2000735 (2017).
8. Delor, M. *et al.* Toward control of electron transfer in donor-acceptor molecules by bond-specific infrared excitation. *Science* **346,** 1492–1495. ISSN: 0036-8075. https://doi.org/10.1126/science.1259995 (2014).

9. Mishra, A. & Bäuerle, P. Small Molecule Organic Semiconductors on the Move: Promises for Future Solar Energy Technology. *Angewandte Chemie International Edition* **51,** 2020–2067. ISSN: 1521-3773. https://doi.org/10.1002/anie.201102326 (2012).

10. Sun, S. S. & Sariciftci, N. S. *Organic photovoltaics: mechanisms, materials, and devices* (Taylor & Francis Group, 2005).

11. Perlin, J. *From Space to Earth: The Story of Solar Electricity* (Harvard University Press, 2002).

12. Rasmussen, S. C. The Early History of Polyaniline: Discovery and Origins. *Substantia* **1.** ISSN: 2532-3997. https://doi.org/10.13128/Substantia-30 (2017).

13. Shirakawa, H., Louis, E. J., MacDiarmid, A. G., Chiang, C. K. & Heeger, A. J. Synthesis of electrically conducting organic polymers: halogen derivatives of polyacetylene, (CH) x. *Journal of the Chemical Society, Chemical Communications,* 578. ISSN: 0022-4936. https://doi.org/10.1039/C39770000578 (1977).

14. Shirakawa, H., McDiarmid, A. & Heeger, A. Twenty-five years of conducting polymers. *Chemical Communications* **0,** 1–4. ISSN: 1359-7345. https://doi.org/10.1039/B210718J (2003).

15. Mann, B. & Kuhn, H. Tunneling through Fatty Acid Salt Monolayers. *Journal of Applied Physics* **42,** 4398–4405. ISSN: 0021-8979. https://doi.org/10.1063/1.1659785 (1971).

16. Aviram, A. & Ratner, M. A. Molecular rectifiers. *Chemical Physics Letters* **29,** 277–283. ISSN: 0009-2614. https://doi.org/10.1016/0009-2614(74)85031-1 (1974).

17. Chung, T.-C., Kaufman, J. H., Heeger, A. J. & Wudl, F. Charge storage in doped poly(thiophene): Optical and electrochemical studies. *Physical Review B* **30,** 702–710. ISSN: 1098-0121. https://doi.org/10.1103/physrevb.30.702 (1983).

18. Wudl, F., Wobschall, D. & Hufnagel, E. J. Electrical conductivity by the bis(1,3-dithiole)-bis(1,3-dithiolium) system. *Journal of the American Chemical Society* **94,** 670–672. ISSN: 0002-7863. https://doi.org/10.1021/ja00757a079 (1972).

19. Wudl, F., Kobayashi, M & Heeger, A. Poly(isothianaphthene). *The Journal of Organic Chemistry* **49,** 3382–3384. ISSN: 0022-3263. https://doi.org/10.1021/jo00192a027 (1984).

20. Roncali, J. Conjugated poly(thiophenes): synthesis, functionalization, and applications. *Chemical Reviews* **92,** 711–738. ISSN: 0009-2665. https://doi.org/10.1021/cr00012a009 (1992).

21. Perepichka, I. F. & Perepichka, D. F. *Handbook of Thiophene-based Materials* 887. ISBN: 978-0-470-05732-2 (2009).

22. Burroughes, J. *et al.* Light-emitting diodes based on conjugated polymers. *Nature* **347,** 347539a0. ISSN: 1476-4687. https://doi.org/10.1038/347539a0 (1990).

23. Pope, M, Kallmann, H. & Magnante, P. Electroluminescence in Organic Crystals. *The Journal of Chemical Physics* **38,** 2042–2043. ISSN: 0021-9606. https://doi.org/10.1063/1.1733929 (1963).

24. Kallmann, H & Pope, M. Positive hole injection into organic crystals. *The Journal of Chemical Physics* **32,** 300–301. https://doi.org/10.1063/1.1700925 (1960).

25. Groenendaal, L, Jonas, F, Freitag, D, Pielartzik, H & Reynolds, J. Poly(3,4-ethylenedioxythiophene) and Its Derivatives: Past, Present, and Future. *Advanced Materials* **12,** 481–494. ISSN: 1521-4095. https://doi.org/10.1002/(SICI)1521-4095(200004)12:7<481::AID-ADMA481>3.0.CO;2-C (2000).

26. Geoghegan, M. & Hadziioannou, G. *Polymer Electronics* 256. ISBN: 978-0-49-953382-4 (2013).

27. Krüger, J. *et al.* Decacene: On-Surface Generation. *Angewandte Chemie International Edition* **56,** 11945–11948. ISSN: 1521-3773. https://doi.org/10.1002/anie.201706156 (2017).

28. Sirringhaus, H. Device Physics of Solution-Processed Organic Field-Effect Transistors. *Advanced Materials* **17,** 2411–2425. ISSN: 1521-4095. https://doi.org/10.1002/adma.200501152 (2005).

29. Sirringhaus, H. 25th Anniversary Article: Organic Field-Effect Transistors: The Path Beyond Amorphous Silicon. *Advanced Materials* **26,** 1319–1335. ISSN: 1521-4095. https://doi.org/10.1002/adma.201304346 (2014).

30. McCulloch, I. Organic Electronics — From Materials to Applications. *Advanced Materials* **22,** 3760–3761. ISSN: 1521-4095. https://doi.org/10.1002/adma.201002794 (2010).

31. Orgiu, E. & Samorì, P. 25th Anniversary Article: Organic Electronics Marries Photochromism: Generation of Multifunctional Interfaces, Materials, and Devices. *Advanced Materials* **26,** 1827–1845. ISSN: 1521-4095. https://doi.org/10.1002/adma.201304695 (2014).

32. Tang, C. W. Two-layer organic photovoltaic cell. *Applied Physics Letters* **48,** 183–185. ISSN: 0003-6951. https://doi.org/10.1063/1.96937 (1986).

33. Hummelen, J. C. *et al.* Preparation and Characterization of Fulleroid and Methanofullerene Derivatives. *The Journal of Organic Chemistry* **60,** 532–538. ISSN: 0022-3263. https://doi.org/10.1021/jo00108a012 (1995).

34. Köhler, A. & Bässler, H. *Electronic Processes in Organic Semiconductors.* (Wiley-VCH, 2015).

35. Capelle, K. A bird's-eye view of density-functional theory. https://arxiv.org/abs/cond-mat/0211443 (2002).

36. Marian, C. M. Spin–orbit coupling and intersystem crossing in molecules. *Wiley Interdiscip Rev Comput Mol Sci* **2,** 187–203. ISSN: 1759-0884. https://doi.org/10.1002/wcms.83 (2012).

37. Hanna, M. W. *Quantum mechanics in chemistry.* (W. A. Benjamin, 1969).

38. Atkins, P. & Friedman, R. *Molecular Quantum Mechanics* (Oxford University Press, 2005).

39. Demtröder, W. *Atoms, Molecules and Photons, An Introduction to Atomic-, Molecular- and Quantum Physics* https://doi.org/10.1007/978-3-642-10298-1 (springer, 2010).

40. Born, M & Oppenheimer, R. Zur Quantentheorie der Molekeln. *Annalen der Physik* **389,** 457–484. ISSN: 0003-3804. https://doi.org/10.1002/andp.19273892002 (1927).

41. Kölle, P., Schnappinger, T. & de Vivie-Riedle, Regina. Deactivation pathways of thiophene and oligothiophenes: internal conversion versus intersystem crossing. *Phys Chem Chem Phys* **18,** 7903–7915. ISSN: 1463-9076. https://doi.org/10.1039/c5cp07634j (2016).

42. Frenkel, J. On the Transformation of light into Heat in Solids. I. *Phys. Rev.* **37,** 17–44. https://link.aps.org/doi/10.1103/PhysRev.37.17 (1 1931).

43. Scholes, G. D. & Rumbles, G. Excitons in nanoscale systems. *Nature Materials* **5,** nmat1710. ISSN: 1476-4660. https://doi.org/10.1038/nmat1710 (2006).

44. Parson, W. W. *Modern Optical Spectroscopy* Student edition. ISBN: 978-3-540-95895-6. https://doi.org/10.1007/978-3-540-37542-5 (Springer-Verlag, 2009).

45. Turro *et al. Modern Molecular Photochemistry of Organic Molecules.* ISBN: 978-1-891389-25-2 (University Science Books, 2010).

46. Juan, C., Grancini, G. & Lanzani, G. Pump-Probe Spectroscopy in Organic Semiconductors: Monitoring Fundamental Processes of Relevance in Optoelectronics. *Adv Mater* **23,** 5468–5485. ISSN: 1521-4095. https://doi.org/10.1002/adma.201102015 (2011).

47. Jahng, J. *et al.* Ultrafast pump-probe force microscopy with nanoscale resolution. *Appl Phys Lett* **106,** 083113. ISSN: 0003-6951. https://doi.org/10.1063/1.4913853 (2015).

48. Fischer, M. C., Wilson, J. W., Robles, F. E. & Warren, S. Invited Review Article: Pump-probe microscopy. *Review of Scientific Instruments* **87,** 031101. ISSN: 0034-6748. https://doi.org/10.1063/1.4943211 (2016).

49. Berera, R., van Grondelle, Kennis, R. & TM, J. Ultrafast transient absorption spectroscopy: principles and application to photosynthetic systems. *Photosynth Res* **101,** 105–118. ISSN: 0166-8595. https://doi.org/10.1007/s11120-009-9454-y (2009).

50. Di, D. *et al.* High-performance light-emitting diodes based on carbene-metal-amides. *Science* **163,** 159–163. https://doi.org/10.1126/science.aah4345.

51. Einzinger *et al.* Sensitization of silicon by singlet exciton fission in tetracene. *Nature* **571,** 90–94. ISSN: 0028-0836. https://doi.org/10.1038/s41586-019-1339-4 (2019).

52. Stranius, K., Hertzog, M. & Börjesson, K. Selective manipulation of electronically excited states through strong light-matter interactions. *Nature Communications* **9,** 2273. ISSN: 2041-1723. http://dx.doi.org/10.1038/s41467-018-04736-1 (2018).

53. Pinnola, A. & Bassi, R. Molecular mechanisms involved in plant photoprotection. *Biochemical Society Transactions* **46,** 467–482 (2018).

54. Cakmak, Y. *et al.* Designing Excited States : Theory-Guided Access to Efficient Photosensitizers for Photodynamic Action **. *Angewandte Chemie - International Edition* **50,** 11937–11941 (2011).

55. Wang, H. *et al.* Insights into the excitonic processes in polymeric photocatalysts. *Chemical Science* **8,** 4087–4092 (2017).

56. Boehme, C. & Lupton, J. M. Challenges for organic spintronics. *Nature Publishing Group* **8,** 612–615. ISSN: 1748-3387. http://dx.doi.org/10.1038/nnano.2013.177 (2013).

57. Sun, D., Ehrenfreund, E. & Valy Vardeny, Z. The first decade of organic spintronics research. *Chem. Commun.* **50,** 1781–1793. ISSN: 1359-7345. http://xlink.rsc.org/?DOI=C3CC47126H (2014).

58. Köhler, A. & Bässler, H. Triplet states in organic semiconductors. *Materials Science and Engineering R: Reports* **66,** 71–109. ISSN: 0927796X (2009).

59. Schott, S. *et al.* Tuning the effective spin-orbit coupling in molecular semiconductors. *Nature Communications* **8,** 15200. http://dx.doi.org/10.1038/ncomms15200 (2017).

60. Nuccio, L. *et al.* Importance of spin-orbit interaction for the electron spin relaxation in organic semiconductors. *Physical Review Letters* **110,** 1–5. ISSN: 00319007 (2013).

61. Sun, D. *et al.* Inverse spin Hall effect from pulsed spin current in organic semiconductors with tunable spin-orbit coupling. *Nature Materials* **15,** 863–870 (2016).

62. Joshi, G. *et al.* Isotropic E ff ective Spin-Orbit Coupling in a Conjugated Polymer. *Journal of the American Chemical Society* **140,** 6758–6762. ISSN: 0002-7863 (2018).

63. Penfold, T. J., Gindensperger, E., Daniel, C. & Marian, C. M. Spin-Vibronic Mechanism for Intersystem Crossing. *Chemical Reviews,* acs.chemrev.7b00617. ISSN: 0009-2665. http://pubs.acs.org/doi/10.1021/acs.chemrev.7b00617 (2018).

64. Marian, C. M. Spin-orbit coupling and intersystem crossing in molecules. *Wiley Interdisciplinary Reviews: Computational Molecular Science* **2,** 187–203. ISSN: 17590876 (2012).

65. Ratzke, W. *et al.* Effect of Conjugation Pathway in Metal-Free Room-Temperature Dual Singlet - Triplet Emitters for Organic Light-Emitting Diodes. *The Journal of Physical Chemistry Letters* **7,** 4802–4808 (2016).

66. Schooten, K. J. V., Baird, D. L., Limes, M. E., Lupton, J. M. & Boehme, C. of electrically detected spin beating. *Nature Communications* **6,** 6688 (2015).

67. Malissa, H *et al.* Revealing weak spin-orbit coupling effects on charge carriers in a π -conjugated polymer. *Physical Review B* **97,** 161201 (2018).

68. Penfold, T. J. & Worth, G. A. The effect of molecular distortions on spin – orbit coupling in simple hydrocarbons. *Chemical Physics* **375,** 58–66. ISSN: 0301-0104. http://dx.doi.org/10.1016/j.chemphys.2010.07.019 (2010).

69. Shoji, Y. *et al.* Unveiling a New Aspect of Simple Arylboronic Esters: Long-Lived Room-Temperature Phosphorescence from Heavy-Atom-Free Molecules. *J. Am. Chem. Soc.* **139,** 2728–2733 (2017).

70. Bowman, M. K. Intersystem Crossing in Photosynthetic Pigments. *Chemical Physics Letters* **48,** 17–21 (1977).

71. Pederzoli, M. & Pittner, J. A new approach to molecular dynamics with non-adiabatic and spin-orbit effects with applications to QM/MM simulations of thiophene and selenophene. *Journal of Chemical Physics* **146.** ISSN: 00219606 (2017).

72. Skov, A. B., Larsen, M. A. B., Liisberg, M. B., Hansen, T. & Sølling, T. I. Conformationally controlled ultrafast intersystem crossing in bithiophene systems. *Phys. Chem. Chem. Phys. Phys. Chem. Chem. Phys* **20,** 13412–13418. ISSN: 1463-9084. http://pubs.rsc.org/en/content/articlepdf/2018/cp/c8cp01419a (1341).

73. Zobel, J. P., Nogueira, J. J. & Gonz, L. Mechanism of Ultrafast Intersystem Crossing in. *Chemistry - A European Journal* **24,** 5379–5387 (2018).

74. Philip, A. M., Gudem, M., Sebastian, E. & Hariharan, M. Decoding the Curious Tale of Atypical Intersystem Crossing Dynamics in Regioisomeric Acetylanthracenes Published as part of The Journal of Physical Chemistry virtual special issue " Young Scientists " . *The Journal of Physical Chemistry A* **123,** 6105–6112. ISSN: 1089-5639 (2019).

75. Mai, S., Marquetand, P. & González, L. Non-adiabatic and intersystem crossing dynamics in SO2. II. The role of triplet states in the bound state dynamics studied by surface-hopping simulations. *The Journal of Chemical Physics* **140,** 204302. eprint: https://

doi.org/10.1063/1.4875036. https://doi.org/10.1063/1.4875036 (2014).

76. Prlj, A. & Curchod, B. F. E. Excited state dynamics of thiophene and bithiophene : new insights into theoretically challenging systems †. *Phys. Chem. Chem. Phys.* **17,** 14719–14730 (2015).

77. Schnappinger, T. *et al.* Ab initio molecular dynamics of thiophene: The interplay of internal conversion and intersystem crossing. *Physical Chemistry Chemical Physics* **19,** 25662–25670. ISSN: 14639076 (2017).

78. Schnappinger, T. *et al.* Intersystem Crossing as a Key Component of the Nonadiabatic Relaxation Dynamics of Bithiophene and Terthiophene. **14,** 4530–4540 (2018).

79. Datko, B. D. *et al.* Large Excited-State Conformational Displacements Expedite Triplet Formation in a Small Conjugated Oligomer. *The Journal of Physical Chemistry Letters* **10,** 1259–1263 (2019).

80. Beljonne, D. *et al.* Optical signature of delocalized polarons in conjugated polymers. *Advanced Functional Materials* **11,** 229–234. ISSN: 1616301X (2001).

81. Paa, W., Yang, J.-p., Helbig, M., Hein, J. & Rentsch, S. Femtosecond time-resolved measurements of terthiophene : fast singlet – triplet intersystem crossing. *Chemical Physics Letters* **292,** 607–614 (1998).

82. Tatchen, J., Gilka, N. & Marian, C. M. Intersystem crossing driven by vibronic spin – orbit coupling : a case study on psoralen w. *Phys. Chem. Chem. Phys.* **9,** 5209–5221 (2007).

83. Yang, W. *et al.* Efficient Intersystem Crossing in Heavy-Atom-Free Perylenebisimide Derivatives. *The Journal of Physical Chemistry C* **120,** 10162–10175 (2016).

84. Northey, T & Penfold, T. J. The intersystem crossing mechanism of an ultrapure blue organoboron emitter. *Organic Electronics* **59,** 45–48. ISSN: 1566-1199. https://doi.org/10.1016/j.orgel.2018.04.038 (2018).

85. Ji, S. *et al.* Molecular Structure - Intersystem Crossing Relationship of Heavy- Atom-Free BODIPY Triplet Photosensitizers. *The Journal of Organic Chemistry* **80,** 5958–5963 (2015).

86. Mcnellis, E. R., Schott, S., Sirringhaus, H. & Sinova, J. Molecular tuning of the magnetic response in organic semiconductors. *Physical Review Materials* **2,** 074405 (2018).

87. Dediu, V, Murgia, M, Matacotta, F. C., Taliani, C & Barbanera, S. Room temperature spin polarized injection in organic semiconductor. *Solid State Communications* **122,** 181–184 (2002).

88. Yong, C. K. *et al.* The entangled triplet pair state in acene and heteroacene materials. *Nature Communications* **8,** 15953. ISSN: 2041-1723. http://www.nature.com/doifinder/10.1038/ncomms15953 (2017).

89. Dean, J. C. *et al.* Photophysical characterization and time-resolved spectroscopy of a anthradithiophene dimer: exploring the role of conformation in singlet fission. *Phys. Chem. Chem. Phys.* **19,** 23162–23175. ISSN: 1463-9076. http://xlink.rsc.org/?DOI=C7CP03774K (2017).

90. Chen, Y., Shen, L. & Li, X. Effects of Heteroatoms of Tetracene and Pentacene Derivatives on Their Stability and Singlet Fission. *The Journal of Physical Chemistry A* **118,** 5700–5708 (2014).

91. Wex, B., Kaafarani, B. R., Danilov, E. O. & Neckers, D. C. Altering the emission behavior with the turn of a thiophene ring: The photophysics of condensed ring systems of alternating benzenes and thiophenes. *Journal of Physical Chemistry A* **110,** 13754–13758. ISSN: 10895639 (2006).

92. Melo, J. S. D., Pina, J, Rodrigues, L. M. & Becker, R. S. A comprehensive study of the spectral and photophysical properties of arylthiophenes. *J. Photochemistry and Photobiology A: Chemistry* **194,** 67–75 (2008).

93. Minemawari, H. *et al.* Inkjet printing of single-crystal films. *Nature* **475,** 364. ISSN: 1476-4687. https://doi.org/10.1038/nature10313 (2011).

94. Illig, S. *et al.* Reducing dynamic disorder in small-molecule organic semiconductors by suppressing large-amplitude thermal motions. *Nature Communications* **7,** 10736. ISSN: 2041-1723. http://www.nature.com/doifinder/10.1038/ncomms10736 (2016).

95. Schweicher, G. *et al.* Bulky End-Capped [1] Benzothieno [3 , 2- b] benzothiophenes : Reaching High-Mobility Organic Semiconductors by Fine Tuning of the Crystalline Solid-State Order. *Advanced Materials,* 3066–3072 (2015).

96. Chopra, U., Egorov, S. A., Sinova, J. & Mcnellis, E. R. Chemical and Structural Trends in the Spin-Admixture Parameter of Organic Semiconductor Molecules. *The Journal of Physical Chemistry C* **123,** 19112–19118. ISSN: 1932-7447 (2019).

97. Myers, A. B. Resonance Raman Intensities and Charge-Transfer Reorganization Energies. *Chemical reviews* **96,** 911–926. ISSN: 1520-6890. http://www.ncbi.nlm.nih.gov/pubmed/11848775 (1996).

98. Zhou, Y., Deng, W.-Q. & Zhang, H.-L. Phonon-electron coupling and tunneling effect on charge transport in organic semi- conductor crystals of C n -BTBT. *J. Chem. Phys.* **145,** 104108 (2016).

99. Wortmann, R., Elich, K., Lebus, S. & Liptay, W. Experimental determination of the S 1 torsional potential of 9 , 9 ' -bianthryl in 2-methyl-butane by simultaneous Franck – Condon and band shape analysis of temperature dependent optical fluorescence spectra. *J. Chem. Phys* **95,** 6371 (1991).

100. Jortner, J. & Jortner, J. Temperature dependent activation energy for electron transfer between biological molecules transfer between biological molecules. *J. Chem. Phys.* **64,** 4860 (1976).

101. Pavlopoulos, T. G. Vibronic Spin – Orbit Interaction in the Phosphorescence Spectrum of Phenazine. *The Journal of Chemical Physics* **2936** (1969).

102. Osaki, T. & Soejima, E. Quadratic scaling functions for obtaining Normal vibrational wavenumbers from the B3LYP calculation. *Res. Bull. Fukuoka Inst. Tech* **42,** 129–134 (2010).

103. Sotgiu, G, Zambianchi, M, Barbarella, G & Botta, C. Synthesis and optical properties of soluble sexithiophenes with one central head-to-head junction. *Tetrahedron* **58,** 2245–2251 (2002).

104. Dobrin, S., Kaszynski, P., Ikeda, S. & Waluk, J. Photophysics of trans-stilbene analogues: Indolo[3,2-b]indole and its heterosubstituted sulfur and selenium derivatives. *Chemical Physics* **216,** 179–192. ISSN: 03010104 (1997).

105. Schmidt, K. *et al.* Intersystem crossing processes in nonplanar aromatic heterocyclic molecules. *Journal of Physical Chemistry A* **111,** 10490–10499. ISSN: 10895639 (2007).

106. Fornari, R. P., Aragó, J. & Troisi, A. A very general rate expression for charge hopping in semiconducting polymers. *The Journal of Chemical Physics* **142,** 184105. http://dx.doi.org/10.1063/1.4920945 (2017).

107. Zuehlsdorff, T. J. & Isborn, C. M. Combining the ensemble and Franck- Condon approaches for calculating spectral shapes of molecules in solution. *The Journal of Chemical Physics* **148,** 024110. http://dx.doi.org/10.1063/1.5006043 (2018).

108. Ruzié, C. *et al.* Design, synthesis, chemical stability, packing, cyclic voltammetry, ionisation potential, and charge transport of [1]benzothieno[3,2- b][1]benzothiophene derivatives. *Journal of Materials Chemistry C* **4,** 4863–4879. ISSN: 2050-7526. https://doi.org/10.1039/C6TC01409G (2016).

109. Fernández, A. *et al.* [1]Benzothieno[3,2-b]benzothiophene (BTBT) derivatives: Influence in the molecular orientation and charge delocalization dynamics. *Materials Chemistry and Physics* **221,** 295–300. ISSN: 0254-0584. https://doi.org/10.1016/j.matchemphys.2018.09.064 (2019).

110. Fan, J.-X. *et al.* Theoretical study of synergetic effect between halogenation and pyrazine substitutions on transport properties of silylethynylated pentacene. *New Journal of Chemistry* **43,** 3583–3600. ISSN: 1144-0546. https://doi.org/10.1039/C8NJ04714F (2019).

111. Kula, S *et al.* Synthesis and photophysical properties of novel multisubstituted benzene and naphthalene derivatives with high 2D-π-conjugation. *Optical Materials* **47,** 118–128. ISSN: 0925-3467. https://doi.org/10.1016/j.optmat.2015.07.011 (2015).

112. Takimiya, K., Osaka, I., Mori, T. & Nakano, M. Organic Semiconductors Based on [1]Benzothieno[3,2- b][1]benzothiophene Substructure. *Accounts of Chemical Research* **47,** 1493–1502. ISSN: 0001-4842. https://doi.org/10.1021/ar400282g (2014).

113. Takimiya, K., Yamamoto, T., Ebata, H. & Izawa, T. [1]Benzothieno[3,2-b][1]benzothiophenes- and dinaphtho[2,3-b:2',3'-f]thieno[3,2-b]thiophene-based organic semiconductors for stable, high-performance organic thin-film transistor materials. *Thin Solid Films* **554,** 13–18. ISSN: 0040-6090. https://doi.org/10.1016/j.tsf.2013.08.026 (2014).

114. Cardia, R, Malloci, G, Bosin, A, Serra, G & Cappellini, G. Computational investigation of the effects of perfluorination on the charge-transport properties of polyaromatic hydrocarbons. *Chemical Physics* **478,** 8–13. ISSN: 0301-0104 (2016).

115. Liu, K. *et al.* Tuning the ambipolar charge transport properties of N-heteropentacenes by their frontier molecular orbital energy levels. *Journal of Materials Chemistry C* **3,** 4188–4196. ISSN: 2050-7526. https://doi.org/10.1039/C4TC02859G (2015).

116. Babudri, F., Farinola, G. M., Naso, F. & Ragni, R. Fluorinated organic materials for electronic and optoelectronic applications: the role of the fluorine atom. *Chemical Communications* **0,** 1003–1022. ISSN: 1359-7345. https://doi.org/10.1039/B611336B (2006).

117. Milián-Medina, B. *et al.* Excited-state switching by per-fluorination of para -oligophenylenes. *The Journal of Chemical Physics* **135,** 124509. ISSN: 0021-9606. https://doi.org/10.1063/1.3643151 (2011).

118. Liu, J. *et al.* Enhancing field-effect mobility and maintaining solid-state emission by incorporating 2,6-diphenyl substitution to 9,10-bis(phenylethynyl)anthracene. *Journal of Materials Chemistry C* **5,** 2519–2523. ISSN: 2050-7526. https://doi.org/10.1039/C7TC00372B (2017).

119. Takimiya, K. *et al.* 2,7-Diphenyl[1]benzoselenopheno[3,2-b][1]benzoselenophene as a Stable Organic Semiconductor for a High-Performance Field-Effect Transistor. *Journal of the American Chemical Society* **128,** 3044–3050. ISSN: 0002-7863. https://doi.org/10.1021/ja057641k (2006).

120. Takimiya, K., Shinamura, S., Osaka, I. & Miyazaki, E. Thienoacene-Based Organic Semiconductors. *Advanced Materials* **23,** 4347–4370. ISSN: 1521-4095. https://doi.org/10.1002/adma.201102007 (2011).

121. Mori, T. *et al.* Consecutive Thiophene-Annulation Approach to π-Extended Thienoacene-Based Organic Semiconductors with [1]Benzothieno[3,2-b][1]benzothiophene (BTBT) Substructure. *Journal of the American Chemical Society* **135,** 13900–13913. ISSN: 0002-7863. https://doi.org/10.1021/ja406257u (2013).

122. Niebel, C. *et al.* Thienoacene dimers based on the thieno[3,2- b]thiophene moiety: synthesis, characterization and electronic properties. *Journal of Materials Chemistry C* **3,** 674–685. ISSN: 2050-7526. https://doi.org/10.1039/C4TC02158D (2014).

123. Davies, J. A. *Synthetic Biology: A Very Short Introduction* https://doi.org/10.1093/actrade/9780198803492.001.0001 (Oxford University Press, 2018).

124. Hemmig, E. A. *et al.* Programming Light-Harvesting Efficiency Using DNA Origami. *Nano Letters* **16,** 2369–74. ISSN: 1530-6984. https://doi.org/10.1021/acs.nanolett.5b05139 (2016).

125. Snow, A. A. & Smith, V. H. Genetically Engineered Algae for Biofuels: A Key Role for Ecologists. *BioScience* **62,** 765–768. https://doi.org/10.1525/bio.2012.62.8.9 (Aug. 2012).

126. Koder, R. L. *et al.* Design and engineering of an O2 transport protein. *Nature* **458,** 305–309. ISSN: 0028-0836. http://www.nature.com/doifinder/10.1038/nature07841 (2009).

127. Kodali, G. *et al.* Design and engineering of water-soluble light-harvesting protein maquettes. *Chem Sci* **8,** 316–324. ISSN: 2041-6520. https://doi.org/10.1039/C6SC02417C (2016).

128. Lishchuk, A, Kodali, G, Mancini, J. & Nanoscale, B. M. A synthetic biological quantum optical system. ISSN: 2040-3364. https://doi.org/10.1039/C8NR02144A (2018).

129. Noy D. *et al*, t. D. d. b. u. h. p. n. v. j. B. y.

130. Josefsen, L. B. & Boyle, R. W. Photodynamic Therapy and the Development of Metal-Based Photosensitisers. *Metal-Based Drugs* **2008.** ISSN: 0793-0291. https://doi.org/10.1155/2008/276109 (2008).

131. Anderson, R. e. Constructing a man-made c-type cytochrome maquette in vivo : electron transfer, oxygen transport and conversion to a photoactive light harvesting maquette. *Chemical Science* **5,** 507–514. https://doi.org/10.1039/C3SC52019F (2013).

132. Shukla, M. K. e. Binding of pigments to the cyanobacterial high-light-inducible protein HliC. *Photosynthesis Research* **95,** 29–39. https://doi.org/10.1007/s11120-017-0475-7 (2018).

133. Dawson, W. e. Towards functional de novo designed proteins. *Current Opinion in Chemical Biology* **52,** 102–111. https://doi.org/10.1016/j.cbpa.2019.06.011 (2019).

134. Lichtenstein, B. R. *et al.* Designing Light-Activated Charge-Separating Proteins with a Naphthoquinone Amino Acid. *Angewandte Chemie International Edition* **54,** 13626–13629. ISSN: 1521-3773. https://doi.org/10.1002/anie.201507094 (2015).

135. Mancini, J. A. *et al.* De novo synthetic biliprotein design, assembly and excitation energy transfer. *Journal of the Royal Society Interface* **15,** 20180021. ISSN: 1742-5689. https://doi.org/10.1098/rsif.2018.0021 (2018).

136. Berg, J. M., Tymoczko, J. L. & Stryer, L. *Biochemistry.* ISBN: 0716746840. https://www.ncbi.nlm.nih.gov/books/NBK21154/ (W.H. Freeman, 2002).

137. Phillips, R. *et al. Physical Biology of the Cell.* ISBN: 9780815344506. https://www.crcpress.com/Physical-Biology-of-the-Cell/Phillips-Kondev-Theriot-Garcia/p/book/9780815344506 (CRC Press, 2012).

138. Marcus, R. & Sutin, N. Electron transfers in chemistry and biology. *Biochimica Et Biophysica Acta Bba - Rev Bioenergetics* **811,** 265–322. ISSN: 0304-4173. https://doi.org/10.1016/0304-4173(85)90014-X (1985).

139. Polak, D. *et al.* Band-edge Excitation of Carotenoids Removes S* Revealing Triplet-pair Contributions to the S1 Absorption Spectrum. *arXiv e-prints.* https://export.arxiv.org/abs/1901.04900v1 (Jan. 2019).

140. Sutherland, G. A. *De novo designed proteins for applications in research and biotechnology.* (2018).

141. Yu, K., Polavarapu, L. & Xu, Q.-H. Excitation Wavelength and Fluence Dependent Femtosecond Transient Absorption Studies on Electron Dynamics of Gold Nanorods. *The Journal of Physical Chemistry A* **115,** 3820–3826. https://doi.org/10.1021/jp108176h (2011).

142. Lu Lyu Dongmei Niu, H. X. N. C. H. Z. Y. Z. P. L. Y. G. Orientation-dependent energy level alignment and film growth of 2,7-diocty[1]benzothieno[3,2-b]benzothiophene (C8-BTBT) on HOPG. *The Journal of Chemical Physics* **144,** 034701. ISSN: 0021-9606. https://doi.org/10.1063/1.4939839 (2016).

143. Polak, D. *et al.* Manipulating molecules with strong coupling: harvesting triplet excitons in organic exciton microcavities. *Chemical Science* **11.** ISSN: 2041-6520. https://10.1039/c9sc04950a (2019).

144. Eizner, E., Martínez-Martínez, L. A., Yuen-Zhou, J. & Kéna-Cohen, S. Inverting singlet and triplet excited states using strong light-matter coupling. *Science Advances* **5.** ISSN: 2375-2548. https://10.1126/sciadv.aax4482 (2019).